Measurement of $^{3}\mathrm{He}(\alpha,\gamma)^{7}\mathrm{Be}$ cross section with the recoil mass separator ERNA

Dissertation
zur Erlangung des Grades eines
Doktors der Naturwissenschaften
in der
Fakultät für Physik und Astronomie
der Ruhr-Universität Bochum

vorgelegt von
Antonino Di Leva
aus Caserta

Bochum 2009

Gutachter:

Prof. C.E. Rolfs

PD F. Strieder

Tag der mündlichen Prüfung: 10.07.2009

Contents

Contents **i**

Introduction **1**

1 The ^{3}He$(\alpha,\gamma)^7$Be reaction **3**
1.1 ^{3}He$(\alpha,\gamma)^7$Be in astrophysics 3
1.1.1 Big Bang Nucleosynthesis 3
1.1.2 Solar neutrinos 7
1.2 The ^{3}He$(\alpha,\gamma)^7$Be reaction in laboratory 10
1.3 Recoil mass separator approach 13

2 Experimental setup **17**
2.1 Accelerator 17
2.2 The recoil mass separator ERNA 18
2.3 Acceptance 20
2.4 Ion identification 28
2.4.1 The ΔE-E telescopes 28
2.4.2 ToF–E detection system 31
2.5 The ^{3}He recirculating gas target 35
2.5.1 Target thickness 38
2.5.2 Density profile 40
2.5.3 Target and beam contaminations 42
2.6 γ-rays detector array 45

3 Experimental procedures and data analysis **51**
3.1 Recoils measurements 51
3.2 Prompt γ-rays measurements 57
3.3 Activation measurements 62

4 Results **69**
4.1 Experimental results 69

4.2 $S_{34}(0)$ extrapolation 73
4.2.1 Choice of the model 73
4.2.2 $S_{34}(0)$ 75
4.3 Impact on astrophysics 79

Summary and Outlook **81**

Appendices **83**

A Basic concepts of nuclear astrophysics **83**

B Data tables **87**

Bibliography **95**

Acknowledgments **99**

Introduction

The ^{3}He$(\alpha,\gamma)^7$Be reaction determines the flux of the ^{7}Be neutrinos from the Sun. The pioneering cross section measurement of Holmgren and Johnston [Hol59] was the basis for the first estimates of solar neutrino fluxes and the planning of the first neutrino observatory at the Homestake mine. Since then many experimental efforts have been devoted to the solar neutrinos: GALLEX/GNO/SAGE, Kamiokande, Super-Kamiokande, Sudbury Neutrino Observatory (SNO), and the more recent Borexino and KamLAND. Recently the Borexino experiment [Arp08] determined the ^{7}Be flux with high accuracy. Nevertheless the ^{3}He$(\alpha,\gamma)^7$Be cross section still represents the largest nuclear uncertainty in the prediction of the flux of solar neutrinos. The ^{3}He$(\alpha,\gamma)^7$Be reaction was considered as a possible key to solve the solar neutrino puzzle before the successful experiments of SNO [Ahm02] and KamLAND [Abe08] proofed the existence of neutrino oscillations and gave an explanation of the observed solar neutrino deficit in the neutrino detectors. The continuous growing of observational data opens a new era of neutrino spectroscopy, in which the solar neutrino fluxes serve as a probe for details of the standard model of particle physics. In particular, the precise knowledge of the different neutrino fluxes can be used to understand physical and chemical properties of the sun, provided that nuclear reaction cross sections are known with similar accuracy. It appears possible to exploit neutrinos from the CNO-cycle and the pp-chain to determine the primordial solar core abundances of C and N [Hax08], if the uncertainties in nuclear cross sections, neutrino observations and neutrino oscillation parameters will be significantly reduced. In the case of the cross section $\sigma(E)$ of the ^{3}He$(\alpha,\gamma)^7$Be reaction, a precision of 3% or better should be achieved [Bah04, Hax08].

The ^{3}He$(\alpha,\gamma)^7$Be reaction has also important implications on the Big Bang Nucleosynthesis. A detailed comparison of the abundances of the primordial elements predicted by the cosmological models with astronomical observations demonstrate an overall good agreement. However, the predicted abundance of ^{7}Li, that depends also from the ^{3}He$(\alpha,\gamma)^7$Be cross section, is a factor 2 to 3 larger than observation. Therefore a precise and accurate evaluation of $\sigma(E)$ is the necessary basis for possible solutions of the so called ^{7}Li *problem*.

In this work I present the results of a new approach, where $\sigma(E)$ of ^{3}He$(\alpha,\gamma)^7$Be was determined by the direct detection of the ^{7}Be recoils using the European Recoil mass separator for Nuclear Astrophysics (ERNA) at the Dynamitron Tandem Laboratorium of the Ruhr-Universität Bochum. The capture γ-rays were also detected in coincidence with the recoils at selected energies, thus allowing a direct comparison of σ with the cross section for γ-ray emission, σ_γ. The measurements with the *activation* method that made use of the ERNA ^{3}He gas target will be also presented.
In the first chapter the role of the ^{3}He$(\alpha,\gamma)^7$Be reaction in the solar neutrino physics and in Big Bang Nucleosynthesis is sketched. The experiments devoted during the last decades to the determination of $\sigma(E)$ at the relevant energies for Big Bang Nucleosynthesis and stellar core hydrogen burning will be reviewed. A brief introduction to recoil mass separator principles is also given. In the second chapter the recoil separator ERNA is illustrated. In particular are presented the modifications to the experimental setup to match the requirements of ^{3}He$(\alpha,\gamma)^7$Be. In the third chapter the data collection and the analysis are described. In the last chapter I will discuss the experimental results, with emphasis on the comparison with previous experimental works and models. The implications of the results for astrophysics will be outlined. Finally some closing remarks are drawn.

Chapter 1

The ^{3}He$(\alpha,\gamma)^7$Be reaction

In this chapter I will introduce the ^{3}He$(\alpha,\gamma)^7$Be reaction. In the first section its role in the astrophysical framework is illustrated and the issues related to the large uncertainty that still affects the determination of the cross section are discussed. The experimental works so far performed are reviewed in the third section. In the last section, the novel approach for the measurement of the cross section with a recoil mass separator, used in the present work, is presented.

A short introduction to the basic concepts of nuclear astrophysics is presented in appendix A, a comprehensive treatment can be found in [Rol88].

1.1 ^{3}He$(\alpha,\gamma)^7$Be in astrophysics

In astrophysics the ^{3}He$(\alpha,\gamma)^7$Be reaction plays a fundamental role in two different scenarios. One is the cosmological nucleosynthesis of light elements in the early universe, known as Big Bang Nucleosynthesis (BBN). The other is the stellar hydrogen burning, since ^{3}He$(\alpha,\gamma)^7$Be is one of the reactions of the so called proton-proton chain (pp-chain) and has a significant influence on the high energy part of the solar neutrino spectrum. The relatively large uncertainty on the ^{3}He$(\alpha,\gamma)^7$Be cross section, $\sim$ 20% as will be discussed in the next section, is one of the largest contribution to the uncertainty on theoretical predictions on the primordial abundance of ^{7}Li and the solar neutrino fluxes.

1.1.1 Big Bang Nucleosynthesis

The BBN is an extremely vast field and even a short introduction to its basic features is beyond the scope of this work. Only some of the key aspects of BBN related to ^{3}He$(\alpha,\gamma)^7$Be reaction will be recalled, more extensive treatments can be found e.g. in [Mal93, Oli00, Cyb04, Kne04, Ioc08].

Any cosmological theory has to explain four fundamental features of the present universe: its expansion, the abundance of light elements, the cosmic background radiation and the baryon-to-photon ratio. The most credited theory that explains all of these features is the Big Bang model. In this framework the production of the first elements occurs by means of the BBN. The theory of BBN consists of following the micro physics of weak interaction and nuclear reactions in the cosmological context of an expanding, cooling universe. The essential aspects of BBN can be seen as a competition between the cosmic expansion rate and particle reaction rates[1]. The nuclides are created, and destroyed, at a rate that depends on their nuclear properties, but also on the interaction energy and the density, both governed by the expansion rate of the universe.

The reaction rates can be established only if the nuclear input parameters, i.e. the probability for a binary nuclear reaction to occur as function of the energy, are well known. The uncertainty on the experimental values will reflect in the uncertainty on the model predictive power.

Standard BBN (SBBN) is the simplest formulation of the theory in the context of the Particle Standard Model. Within SBBN the content of baryons of the universe is set once for all at the beginning and the corresponding density n_B is the only adjustable/free parameter of the theory, while the number of free neutrinos families is fixed to 3 and the neutron lifetime to its experimentally determined value. The number of photons n_γ is also a constant after the temperature drops below 3×10^9 K, about 14 s after the Big Bang, and almost all positrons annihilate with electrons. Thus SBBN uses more conveniently as the free parameter $\eta = n_b/n_\gamma \sim 10^{-9}$, where n_b and n_γ are the baryon and photon density, respectively.

The hot initial phase of the expansion of the universe is dominated by relativistic particles interacting via the weak interaction. It is believed that the present understanding of the weak interaction is such that the uncertainty related to the model of this phase *do not introduce an appreciable uncertainty* [Fie06] on the calculation results. The initial phase determines the ratio of protons to neutrons at the time the conditions of temperature and density allow the stable binding of a neutron and a proton in a deuterium (d) nucleus through the $p(n,\gamma)d$ reaction, about 10^2 s after the Big Bang. The synthesis of heavier elements occurs through a network of many nuclear reactions that leads to the production of astrophysically interesting abundances of deuterium d, ^{3}He, ^{4}He, and ^{7}Li. These abundances are mainly determined by a set of 9 major reactions along with the $p(n,\gamma)d$ reaction and the neutron lifetime. Those are the reactions involving deuterium: $d(d,p)t$, $^3\mathrm{He}(n,p)t$, $d(d,n)^3\mathrm{He}$, $d(p,\gamma)^3\mathrm{He}$; the ones producing ^{4}He: $^3\mathrm{He}(d,p)^4\mathrm{He}$, $t(d,n)^4\mathrm{He}$. The gap at $A = 5$ is overcome and the produc-

[1] The definition of reaction rate is given in appendix A

tion and destruction of mass $A = 7$ are mainly regulated by: $^3\mathrm{He}(\alpha,\gamma)^7\mathrm{Be} \rightarrow {}^7\mathrm{Li} + e^+ + \nu_e$, $t(^4\mathrm{He},\gamma)^7\mathrm{Li}$, $^7\mathrm{Be}(n,p)^7\mathrm{Li}$, $^7\mathrm{Li}(p,\alpha)\alpha$. The gap at $A = 8$ prevents the production of heavier nuclei in any relevant amount [Ioc07]. The network formed by these reactions is illustrated in figure 1.1.

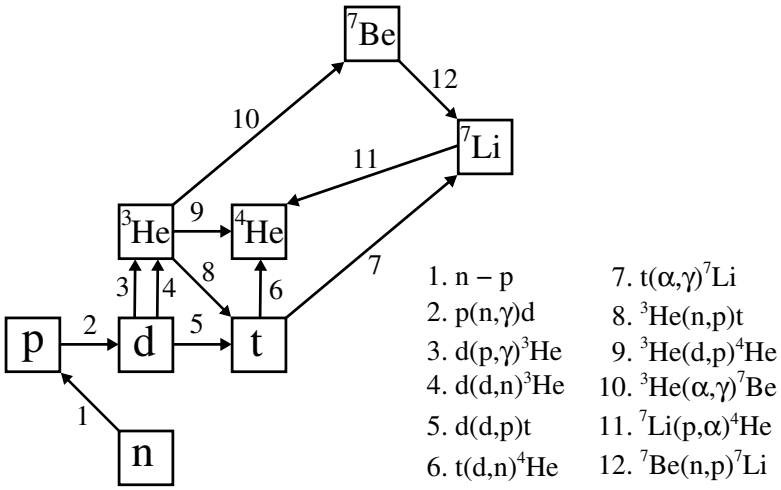

Figure 1.1: Network of the major reactions involved in SBBN calculations.

The aim of BBN is to establish how the mass flows through the network. The effective synthesis of nuclei happens in a range of temperature $1.2 \times 10^9 \gtrsim T \gtrsim 3 \times 10^8$ K, that converts in centre of mass energies *relatively* high for the various reaction, i.e. accessible in a laboratory with the present experimental techniques. For the $^3\mathrm{He}(\alpha,\gamma)^7\mathrm{Be}$ reaction the significant energy interval is $180 \lesssim E_{\mathrm{cm}} \lesssim 400$ keV. On the basis of the experimental determined nuclear reaction cross sections it is possible to calculate expected abundances as a function of the free parameter η. Comparison against the observed primordial abundances can be used to infer the value of η and then estimate the initial baryon density. The uncertainty on the calculated abundances are determined by the uncertainties on the reaction rates.

The Cosmic Microwave Background (CMB) acoustic oscillations, generated somewhat like 4×10^5 years after the Big Bang, when the electrons got bound to the nuclei to form atoms, are also sensitive to the initial mass distribution, and therefore to η. The Wilkinson Microwave Anisotropy Probe (WMAP) has recently measured the CMB power spectrum with high sensitivity [Hin09] and the high precision determination of $\eta = 6.23 \pm 0.17$ was derived. This value is currently used as input parameter for SBBN to interpret primordial abundances, rather then being directly derived from the observations as discussed. A comparison of the abundances of the primordial elements (D, ^{3}He, ^{4}He, ^{7}Li) predicted by BBN with astronomical observations demonstrate a good agreement for the D, ^{3}He and ^{4}He abundances.

The abundance of ^{7}Li shows the largest discrepancy between prediction and observation, see figure 1.2. The ^{7}Li is mainly produced and destroyed by the re-

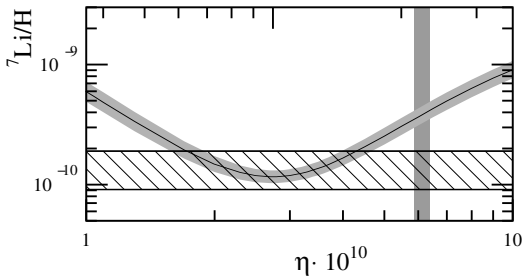

Figure 1.2: Abundance of ^{7}Li calculated by SBBN [Cyb04] as function of η, solid line, the 1σ uncertainty is given by the shaded area. The obervational data $^7\mathrm{Li/H} = \left(1.23 \pm 0.06^{+0.68}_{-0.32}\right)\times 10^{-10}$, 95% C.L., is represented by the horizontal dashed area. The 1σ WMAP η determination is represented by the vertical stripe. The disagreement between prediction and observations is clear.

actions listed above, therefore the cross section for all of these reactions, and the corresponding uncertainties, have to be experimentally determined. To the uncertainty on the calculated ^{7}Li abundance contributes significantly, by more than 50% [Cuo04], the uncertainty on the ^{3}He$(\alpha,\gamma)^7$Be cross section.
The reason for the disagreement is not yet identified. There are several factors that can be responsible, including physics beyond the standard model, better approximations in relativistic cosmology, etc. In any case it seems that the SBBN model has to be extended to include other aspects. This is at present a very active field, many different forms of non-standard BBN have been proposed, some of them are reviewed in [Col02].
It is also widely debated whether the observed abundances are reliable. Since the near universe is far from reflecting its primordial conditions, the methods developed to infer primordial yields have to deal with all sorts of complications. Observations are performed on highly evolved systems where reprocessing, astration, and contaminations from younger systems are possibly present and difficult to correct for. Then relevant systematic errors are involved and are to a large extent irreducible and intrinsic to the astrophysical determinations themselves.
A *stellar* solution to the ^{7}Li discrepancy, the depletion due to processing in star cores, has been proposed by [Kor06], its validity is under debate.

It was argued whether the disagreement between observation and calculations could have been due to wrong estimation of reaction rates. For what concerns ^{3}He$(\alpha,\gamma)^7$Be, any variation in its rate reflects in an almost directly proportional variation in the ^{7}Li abundance, $^7\mathrm{Li}/H \propto S_{34}^{0.96}$ [Cyb04]. This happens because ^{7}Li

is instantly destroyed due to the large cross section of ^{7}Li$(p,\alpha)\alpha$, while the probability for the ^{7}Be$(p,\gamma)^8$B is much smaller. The half-life of the electron capture of ^{7}Be produced by ^{3}He$(\alpha,\gamma)^7$Be is long enough that ^{7}Be survived until the proton density and energy is low enough to freeze out the ^{7}Li abundance.
It was observed [Coc04] that an underestimation of the ^{7}Be$(d,p)2\alpha$ and ^{7}Be$(d,\alpha)^5$Li cross sections could have been the source of the discrepancy, but the measurement of [Ang05] excluded this possibility. Any other nuclear solution to the discrepancy looks unlikely [Cyb04].

A precise determination of ^{3}He$(\alpha,\gamma)^7$Be cross section is not going to solve the ^{7}Li discrepancy, but in the epoch of the *precision cosmology* it will decrease the uncertainty on the model predictions and better constrains the underlying physics.

1.1.2 Solar neutrinos

The energy production in the Sun take place by converting four protons in one ^{4}He nucleus. At the solar core temperature, $T_\odot \simeq 1.5\times10^7$ K, the more effective way, about 99% of the total, occurs by the series of reactions shown in figure 1.3, the so called pp-chain, that contain the ^{3}He$(\alpha,\gamma)^7$Be reaction. The remaining 1% occurs

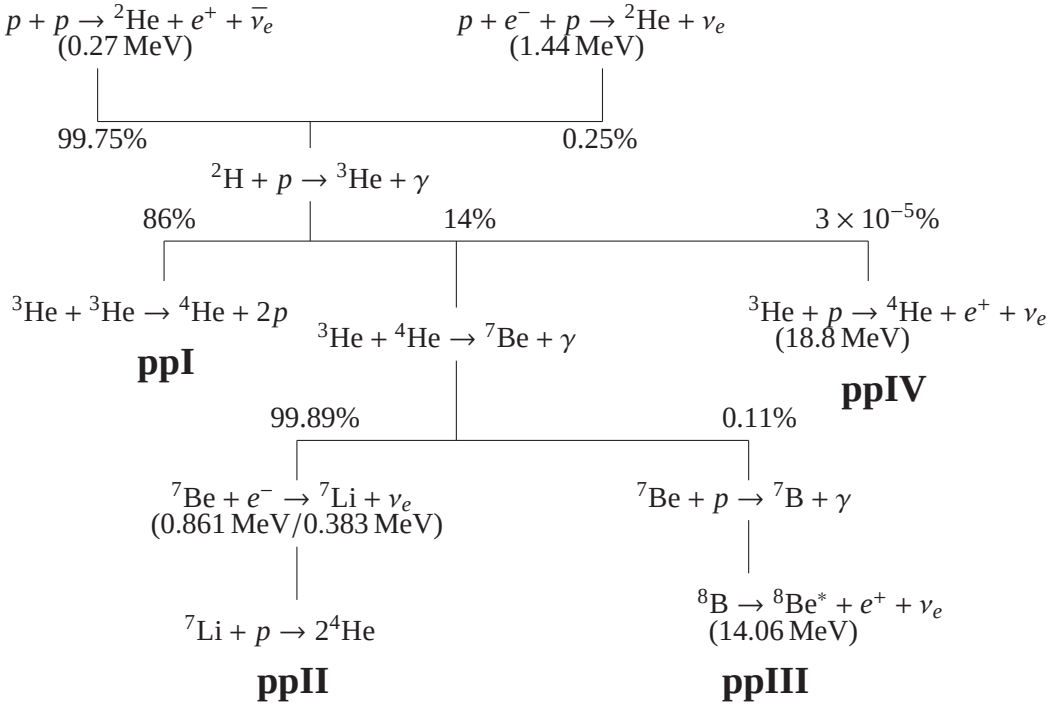

Figure 1.3: Schematic representation of the pp-chain, with the four possible terminations ppI-ppIV. The emitted neutrinos are indicated together with their maximum energies.

through the CNO cycle, see e.g. [Rol88]. The huge amount of observations about the Sun, and main sequence stars, permits a detailed modelling of the hydrogen burning phase. The Standard Solar Model (SSM), see e.g. [Bah05], summarises this knowledge for the Sun. This model requires as inputs the luminosity, the radius, the initial metallicity, i.e. the abundance of elements heavier than helium, the opacities and the nuclear reaction rates of the nuclear reactions involved.
At the temperature $T_\odot$ the corresponding centre of mass energy for the reactions is a few tens of keV, and correspondingly the cross sections are extremely small, due to the Coulomb barrier. Therefore usually cross sections are measured at energies higher than the corresponding Gamow peak[2], and then are extrapolated to the proper energy on the basis of a nuclear model.
As regards the *pp*-chain, the cross section of the $p(p,e^+\nu_e)^2$H reaction is prohibitively low for the present experimental techniques to be measured. All the other nuclear input parameters have been determined. Only the ^{3}He$(^3$He$,2p)^4$He and the $d(p,\gamma)^3$He have been measured at the Gamow peak energies, all the others rely on extrapolation. For the ^{3}He$(\alpha,\gamma)^7$Be reaction the Gamow peak energy in the Sun is 22 keV. At this energy the cross section is expected to be $\sim 1.5\times10^{-17}$ barn. The rate of ^{3}He$(\alpha,\gamma)^7$Be is, at the present status, the one with the largest experimental uncertainty. The experimental uncertainties are reflected in the uncertainty of the SSM predictions.
One of the predictions that can be derived from the SSM is the neutrino energy spectrum, shown in figure 1.4, that is a direct observable of the nuclear reactions occurring in the interior of the Sun. The ^{7}Be contributes with the neutrinos emitted by its electron capture decay to ^{7}Li. The main neutrino flux, dominating the low energy part of the spectrum, is due to neutrinos emitted by the $p+p$ reaction. The high energy part of the spectrum is mainly produced by the β-decay of ^{8}B, and a significant contribution is given by the ^{7}Be neutrino. The relative intensity of the two fluxes is determined by the relative rate of ^{3}He$(\alpha,\gamma)^7$Be with respect to the rate of ^{3}He$(^3$He$,2$p$)^4$He.
The neutrino observatories are mainly sensitive to the high energy component of the neutrino spectrum. The discrepancy of the observed flux in the Homestake neutrino observatory compared to the predicted one, the so called *solar neutrino puzzle* (see e.g. [Bah82, Bah00]), generated a huge amount of theoretical and experimental efforts in the '70 and '80. Lots of these efforts were devoted to ^{3}He$(\alpha,\gamma)^7$Be, since it was suspected that its cross section could have been overestimated. This hypotesis was ruled out by the measurements that essentially confirmed the existing data. Later the Gallex experiment found that also the *pp* flux was reduced in intensity with respect to the predictions [Ans92]. Thus more complicated scenarios were suggested, like the old suspicion on the presence of

[2]For the definition of the Gamow peak see Appendix A.

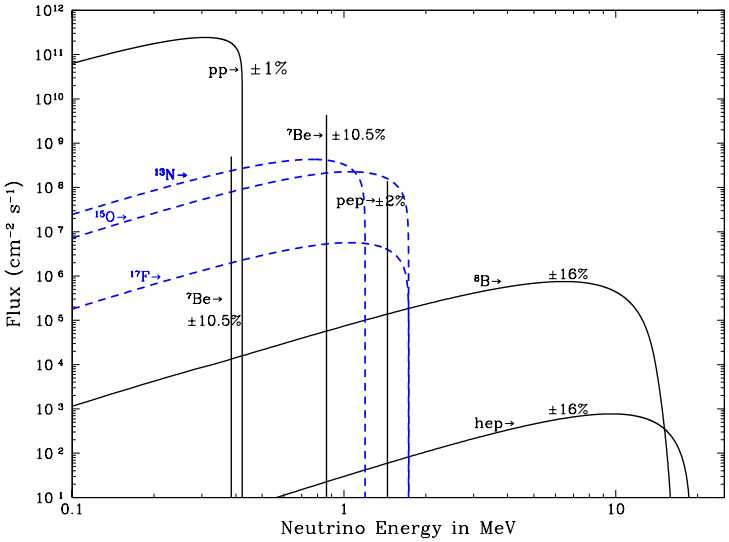

Figure 1.4: Solar neutrino spectrum as calculated in [Bah05].

a resonance in the Gamow peak of the ^{3}He(^{3}He, $2p$)^{4}He reaction. The important measurement of [Bon99] excluded this possibility. The nuclear input parameters are now well grounded and the puzzle cannot be fixed by changing other SSM input parameters, the hypotesis of neutrino oscillations gained confidence. The solar neutrino flavour mixing was experimentally verified by the results of the Sudbury Neutrino Observatory (SNO) [Ahm02].

Nevertheless, the interpretation of the experimental results of the various neutrino observatories relies on the SSM. While the available experimental data increase, e.g. the observed ^{7}Be neutrino has been recently determined with high precision by [Arp08], an improved precision on the prediction of the neutrino fluxes is crucial to better determine the parameters governing solar neutrino oscillations.

In addition, if the uncertainties in nuclear cross sections, neutrino observations and neutrino oscillation parameters will be significantly reduced, it appears to be possible to exploit neutrinos from the CNO-cycle and determine the primordial solar core abundances of C and N [Hax08]. This would be a direct probe of the Sun's core metallicity, that might provide a check on the major SSM assumption that equates surface and zero-age core metallicity, that at present has no experimental support.

1.2 The ^{3}He$(\alpha,\gamma)^7$Be reaction in laboratory

The ^{3}He$(\alpha,\gamma)^7$Be radiative capture reaction is schematically illustrated in figure 1.5. The reaction is exotermic and its Q-value amounts to 1.587 MeV. Once the process takes place the γ-ray emission may occur in two ways, directly to ground state, or through the ^{7}Be first excited state at $E_x = 429$ keV with the emission of the correspondig secondary γ-ray.

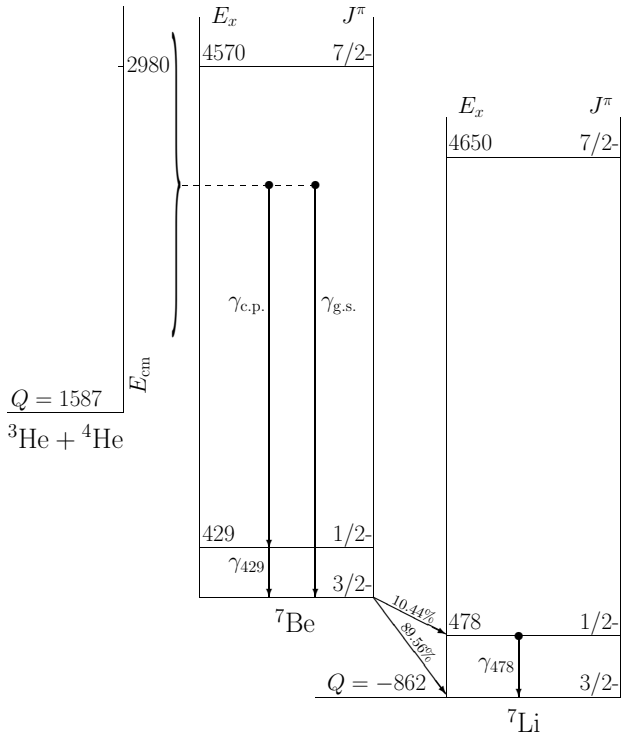

Figure 1.5: Level diagram of ^{7}Be indicating the possible γ-ray transitions, as well as the relevant Q values and quantum numbers of the various excited states. All energies are in keV.

The ^{7}Be is an unstable nucleus, it decays by Electron Capture (EC) to ^{7}Li with the emission of an electron neutrino ν_e. The half-life is 53.22 ± 0.0653 days [Til02]. The Q-value of the process is 862 keV, that is the energy of the neutrino if the ^{7}Li is created in its ground state. With a probability of (10.44 ± 0.04)% [Til02] the decay populates the first ^{7}Li excited state at $E_x = 478$ keV and the characteristic γ-ray of the same energy is emitted. In this case the energy of the neutrino is $Q - E_x = 384$ keV.

In the energy range so far exploited by experiments the ^{3}He$(\alpha,\gamma)^7$Be cross

section shows a smooth variation with energy, an almost isotropic γ-ray angular distribution and no spin variation. Those properties are characteristic of a direct capture process [Chr61]. Such a process is said to be an *external* process, i.e. the capture occurs by electromagnetic interaction at a distance larger than the range of the strong interaction. For this reason the cross section is supposed to be not very sensitive to the detailed nuclear structure of the particles involved.

Direct-capture model calculations of different complexity yield nearly identical energy dependence of the low-energy S factor[3]. The calculations can be grouped in two classes: potential models, e.g. [Tom63] and microscopic models (e.g. microscopic cluster model, resonating group method, etc.) [Liu81, Kaj84, Lan86, Kaj87, Moh93, Csó00, Nol01]. The energy behaviour of the S factor, according to the potential models, is almost fixed by the spectroscopic factors. Common to all of these models is the assumption that the ^{7}Be nucleus has a dominating cluster structure as ^{3}He+^{4}He.
In the work of [Csó00] the ^{3}He$(\alpha,\gamma)^7$Be was studied with an extended cluster model, i.e. with the inclusion of ^{6}Li$+p$ cluster states. According to their calculation the low energy slope of the S-factor changes if the extended cluster is accounted and/or a different nucleon-nucleon interaction is used. This induces the authors of [Csó00] to question the use of a pure direct capture model to describe the ^{3}He$(\alpha,\gamma)^7$Be process.
The R-matrix approach used by [Des04] to fit the experimental data, essentially reduces to a potential model calculation, due to the non-resonant nature of the reaction in the energy range considered.

Measurements of the ^{3}He$(\alpha,\gamma)^7$Be cross section have been performed so far by two different techniques.
The first method, known as *prompt* γ, is based on the detection of the capture γ-rays emitted in the reaction. Measurements using this approach were performed by [Par63, Nag69, Krä82, Ale84, Hil88].
The second method utilized, known as *activation* or *delayed* γ, is performed by measuring the activity of the synthesized ^{7}Be. This is possible detecting the γ-rays emitted in the ground state transition of the first excited state of ^{7}Li. This approach was used in the works of [Rob83, Vol83, Nar04].
In the work of [Osb84, Bro07] and [Con07] both approaches were used. The latter summarises the results of all the measurements performed at the Laboratory for Underground Nuclear Astrophysics (LUNA), i.e. also the measurements of [Bem06] and [Gyü07] performed by activation only. The LUNA measurements are presented also in [Cos08].
The experiments span a centre of mass energy interval $150\,\text{keV} \leq E_{\text{cm}} \leq 2.5\,\text{MeV}$,

[3] For the definition of the S-factor see Appendix A.

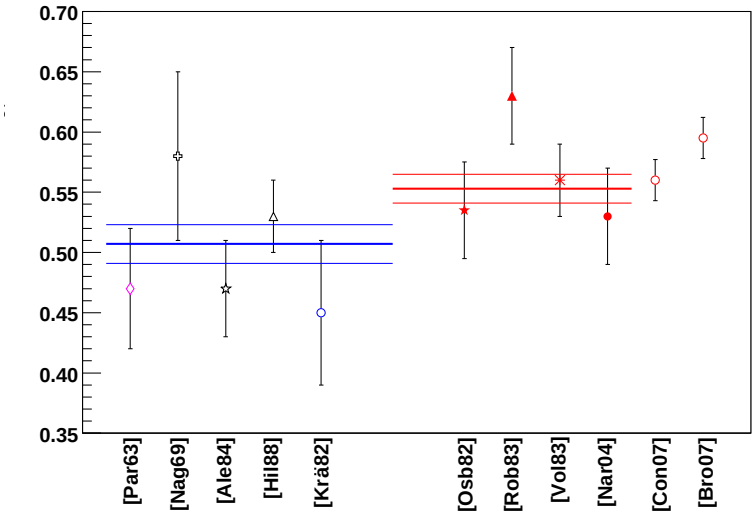

Figure 1.6: Published extrapolated S_{34} values for the various experiments. The horizontal thick line is the weighted average of the values available at the time when this work was planned, grouped by the measurement technique; the thin lines represent 1σ deviation.

whereas the energy range $E_{\mathrm{cm}} > 1.2\,\mathrm{MeV}$ was covered only by [Par63]. The lower limit is essentially set by the extremely small counting rate. The beam induced background usually makes prompt γ-rays measurements difficult to perform above $E_{\mathrm{cm}} \gtrsim 1.2\,\mathrm{MeV}$.

The results of the different experiments are summarized in figure 1.6 in the form of the extrapolated $S_{34}(0)$, the value of the S-factor at solar core temperature. Note that the result of [Krä82] is renormalized by a factor of 1.4, as suggested by [Hil88]. The renormalization is needed due to an incorrect evaluation of the total target thickness. In the work of [Hil88] no error on the scaling factor was quoted, from the data reported in table 2 of [Krä82] it should be assumed to be $\sim 28\%$.

It was noted by [Ade98] that averaging the values, available at that time, grouped by measurement technique the means obtained were not compatible to each other. It was argued whether this effect was due to the presence of systematic errors in one or both of the techniques, or perhaps to the presence of a non radiative channel, like internal conversion or pair production, to which prompt γ-ray experiments would not be sensitive. The results of [Bro07, Con07] exclude this latter hypothesis. These works have been published after the beginning of the present work, solving the *discrepancy* was still a strong motivation for the start of the present work.

The ratio of the intensity of the transition through the first excited state with respect to the transition intensity to ground state, $\sigma_{429}/\sigma_{g.s.}$ was measured by

[Par63, Nag69, Krä82, Ale84, Osb84]. It is worthwhile to note that the results of [Par63] are about 10% lower than the results of all the other experiments. The origin of this discrepancy is difficult to identify, but might influence the determination of the cross section.

Angular distribution of prompt γ-rays were measured only by [Krä82] at various energies up to $E_{\mathrm{cm}} = 1.29\,\mathrm{MeV}$. Results were found, for all energies but one, compatible with the *almost isotropic* prediction of [Tom63].

1.3 Recoil mass separator approach

Another method to measure $^{3}\mathrm{He}(\alpha,\gamma)^{7}\mathrm{Be}$ cross section, with different systematics and improved statistical precision, is the direct detection of the ^{7}Be recoils produced in the reaction.

In a radiative capture reaction if the target is thin enough the recoils leave the target together with the particles of the primary beam, at a very small intensity ratio. The ratio of recoils to projectiles is 10^{-12} for a cross section of $1\,\mu$barn and a target thickness of $1 \times 10^{18}\,\mathrm{atoms\,cm^{-2}}$, typical values of nuclear physics experiments. Presently there is no detector to be placed directly after the target that can accomplish the task of discriminating and counting the recoils. Thus the primary beam has to be filtered out in order to achieve a reasonable ratio to allow direct detection. This task is accomplished by a Recoil Mass Separator. The separation of ions can be performed by means of different type of filters: magnetic, that selects ions according to rigidity, ratio of ion's momentum and charge p/q; electric, that selects ions according to the energy to charge ratio, E/q; velocity, that selects on ion's velocity v regardless of the charge state. A combination of different type of filters must be used to achieve mass separation, then the separator discriminates the recoils in one of all possible charge states.
The high detection efficiency for particles like the recoils produced in the reaction is a major improvement. High precision measurements can be obtained in much shorter measurement time compared to the other techniques.
Some large corrections needed in γ-ray measurements can be avoided. In fact due to the low efficiency of γ-ray detection usually high density gas target and/or high intensity particle beams have to be used. It is known that in such conditions local modifications of the target density occur under beam irradiation: the *beam heating effect* [Gör80]. For this reason sizable corrections (5-15%) have to be applied to obtain the cross section. The high detection efficiency of the recoil separator approach allows for lower density and/or lower beam intensity, thus avoiding these systematic uncertainties.
The recoil separator approach is an essentially background free measurement technique, that permits easily to expand the measurements toward the *higher en-*

ergy range, barely accessible to γ-ray measurements due to the beam induced background.

The cost is a complicated experiment. In fact, the typical energy range spanned by nuclear astrophysics, makes the task of recoils collection extremely difficult. The first issue to deal with is to allow the recoils emerge from the target. The low energy of the recoils, in the order of a few hundred keV per nucleon, requires the target to be gaseous. The same reason makes impossible to have the gas confined by thin windows, that would in any case limit the beam to extremely low intensities. Therefore a windowless, differentially pumped, gas target is needed. The gas target used for this work will be illustrated in section 2.5.
The selection and transport of the recoils is complicated by their angular and energy spread. Consider the reaction induced by the projectile A on target x producing the recoil B, $x(A,\gamma)B$. Due to momentum conservation projectiles and recoils have essentially the same momentum, $p_A \simeq p_B$, but because of the different mass have different velocities. Nevertheless the γ-ray emission leads to an angle and energy distribution of the recoils according to the following equations. The energy of the photon for a ground state transition in the centre of mass framework is

$$E_\gamma = \left[\sqrt{1+\frac{2(E_{\rm cm}+Q)}{m_B c^2}}-1\right]\cdot m_B c^2 \simeq E_{\rm cm}+Q \ .$$

where Q is the Q-value of the reaction, m_B the recoil's mass and c the speed of light. Being E_γ/c the momentum of the photon and p_B of the recoil, the latter emerge from the target with an angle in respect to the beam direction

$$\theta_{\rm lab} = \arctan\frac{p_{B\perp}}{p_{B\parallel}} = \arctan\left(\frac{\sin\theta_\gamma}{\frac{c}{E_\gamma}p_A-\cos\theta_\gamma}\right) \ , \tag{1.1}$$

where θ_γ is the γ-ray emission angle in the centre of mass framework, since usually $v_{\rm cm} \ll c$ the approximation $\theta_\gamma \simeq \theta_{\gamma\rm LAB}$ is made. The energy conservation implies for the recoil energy E_B

$$E_B = \frac{m_A}{m_B}E_{\rm lab}\left[1-2\frac{p_\gamma}{p_A}\cos\theta_\gamma+\left(\frac{p_\gamma}{p_A}\right)^2\right] \ , \tag{1.2}$$

the quadratic term in parentheses is, in the energy range of nuclear astrophysics, negligible. These equations thus relate the recoil angle and energy to θ_γ. In particular the maximum for $\theta_{\rm lab}$, $\theta_{\rm max}$, is reached when $\theta_\gamma = \pi/2$

$$\theta_{\rm max} = \arctan\left(\frac{E_\gamma}{\sqrt{2m_A c^2 E_{\rm lab}}}\right) \ . \tag{1.3}$$

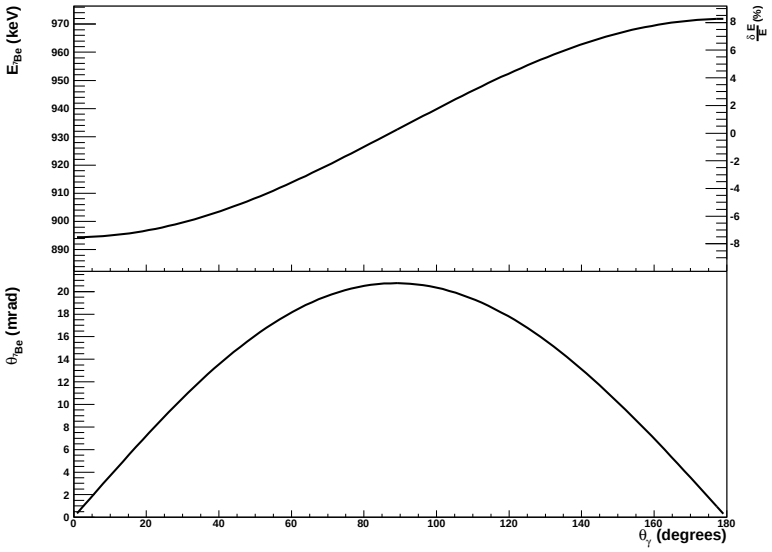

Figure 1.7: Energy (top) and angle (bottom) for ^{7}Be recoils as a function of the γ-ray emission angle θ_γ, according to ^{3}He$(\alpha,\gamma)^7$Be reaction kinematics at $E_{\rm cm} = 700$ keV.

In figure 1.7 are shown, as a function of θ_γ, the energy and the angle of the recoils calculated for ^{3}He$(\alpha,\gamma)^7$Be at $E_{\rm cm} = 700$ keV. As a function of the centre of mass energy, $\theta_{\rm max}$ has a minimum at $E_{\rm cm} = Q$. Note that for the same centre of mass energy $E_{\rm cm}$ in inverse kinematics, i.e. projectiles heavier than the target nuclei, a smaller $\theta_{\rm max}$ is attained.
Corresponding to $\theta_{\rm max}$ the energy of the recoil is

$$\bar{E} = \frac{p_A^2}{2m_B} = E_{\rm lab}\frac{m_A}{m_B} \ . \tag{1.4}$$

For other values of θ_γ the recoil's energy E_B varies in the interval $\bar{E} - \Delta E \le E_B \le \bar{E} + \Delta E$, with

$$\Delta E = 2\frac{E_\gamma}{m_B c^2}\sqrt{2m_A c^2 E_{\rm lab}} \ . \tag{1.5}$$

The minimum of the energy corresponds to γ-ray emission in beam direction, the maximum for backward emission.

To measure the total cross section of a nuclear reaction the separator must have the corresponding *acceptance*, i.e. it has to provide 100% transmission of the recoils, for the selected charge state, for any $\theta_{\rm lab}$ and E_B related by the equations 1.1 and 1.2. Any transmission significantly different from 100% would drastically affect the accuracy on the determination of the cross section, since a realiable correction would require a detailed knowledge of the phase space distribution of

the recoils.
Because of θ_{lab} the recoil's beam diameter grows sizeably after the target. Thus before any filtering the ions need to be focussed toward the beam axis. Moreover also the filter elements, that are usually set to match properties of the recoils with $E = \bar{E}$, will have some effect on the trajectories of the recoils that have an energy different from $\bar{E}$. These effects are compensated with focussing elements too. Therefore a separator is a chain of focussing and filter elements.

The *suppression factor*, defined as the number of projectile particles that reaches the end of the separator (*leaky*) with respect to the total number of impinging particles N_p(leaky)/N_p(impinging), is an index of the separator efficiency. It depends on the projectile ion rigidity, the selected recoil charge state, and the energy. A smaller suppression factor implies a better signal to background ratio, and thus the possibility to measure smaller cross sections.

The recoil separator ERNA used for this work is described in the next chapter.

Chapter 2

Experimental setup

The European Recoil mass separator for Nuclear Astrophysics ERNA has been built to measure the cross section of radiative capture reactions of astrophysical interest.
The setup and commissioning of the separator has been reported in [Rog99a, Rog99b, Rog03b, Gia04, Sch04], the details of the separator elements can be found in [Rog03a].
The $^{12}C(\alpha,\gamma)^{16}O$ reaction is the first case studied with ERNA, because of its importance in astrophysics and the fact that it is an ideal case for the development of the separator. The results are reported in [Sch05] and in deeper detail in [Sch07], in particular the ^{4}He target.

In this chapter a brief overview of the separator is given, then I will concentrate on the modifications of the separator and the target in order to measure the $^3He(\alpha,\gamma)^7Be$ cross section.

2.1 Accelerator

In this experiment the $^3He(\alpha,\gamma)^7Be$ cross section was measured in inverse kinematics, that is using as target the lighter ion ^{3}He and the heavier ^{4}He as the projectile, a choice that will be justified in section 2.3.
The ^{4}He beam was provided by the 4 MV Dynamitron Tandem Accelerator of the Ruhr-Universität Bochum. The negative ion source was of duoplasmatron type, equipped with a lithium exchange channel. In the course of this work the laboratory upgraded to a new duoplasmatron source with a rubidium exchange channel. Typical beam intensities were in the order of 1 pμA on target.
Other beams like H, Li, N, C, O, in some cases provided by a sputter source, were also used for energy loss and density profile measurements.
The beam energy was selected with a precision of $4 \cdot 10^{-4}$ by the 52.5° analysing

magnet, whose calibration was determined in a large range of energies [Bec95]. The ions were injected to the 75° separator's beam line by the switching magnet, see figure 2.1.

2.2 The recoil mass separator ERNA

As discussed in section 1.3, to perform the measurement of ^{3}He$(\alpha,\gamma)^7$Be cross section the separator has to provide a suppression of the primary beam of about 10 orders of magnitude or better. Moreover, the separator has to have the acceptance required by ^{3}He$(\alpha,\gamma)^7$Be kinematics, i.e. up to 25 mrad for angular acceptance and ±4% for energy acceptance (see section 2.3).
A schematic layout of the recoil separator ERNA is presented in figure 2.1. In the figure are also shown the beam preparation stages and the beam purification elements, two Wien filters (purWF1 and purWF2), that provide the necessary beam purity, an issue that will be further discussed in section 2.5.3.
The reaction occurs in the extended windowless ^{3}He gas target, that I will describe extensively in section 2.5.
The separator follows a velocity-rigidity-velocity filtering scheme. Briefly, the first separator element, as close as possible to the target cell, is the quadrupole triplet (QT). This element is needed to bring toward the beam axis the recoils with large angular divergence, preventing them to enter the following element too far from the beam axis. The next element is a Wien Filter (sepWF1), a device that provides an electrical and a magnetic field orthogonal to each other and to the beam axis. This element selects ions according to their velocity, and is responsible for the main primary beam suppression, since beam particles and recoils have the same momentum but, obviously, different speed. Then comes a quadrupole singlet (S1), focusing in the horizontal plane, to compensate for the refocusing effect of sepWF1 on the recoils that have energy different from the one corresponding the velocity on which the filter is set. The second filter element is the 60° dipole magnet, a rigidity filter. This element also has a strong focusing effect on the recoils in the horizontal plane, see figure 2.3, giving them high divergence at its exit. Therefore the next element is again a focusing element, the quadrupole doublet (QD). The last filter element is another Wien filter (sepWF2), that enhances the suppression of the primary beam.
Along the separator are mounted Faraday Cups (FC) for current measurement. Slit systems (SS), movable plates orthogonal to the beam axis, are used for beam diagnostics and suppression enhancement.

The suppression factor of the separator for ^{3}He$(\alpha,\gamma)^7$Be was varying between $\sim 10^{-9}$ and $\sim 10^{-13}$, depending on the selected charge state and recoil energy, as shown in figure 2.2. The leaky beam, projectile ions that reach the end of the

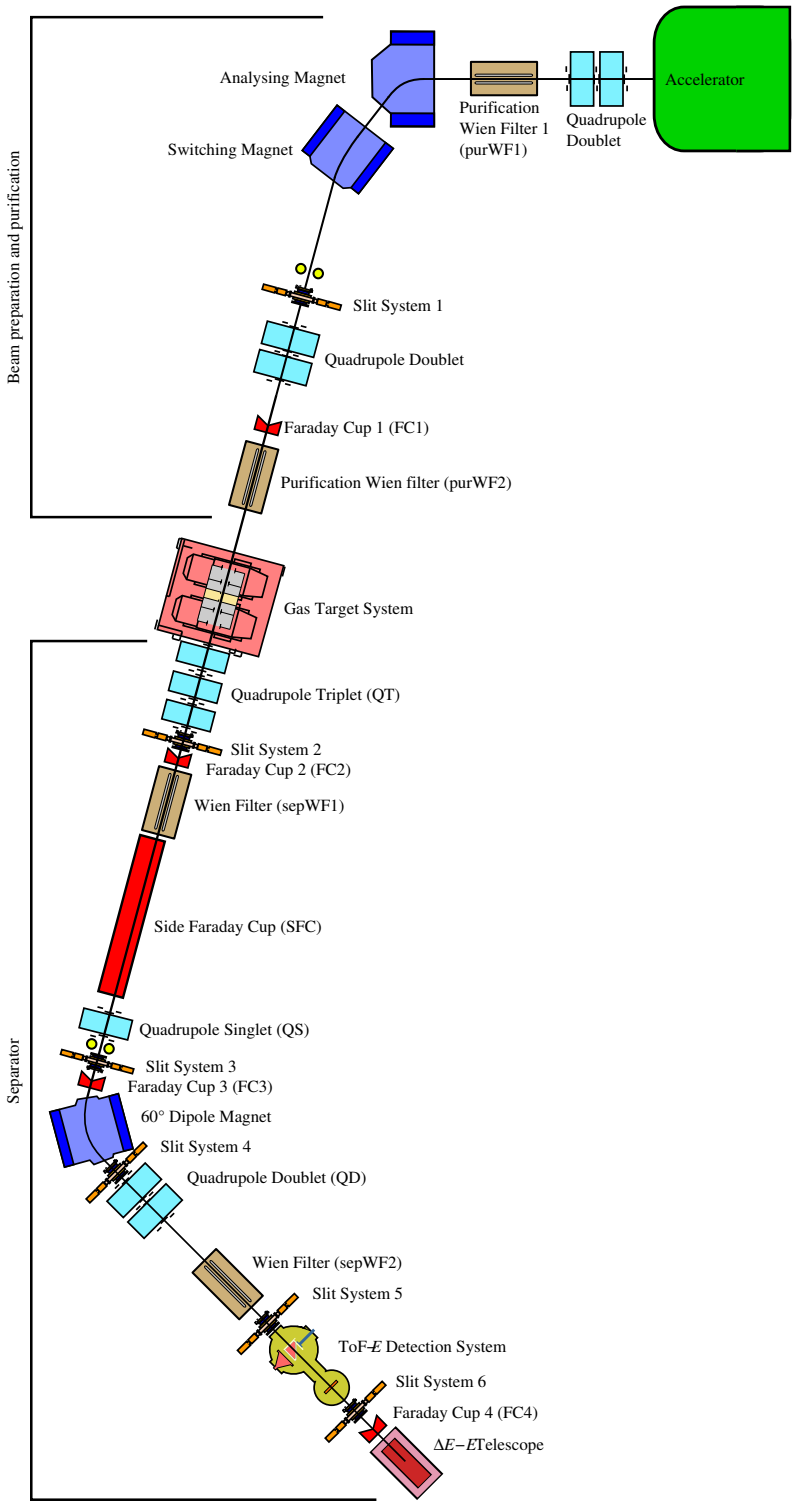

Figure 2.1: Schematic layout of the recoil separator ERNA, not in scale.

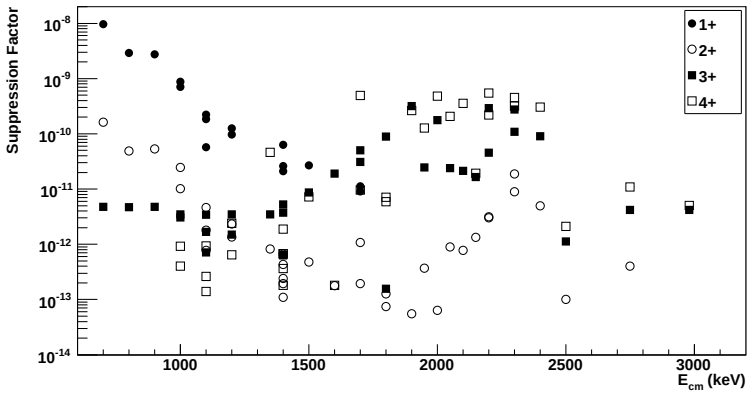

Figure 2.2: Observed suppression factor of the separator.

separator, is likely to be originated mainly by elastic scattering on target collimators and/or sepWF1 plates. To allow ion discrimination and counting at the end of the separator there is the end-line detector. For the measurements of ^{3}He$(\alpha,\gamma)^7$Be cross section three different end detectors were used: a) an ionisation chamber with fractioned anode used as a ΔE-E telescope; b) a similar telescope, with the residual E measured by a large area silicon detector; and c) a Time of Flight-Energy detection system. These detectors are described in detail in section 2.4.
The installation of the ToF–E required some modification to the layout of the separator in the last section. In order to fit the chambers of the ToF–E after sepWF2, the filter was moved upstream by 55.5 cm and the telescope chamber downstream by 15 cm. This configuration was chosen to allow a change from ToF–E to the ΔE-E telescope with minimum amount of work.

2.3 Acceptance

A key requirement for the separator is the acceptance, i.e. the ability of transporting to the end detector 100% of the recoils in the selected charge state q, with energy and angle in the windows defined by the reaction kinematics, equations 1.1 and 1.2.

Calculations of charged ions trajectories can be performed with a formalism identical to the one used in geometric light optics, therefore one refers to them as *optical* calculations. These calculations are used for preliminary studies and optimisations. For these purposes I used the routine written to describe ERNA [Rog03a] for the software COSY Infinity [Ber90]. An example of such calculations is shown in figure 2.3, in red are represented the trajectories for ions emerging from the target with central energy and maximum angular divergence, in blue

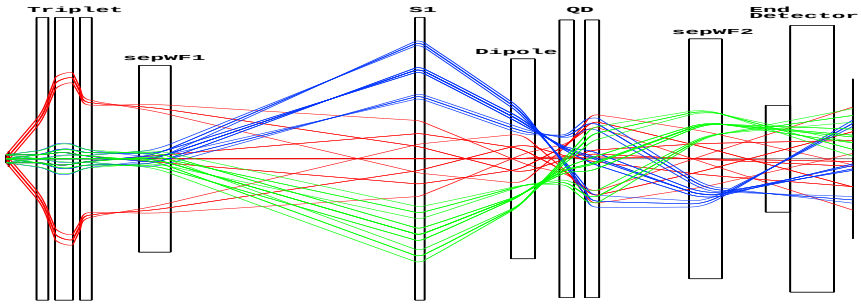

2.3.1: Horizontal plane.

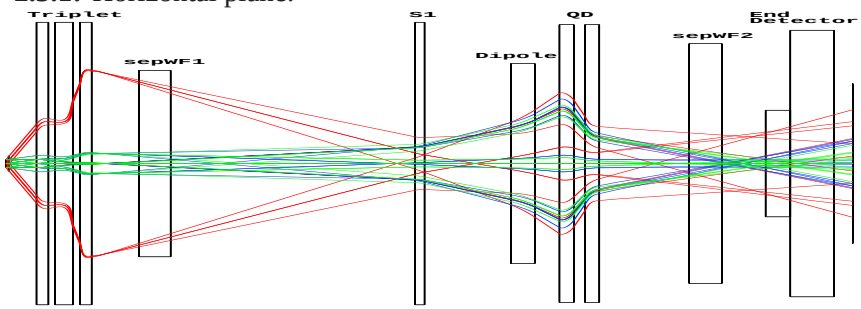

2.3.2: Vertical plane.

Figure 2.3: Optical calculation of ion trajectories at $E_{cm} = 1.2$ MeV. The separator's elements are schematically represented as boxes, the color scheme of the trajectories is explained in the text.

and in green the ones emerging parallel to the beam axis with the lowest and highest energy, respectively (see section 1.3). An important information obtained from the optical calculations is that these trajectories define the outer envelope of the recoil cone. Thus the full transmission of these recoils to the end of the separator grants the transmission of any recoil produced in the reaction. For this reason the acceptance of the separator can be experimentally obtained by verifying, separately, the transmission of the recoils emerging from the target with angle θ_{max}, *angular acceptance*, and of the recoils with minimum and maximum energy, *energy acceptance*.

The full transmission of the recoils to the end detector can be achieved only in a limited region around the centre of the target. This in turn implies that the target atoms must be confined in the region where full acceptance can be obtained. On the basis of the optical calculations this region extends $\sim \pm 40$ mm around the target centre.

Besides the reaction kinematics, the interaction of the recoils with the target gas must be considered to determine the maximum angle θ_{max} for the recoils to

emerge from the target. In fact since the ^{7}Be energy is rather low, $< 700\,\mathrm{keV/amu}$, atomic collisions can modify $\theta_{\max}$ significantly.
To evaluate this effect I performed Monte Carlo (MC) calculations with the software TRIM [Bie03], a program that simulates the transport of ions through matter by means of statistical methods. These calculations have been performed, according to the reaction kinematics, under the following assumptions:

- all recoils are generated at the beginning of the target;
- only ground state γ-ray transition is present;
- γ-rays angular distribution is assumed to be isotropic at all energies;
- the beam profile is assumed to be gaussian with $2\sigma = 1.5\,\mathrm{mm}$, since the typical transmission through a 3 mm diameter at target position was 98%;
- the beam divergence has uniform probability distribution in $\pm 3\,\mathrm{mrad}$, estimated from the typical beam diameter at $\sim 3\,\mathrm{m}$ upstream the gas target.

The angle that includes 99% of the ions is chosen as $\theta_{\max}$.

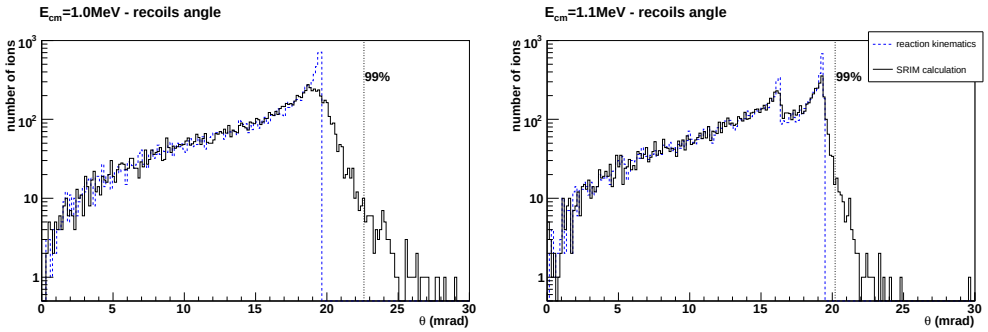

2.4.1: *Conservative* MC calculation. **2.4.2:** Realistic MC calculation.

Figure 2.4: Example of MC calculations for angular straggling of ^{7}Be recoils in target gas. Dashed histogram is the distribution expected from reaction kinematics, while continuous line histogram shows the effect of collisions with the target gas atoms. Vertical dotted line indicates $\theta_{\max}$, see text for details.

The above assumptions, especially the first, grant a large safety margin for the recoil envelope to be within $\theta_{\max}$. An example of such MC calculations is shown in figure 2.4.1. The values of $\theta_{\max}$ obtained in these calculations are the values required for the angular acceptance.
In some cases a more realistic MC calculation was performed. In this calculation the recoil distribution along the beam axis was considered, according to the density profile of the target gas to be discussed in section 2.5. The cascade transition

was also included according to the theoretical estimate of [Liu81]. An example of this MC calculation is shown in figure 2.4.2, it may be noted that the $\theta_{\max}$ value obtained is significantly smaller. Thus the conservative MC calculation always represents an upper limit.

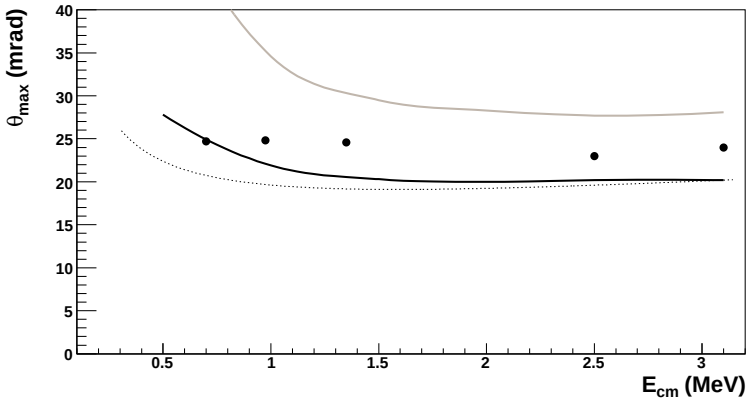

Figure 2.5: Needed angular acceptance for the measurement of the ^{3}He$(\alpha,\gamma)^7$Be cross section in direct and inverse kinematics, grey and black curve, respectively. The filled circles represent the measured acceptance. See text for details.

The results of the MC calculations are summarised in figure 2.5, where the needed angular acceptance for inverse kinematics, solid black line, is shown as a function of the centre of mass energy. The dotted curve is the $\theta_{\max}$ due to the reaction kinematics only. It is clear from the figure that the effect of the target gas is almost negligible at the higher energies, $E_{\rm cm} \sim 3\,$MeV, while becomes relevant and a major limitation at low energies $E_{\rm cm} \simeq 0.7\,$MeV. The solid grey line shows the required angular acceptance for direct kinematics, and is clearly larger than the measured angular acceptance (filled circles), i.e. too large to allow measurements with an ^{3}He beam on ^{4}He target.
The measured angular acceptance values were obtained in the *tuning* of the separator, the procedure used to experimentally determine the fields of the separator elements that grant 100% transmission of the recoils to the end detector. This procedure was needed since the field settings could not be obtained from optical calculations while, although they reproduce closely the separator's features, they lack the necessary accuracy. For some critical fields an accuracy better than 1% was needed. This is due to the fact that not all of the features of *real* devices, like field inhomogeneities, fringe fields, etc., were accurately included in the calculations. The experimentally determined fields did not follow perfectly a scaling law with the recoil charge state and energy, making the scaling of the fields according to rigidity not exact. For this reason the tuning of the separator, and acceptances verification, was carried out at several energies for all the recoil charge states to

be measured.
The tuning procedure consisted in checking the transmission of a pilot beam, by current measurement, from target position (FC2) to the end of the separator (FC4), see figure 2.1. The properties of the pilot beam must be close to the recoil beam. These properties are rigidity, mv/q, energy spread, and angular divergence. The only stable element of nuclear mass 7 is Lithium, thus the best candidate to be the pilot beam for ^{3}He$(\alpha,\gamma)^7$Be measurements. Since the accelerator handles ions of any energy up to $(q+1)*4\,$MeV, the first two properties are usually easily obtained, except for the 4+ charge state not available for ^{7}Li.
Angular divergence is achieved by means of an electrostatic deflection unit, two aluminium plates of length $l = 200\,$mm at distance $d = 14\,$mm placed at target position. A scheme of the deflection unit is shown in figure 2.6. The device is

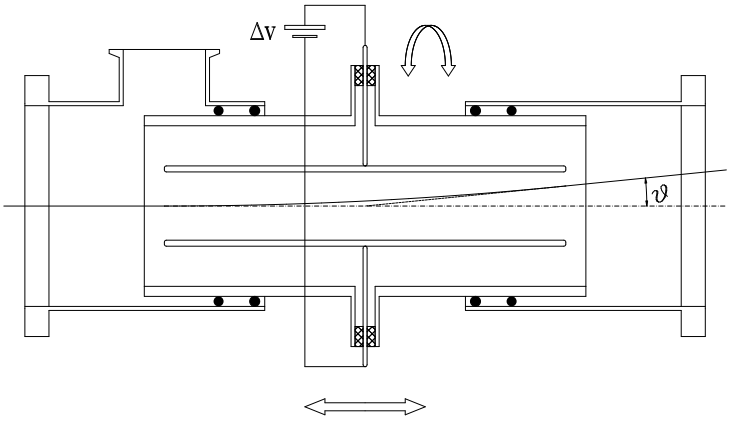

Figure 2.6: Electrostatic deflection unit used for the separator tuning.

described in [Rog03a]. It was modified in order to be able to rotate it at any polar angle ϕ around the optical axis and to be shifted by $\sim 40\,$mm upstream and downstream of the central position without breaking the vacuum, as described in [Sch04, Sch07].
Applying to the plates a voltage ΔV the beam is deflected by an angle

$$\vartheta = \arctan\left(\frac{q\Delta V l}{4dE}\right) \ ,$$

where q and E are respectively the charge state and the energy of the ions. The trajectory is like originating at the middle point between the plates. The possibility to rotate the plates around the optical axis allowed to mimic the whole recoil cone. The ability of being moved along the beam axis allowed to check for transmission on a large fraction of the target extension.
The separator has a high sensitivity to the particle entrance angle with respect to the optical axis. This imposes that the impinging beam, pilot or projectiles, has

to enter the separator on the optical axis. Great care was paid to the focusing and the alignment of the incident beam. A transmission of the order of 98% or better through an aperture of $\phi = 3$ mm located on optical axis at the target position was required. The alignment was verified by determining the beam position at FC3, ~ 5 m downstream of the target centre. The maximum allowed misalignment was ~ 0.3 mrad.

The fields of the filter elements were found maximising the transmission of the pilot beam through the separator, measuring the current in the Faraday cups with slits closed to a few millimetres, in order to ensure transmission along the optical axis. Then voltage was applied to the deflection unit in such a way that the ions were deflected to $\theta_{\max}$. The focusing element fields were varied in order to have 100% trasmission of the current to FC4. The deflection unit was then rotated around the beam axis and if full transmission was not achieved for any ϕ angle fields were again varied. The procedure went on iteratively until full transmission was achieved for any ϕ angle at -40, 0, and +40 mm with respect to target centre. Once the tuning procedure was completed, for selected values of ϕ, the applied voltage was varied beyond $\theta_{\max}$ in order to check for the maximum angle at which the beam was fully transmitted. In figure 2.7 is shown the separator angular acceptance as function of the angles θ and φ at various positions, as measured with $E_{\text{lab}}(^7\text{Li}) = 933$ keV, corresponding to $E_{\text{cm}} = 700$ keV. The required angular acceptance at this energy is 26 mrad, see figure 2.5, that is not fully satisfied for minor intervals of φ. Once the measured acceptance is folded with the expected recoil angular distribution as function of θ and with the target density profile the predicted loss of recoils is negligible.

For all the other tunings, namely $E_{\text{lab}}(^7\text{Li}) = 1.30, 1.80, 3.33, 4.13$ MeV, measured angular acceptance was found to exceed largely the requirements for inverse kinematics, as shown in figure 2.5.

The energy acceptance required for $^3\text{He}(\alpha,\gamma)^7\text{Be}$ measurement is shown in figure 2.8 in the form $\Delta E/\bar{E}$, equations 1.4 and 1.5. The transmission of recoils with an energy most different from the central energy $\bar{E}$ is mainly determined by the intensities of the sepWF1 fields. The energy acceptance was verified by checking the transmission through the separator, with fields set to the values found in the tuning procedure, for ion beams with the energy corresponding to the maximum and the minimum energy expected for the recoils. For the minimum energy the loss in the target gas was also considered. When the energy acceptance was found to be not fulfilled, the fields of sepWF1 were changed, keeping their ratio constant, in order to achieve 100% transmission, and the angular acceptance was again checked.

The fields for the measurements at energies other than the tuning energies were obtained scaling the experimental fields of the closer tuning, according to

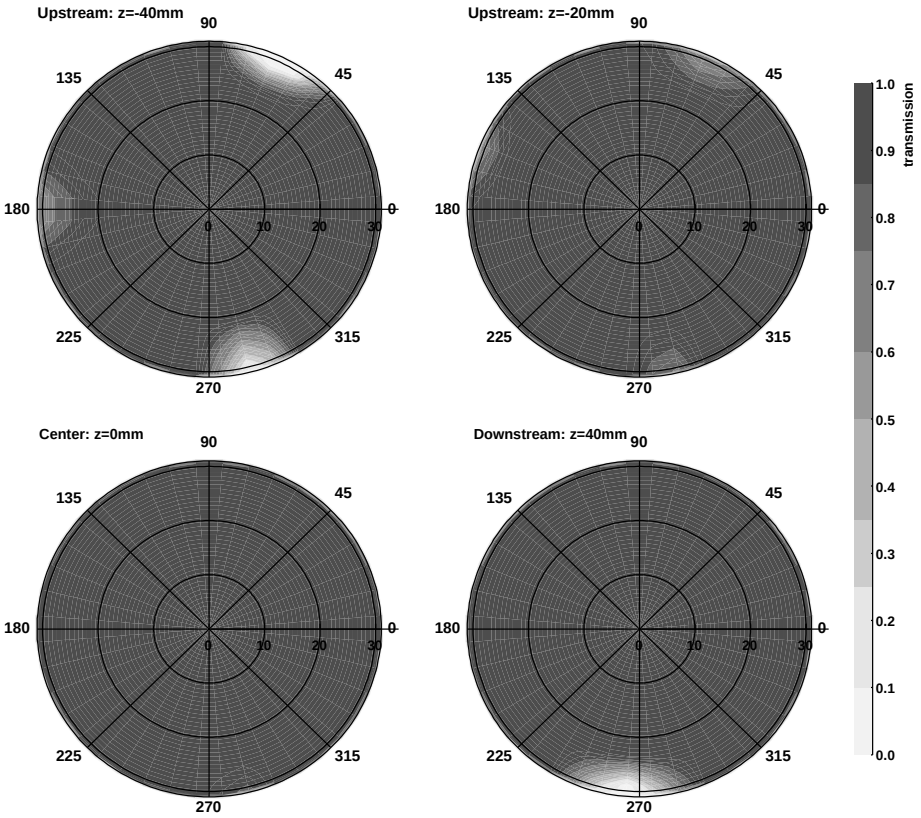

Figure 2.7: Angular acceptance as function of the φ, θ angles at various positions along the gas target.

the momentum of the recoils. Consistent results were obtained in measurements of the recoil yields using fields from two different tunings.

The use of ^{7}Li as pilot beam does not allow to check for angular and energy acceptance for recoils in the q = 4+ charge state.
The separator fields used for detection of recoils in this charge state were obtained by scaling the 3+ fields. As mentioned before higher order effects may lead to not exact scaling of the experimentally determined fields with the charge state. In order to check for recoil losses due to reduced acceptance some tests were performed. Measurements of the recoil yield as function of the most sensitive separator fields were performed at selected energies.
The triplet external lens field strongly influence the trajectories of recoils with a large angular divergence. Therefore, the reaction yields for the 3+ and 4+ charge state were measured as a function of that field at E_{cm} = 1.85 MeV. The results are shown in figure 2.9. The two yields show a similar flat-top behaviour around the

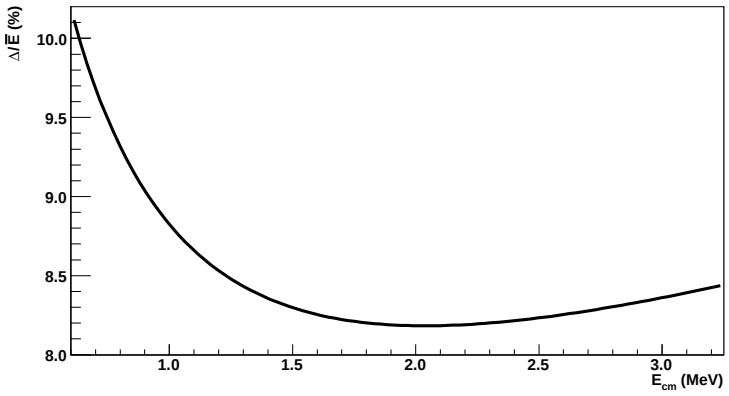

Figure 2.8: Required energy acceptance as a function of the centre of mass energy, see text for details.

field B_0 used for the actual cross section measurements. Analogous results were obtained for a similar measurement performed at $E_{\mathrm{cm}} = 2.3\,\mathrm{MeV}$.
The recoils having an energy most different from $\bar{E}$ are mainly influenced by sepWF1 fields. Measurements with different field intensities, keeping constant $\Delta V/B$, gave consistent results for several values of E_{cm}.
These results support the assumption of full acceptance for the 4+ recoil charge state.

In conclusion the separator has full acceptance for ^{7}Be recoils produced by the $^{3}\mathrm{He}(\alpha,\gamma)^{7}\mathrm{Be}$ reaction initiated in inverse kinematics, independent of the charge state, in a region of ±40 mm from the target centre. Outside this region the trans-

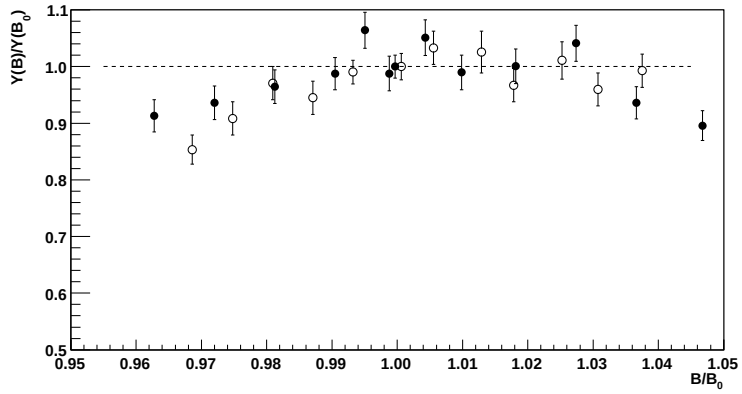

Figure 2.9: Recoil yield for $E_{\mathrm{cm}} = 1.85\,\mathrm{MeV}$ as function of the triplet external lens field B for $q = 3+$ (bullets) and $q = 4+$ (open circles) charge states, with B_0 being the field used for the actual measurement.

mission is somewhat more uncertain. The effect on the total transmission T depends on the density profile of the target gas. This will be further discussed in section 2.5.2.

2.4 Ion identification

As mentioned in section 2.2 the separator's primary beam suppression for some charge states and energy ranges was not sufficient to allow measurements without particle identification. Thus a determination of mass A and nuclear charge Z of the detected ions is necessary. For this purpose a widely used technique in nuclear physics is the ΔE-E telescope. With ERNA two telescopes were used, the first was an Ionisation chamber with fractioned anode (ICT), and the other was an ionisation chamber in conjunction with a large area segmented silicon detector (GST). The energy loss of the recoils in the entrance window of the telescope is a large fraction of the total energy, especially for low energy ions. This is a disadvantage of these detectors, and, together with the intrinsic discrimination limits of ΔE-E telescopes, sets a lower limit on the energy for the ions to be identified. For ^{3}He$(\alpha,\gamma)^7$Be this limit is at $E_{\rm cm} \sim 1.1$ MeV. To perform measurements at lower energies a Time of Flight-Energy detection system (ToF–E) was developed.

All three detectors are described in the following subsections.

2.4.1 The ΔE-E telescopes

The telescope, either the ICT or the GST, was enclosed in a cylindrical chamber filled with isobutane (C_4H_{10}) at a pressure of 4 to 9 mbar, depending on the energy of the ions to be detected. The gas was continuously refreshed (about one chamber volume per hour) using an automatic control system, which also kept the pressure constant within 0.6%. The ions enter the chamber through a window (0.8 μm thick polypropylene foil or 1.5 μm mylar, 40 mm diameter).

Gaseous detectors working in proportional regime have a typical charge collection time of the order of μs. Even when operated with moderately high rates *pile-up* of the events is likely to occur, i.e. two different ions entering the chamber within an interval of a μs are detected as a single event with a larger signal. Pile-up was the main source of background-like events in the measurements of ^{3}He$(\alpha,\gamma)^7$Be, see section 3.1. To discriminate such events a pile-up rejection tag was generated using a Parallel Grid Avalanche Counter (PGAC). This detector, installed in the same volume of the telescope, operates in the discharge regime and produces a fast signal when an ion enters the chamber, its time resolution is 2.5 ns [DL03]. The cathode of the PGAC was an aluminium layer deposited on the telescope entrance window. The anode was a fine wire mesh ($\sim$ 1 mm spacing), and a second mesh

was used to prevent electron leakage in the ΔE active volume. The transparency of the grids $t_{\mathrm{PGAC}} = 0.979 \pm 0.005$ was measured with an α source [DL03]. At a distance of ~ 8 mm after the window the ions enter the active volume of the ΔE.

The ICT is an ionisation chamber of a total length of 80 cm, with fractioned anode to collect separately the charge from the first 8 cm and the rest, to be used as ΔE and E residual respectively. This detector is described in [Rog99a].
The absolute efficiency of the ICT detector is given by the transparency of the PGAC grids

$$\varepsilon_{\mathrm{ICT}} = t_{\mathrm{PGAC}} = 0.979 \pm 0.005 \ .$$

To further improve the pile-up events identification the GST detector was developed. The ΔE of this detector is an ionisation chamber while the E residual was measured by a large area silicon detector. The silicon detector is a 16 strips PIPS detector provided by Canberra (PF-16CT-58*58-300EB, total area $58 \times 58\,\mathrm{mm}^2$). Due to the segmentation of the Si detector particles belonging to a pile-up event

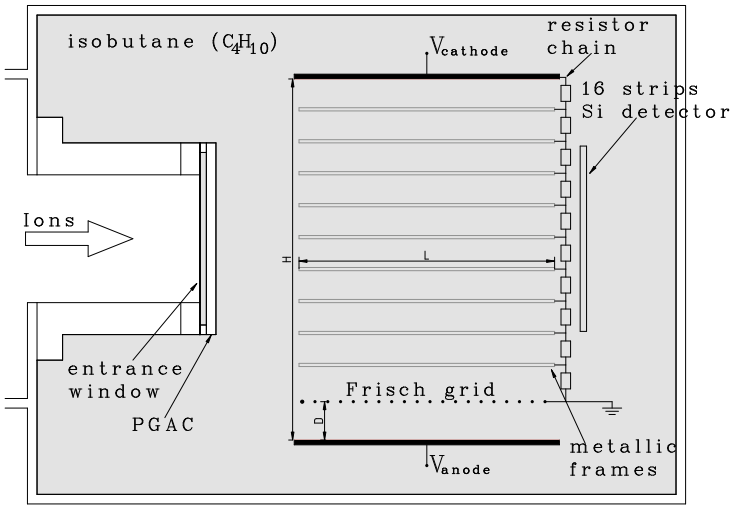

Active volume dimensions (mm)	
width	140
length (L)	80
height (H)	113
Frish grid to anode (D)	13

Figure 2.10: Scheme of the gas silicon telescope (GST), in the table are reported the dimensions of the active volume of the detector.

are unlikely to be detected on the same strip. Thus, in the analysis, events with two or more detected particles were identified as pile-up events. The segmentation also provided useful informations on the distribution of the recoils in the horizontal plane (see section 3.1).
A scheme of the GST is shown in figure 2.10. The design of the ΔE section closely followed the design of the ICT. The Frish grid, consisting of $25\,\mu$m thick gold-tungsten wires at a distance of ~ 1 mm, was kept at ground potential. The

electric field in the active volume is produced by a voltage of 350 V applied to the cathode. In order to achieve a nearly homogeneous field over the entire active volume, 9 metallic frames, each 1 mm thick, were used as a voltage divider (50 MΩ resistors). The frames are continued with 25 μm thick wires over the apertures that allow the ions to enter the active volume of the ΔE and leave toward the Si detector. The electric field between the anode and the Frish grid is obtained by a 300 V voltage applied to the anode.

The silicon detector conductive entrance window has a thickness of 50 nm Si equivalent. The detector is segmented by silicon dioxide layers $\sim$ 50 μm wide, 150 μm thick, see figure 2.11.1. An additional 65 μm wide, 1.5 μm thick layer, *contact area*, runs along the perimeter of the strip [PC06]. The signal amplification, shaping, discrimination, and timing is done via a dedicated electronic modules (Mesytec MPR-16 and SPR16).

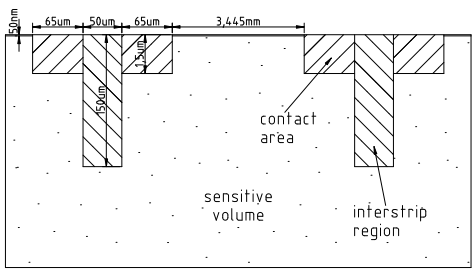

2.11.1:

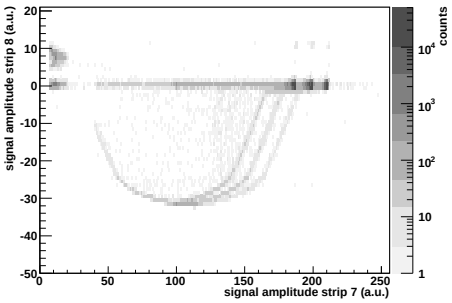

2.11.2:

Figure 2.11: Left: schematic section view of the Si detector, not in scale. Right: triple α source coincidence spectra of two adjacent strips, see text for details.

If a particle hits the detector on the contact area the measured particle energy is reduced by the energy lost in the contact layer, and a negative signal proportional to the loss is induced in the next strip. This feature is illustrated in figure 2.11.2, where a measured two dimensional spectra of a triple α-source (Cm, Am, Pu) is shown. The abscissa is proportional to the charge collected in one of the strips, in this case number 7, and the ordinate is proportional to the charge collected in the next strip, number 8, the shades of grey indicates the intensity. The largest amount of the events were detected in the three peaks corresponding to their full energy loss in strip 7. Some events instead released a large fraction of their energy in strip 7, but also a negative charge is collected in strip 8 with a clear correlation with the signals of strip 7, appearing as the diagonal stripes in figure 2.11.2. The read out electronics is not meant to be used with negative signals, this explains why the correlation is distorted at large negative signals.
This feature of the detector determines the appearance of replicas of the main

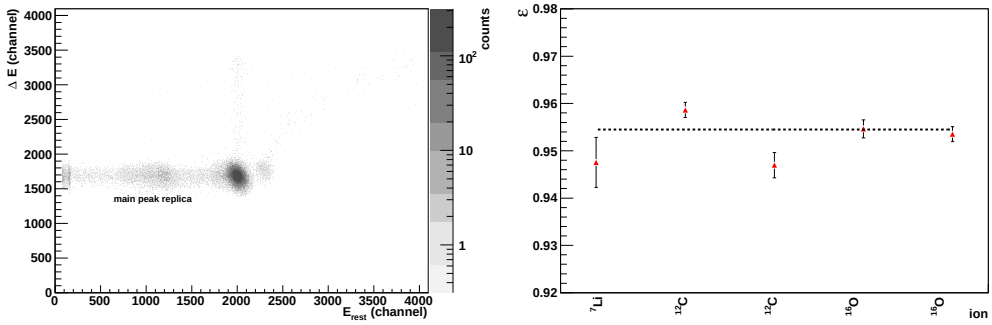

2.12.1: **2.12.2:**

Figure 2.12: Left: GST bi-dimensional ΔE-E_{rest} spectrum of ^{16}O ions $E = 7.0$ MeV. Right: measured absolute efficiency of the Si detector, dotted line indicates the weighted average.

peaks in the experimental spectra, see e.g. figure 2.12.1. The ADC used for the data acquisition (Silena 9418/6-V 32) converts only positive signals, therefore the negative induced signal could not be used to tag those events.

The complete characterisation of the GST detector required its absolute efficiency to be measured. Since the detection efficiency for the ionisation chamber part is 100%, the quantity to be determined was the absolute efficiency of the silicon detector $\varepsilon_{\mathrm{Si}}$. For this purpose low intensity beams, from $\sim$ 50 to $\sim$ 1500 particles/s, of ^{7}Li, ^{12}C, and ^{16}O were guided into the telescope. The ratio of coincidence events in the silicon detector and the ΔE with respect to the total number of events detected by ΔE was determined. The results are shown in figure 2.12.2. The replica events of the main peak (figure 2.12.1) were not accounted for the determination of the absolute efficiency of the detector, that results to be

$$\varepsilon_{\mathrm{Si}} = 0.954 \pm 0.003 \ .$$

The absolute efficiency of the GST telescope is then

$$\varepsilon_{\mathrm{GST}} = t_{\mathrm{PGAC}} \cdot \varepsilon_{\mathrm{Si}} = 0.934 \pm 0.006 \ .$$

2.4.2 ToF–E detection system

For measurements below $E_{\mathrm{cm}} = 1.1$ MeV a new detector had to be developed. The requirements to be fulfilled were: compact dimensions, $\sim$ 1 m; large active area, to fit the recoil beam dimension of $\phi \sim 30$ mm as expected from optical calculations; high transparency; very small additional energy and angular spread introduced on the recoils.
Such characteristics can be met by a Time of Flight-Energy detection system. The

mass is identified by the correlation of the particle energy and the time needed to travel between two well defined positions in the separator line. The first timing signal, corresponding to the crossing of the first line was provided by the Time Zero Detector (TZD), a Microchannel Plate (MCP) mounted in electrostatic mirror configuration [Bus80]. The energy measurement and the second timing signal were provided by a large area Si detector, identical to the one described in the previous section. This ToF–*E* detection system configuration does not allow to determine the nuclear charge *Z* of the ions. But since no recoil like contaminations were expected, see section 2.5.3, the mass identification was sufficient and such a detection system was suitable for low energy measurements of ^{3}He$(\alpha,\gamma)^7$Be with ERNA.

The working principle of the ToF–*E* detection system is shown in figure 2.13. The MCP essentially is an electron multiplier, the one used was provided by Burle

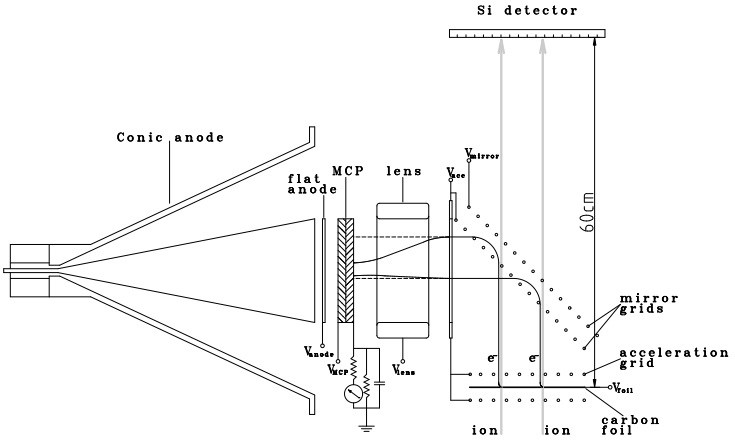

Applied voltages (kV)	
V_{foil}	-1.1
V_{acc}	0
V_{mirror}	-1.7
V_{MCP}	2.0
V_{anode}	2.5
V_{lens}	-0.9

Figure 2.13: Working principle of the electrostatic mirror, note that drawing is not in scale.

(model 3040-60:1), 2 stages in chevron mounting, with a nominal gain of $\sim 2\times10^7$ and active area of 40 mm in diameter. The multiplied electrons were collected on the flat anode, a metal disc 40 mm diameter, 3 mm from the back side of the MCP. The actual signal was obtained by capacitive coupling of a conical anode to the MCP flat anode at 2 mm distance. The conical anode provides a better matching of the detector to the 50 Ω impedance of the read-out electronics (Ortec FTA 420 Fast Amp), in order to avoid reflections and degrading of the signal, a key requirement for sub-nanosecond timing resolution. The capacitive coupling gives also the possibility to apply a bias to the flat anode, that in turn corresponds to a flexible choice of the MCP front face bias.

In the electrostatic mirror configuration the active surface of the MCP is placed parallel to the beam axis. The passage of an ion through the TZD is indicated by

the detection of electrons stripped from a thin carbon foil placed orthogonal to the beam axis. The number of stripped electrons depends on the stopping power, that is Z and the E, of the ion to be detected, and, for very thin foils ($< 10\,\mu g/cm^2$), on the foil thickness [Fri86]. The foil is mounted on a metallic frame kept at voltage $V_{foil} = -1.1\,kV$. The acceleration grid, a fine wire mesh parallel to the foil at 3 mm distance, was kept at $V_{acc} = 0\,V$. Another identical mesh at the same voltage, placed in a symmetric position with respect to the foil, prevents its deformation due to electrostatic forces. Thus the electrons, stripped from the foil at energies of a few tens of eV, are accelerated in beam direction to $\sim 1.1\,keV$. This energy was chosen to reach the maximum detection efficiency of the MCP [Fra83]. Once accelerated the electrons will have almost the same velocity and, in first approximation, a direction parallel to the beam axis. The electrons are bent toward the MCP by the *electrostatic mirror*. The mirror consists of two fine wire meshes at a relative distance $d = 6\,mm$ with the wires parallel to the MCP. The planes of the mirror grids are at 45° with respect to the beam axis. The first mesh, the *internal* grid, is kept at the same potential of the acceleration grid V_{acc}, as well as the front face of the MCP. The second mirror grid, the *external* grid, is kept at $V_{mirror} = -1.7\,kV$. With this choice of the voltages the electrons do not experience any forces in the region defined by front face of the MCP, the acceleration and internal grids, and follow straight trajectories. The parabola trajectories between the mirror grids are equal for all the electrons provided their direction is parallel to the beam axis. Thus the electron trajectories are isochronous regardless of the emission position on the foil, a feature that improves the time resolution. The voltage applied to the back side of the MCP was $V_{MCP} = 2\,kV$, and to the flat anode was $V_{anode} = 2.5\,kV$.

The actual values of the voltages were chosen by optimising the detection of α particles from a source and at the same time minimising the *dark counts*, detection of electrons not emitted from the carbon foil [DC06].

The TZD detection efficiency is strictly related to the mean number of electrons stripped from the carbon foil and their transport to the front face of the MCP. Nevertheless, due to the relatively low energy of the ions, the additional angular straggling given by the interaction with the foil atoms is not negligible. This has a direct consequence on the recoil beam diameter at detector position. A larger angle implies, for the same flight path length, a larger detector size. To achieve a ToF difference for recoils and leaky particles in the order of a few ns the flight path length had to be of about 60 cm or more. I performed MC calculation of angular straggling of the recoils in the C foil, in connection with optical calculations, to determine the optimal foil thickness as a function of the flight path length. It turned out that a foil thicker than $10\,\mu g/cm^2$ would lead to incomplete collection of recoils at the Si detector. Therefore to grant a large safety margin under this respect, a Laser Ablation Deposition (LPA) [MK99] carbon foil of $4\,\mu g/cm^2$ was

used. The mounting of such a thin foil with a diameter of 45 mm is technically very challenging. Mechanical stability of the foil in the mounting procedure was improved with the aid of formvar, a polymer, subsequently removed before use by rastering a low intensity C beam over the foil surface for several hours.

In the energy range of the experiment where the ToF–E detection system was used (recoils energy 130 to 230 keV/amu), the mean number of electrons stripped from the foil is expected to be ~ 5.

The characterisation of the detector included the determination of the efficiency as a function of the distance from the beam axis and the energy of the ^{7}Be recoils.

A measurement of the efficiency of the TZD as a function of the position on the carbon foil was performed using the slits installed directly before the TZD chamber and a 1 MeV $^7Li^+$ beam with low intensity, ~ 100 ions s^{-1}. The stopping power of Lithium at this energy is the same as for ^{7}Be at 750 keV [Bie03], corresponding to $E_{cm} = 600$ keV. Thus the measured efficiency at that energy represents a lower limit for the overall detection efficiency of the ToF–E detection system, since the stopping power, and therefore the efficiency, increases with increasing recoil energy. The slits were set in order to define a 2×2 mm^2 square centred at the position (x, y). The efficiency $\varepsilon(x, y)$ was obtained as the ratio of the particles detected in the 16 strips silicon detector to the coincidences with the TZD. The value, and therefore the error, was calculated as the weighted average of the values for the single strips having more than hundred counts.

A first version of the TZD was not equipped with the focusing lens, shown in figure 2.13. The measured $\varepsilon(x, y)$, shown in figure 2.14.1, was not satisfying. A significant drop in the detection efficiency outside a diameter of ~ 10 mm around the beam axis was observed. This would have made the use of the detector unpractical, because of the unknown recoil distribution at the foil position. This effect was possibly caused by electrons emitted from the foil but not collected on the active surface of the MCP. The addition of the einzel lens, that focuses the electrons toward the MCP centre, significantly improved the performance of the detector, as can be seen in figure 2.14.2. The lens modifies the electron trajectories and makes them not isochronous, thus introducing a worsening of the time resolution. The detection efficiency obtained is almost uniform within a diameter of 30 mm around the beam axis, a significant drop is still present in the upper half at larger distance. The asymmetry has been attributed to a vertical misalignment of the MCP with respect to the mirror. During the tuning procedure it was verified that about 98% of the pilot beam ions were within a $\phi = 30$ mm diameter around the beam axis. The detection efficiency of the MCP ε_{MCP} is taken as the average value over that area

$$\varepsilon_{MCP} = 0.98 \pm 0.01 \ .$$

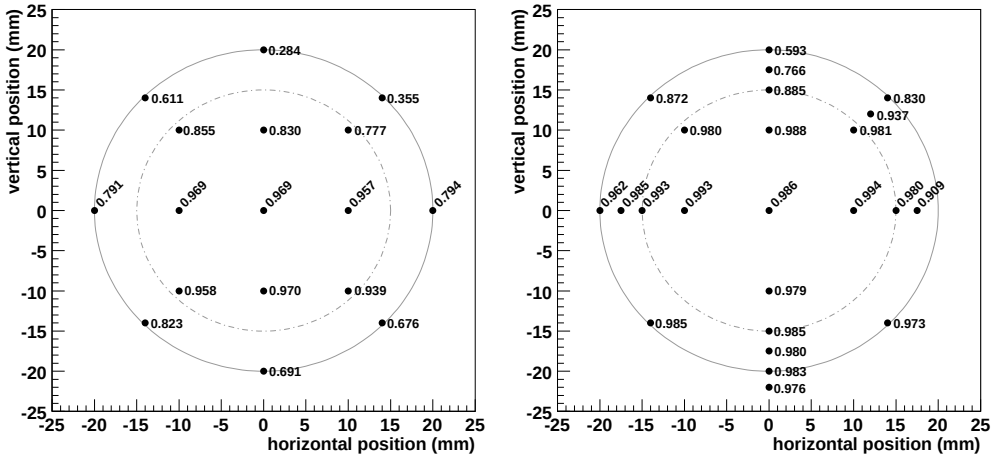

2.14.1: Efficiency as measured before the installation of the electron focusing lens.

2.14.2: Efficiency as measured using the electron focusing lens.

Figure 2.14: Results of the measurement of the TZD efficiency as function of the position.

As regards the dependence of $\varepsilon_{\mathrm{MCP}}$ on the energy of the recoils, in the energy range where the ToF–E detection system was used the variation of the ^{7}Be stopping power has no significant influence on the mean number of electrons stripped. Thus $\varepsilon_{\mathrm{MCP}}$ was assumed constant.
The transparency t_{mirror} of the TZD meshes was measured by detecting ^{4}He ions in the Si detector with and without the mirror on the beam axis, it resulted to be

$$t_{\mathrm{mirror}} = 0.954 \pm 0.012 \ .$$

Finally the total efficiency of the whole ToF–E detection system is the product of the mirror transparency, the detection efficiency of the MCP $\varepsilon_{\mathrm{MCP}}$ and the efficiency of the 16 strips Si detector $\varepsilon_{\mathrm{Si}}$

$$\varepsilon_{\mathrm{ToF}\text{–}E} = t_{\mathrm{mirror}}\varepsilon_{\mathrm{MCP}}\varepsilon_{\mathrm{Si}} = 0.909 \pm 0.015 \ .$$

2.5 The ^{3}He recirculating gas target

As shown in section 2.3 the needed angular acceptance is fulfilled by the separator only if the reaction is initiated in inverse kinematics. This meant that the windowless differentially pumped gas target, as it was used for the measurement

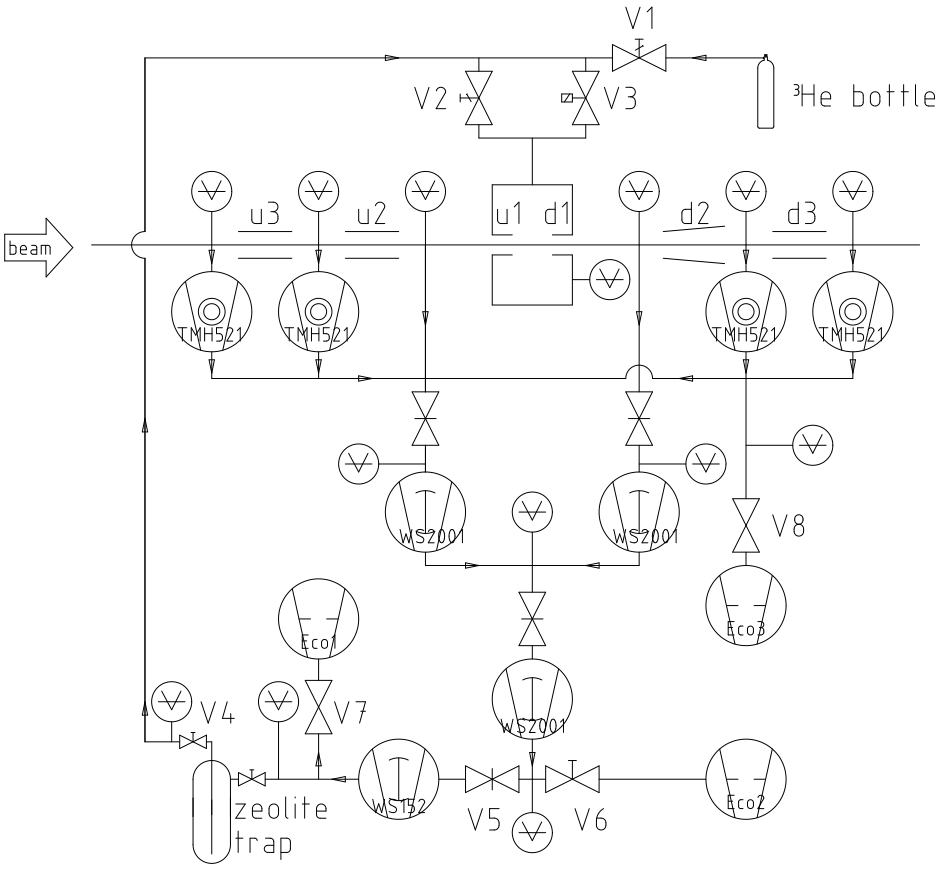

Figure 2.15: Scheme of the recirculating ^{3}He gas target.

of $^{12}C(\alpha,\gamma)^{16}O$ [Sch07], had to be accommodated to the use of ^{3}He gas. Although in principle the target could have been operated with ^{3}He as it was, the relatively high gas consumption, $\sim 8\,l$/min PST, made its use unpracticable in view of the high cost of ^{3}He. Therefore the pumping scheme of the gas target was modified, as shown in figure 2.15, in order to allow recirculation of the gas. The piston pumps backing the roots blowers were replaced with a double stage roots blower pump (Leybold WS152), whose exhaust line was connected to a zeolite trap cooled to liquid nitrogen temperature. The zeolite trap provided the necessary cleaning of the gas from oil and residual gases, an issue further discussed in section 2.5.3. To minimize gas loss the back pumping of the turbo pumps of the second and third pumping stages was provided by the first upstream roots blower.

The target chamber, shown in figure 2.16, was not modified with respect to the ^{4}He target. The length of the central gas cell was 40 mm, connected to the first outer pumping stages by the apertures u1 and d1. The upstream apertures u1, u2,

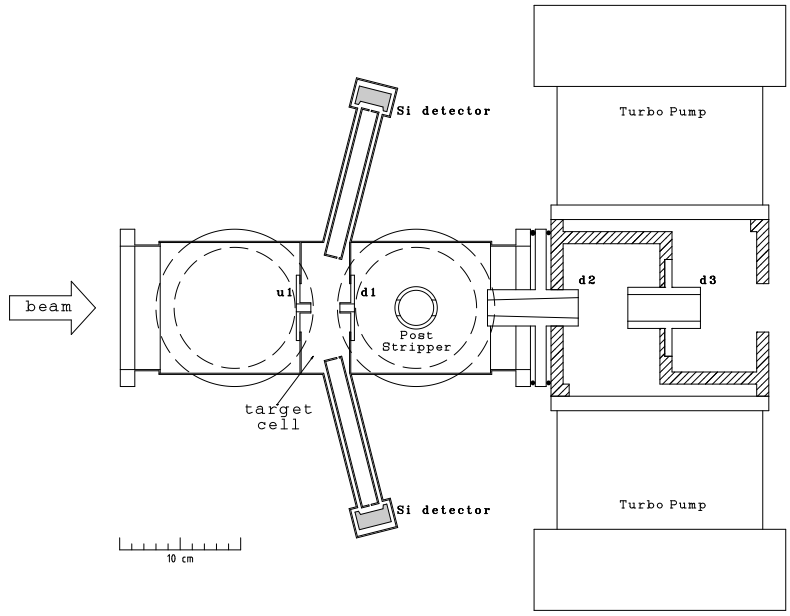

Figure 2.16: Detail of the gas target chamber. The 2nd and 3rd upstream pumping stages and the apertures u2 and u3 are not shown.

u3 were cylindrical with diameter of 6, 10, and 14 mm and a length of 10, 75, and 30 mm, respectively. The downstream apertures d1, d2, d3 had the same respective length. Apertures d1 and d2 were conically shaped with an angle of 30 mrad, with entrance diameter of 5.4, 12.3, and 22 mm for d1, d2, and d3, respectively. These dimensions allow particles to enter the quadrupole triplet with angular divergence up to $\theta = 30$ mrad produced within a circle of 3 mm diameter around the beam axis.

Two collimated silicon detectors, facing the centre of the gas cell at 75° with respect to the beam axis, were used to monitor the elastic scattering rate. A pipe was present in the first downstream pumping stage, that could be used for the injection of post-stripping gas, but was not needed in the case of the ^{3}He$(\alpha,\gamma)^7$Be measurements.

The system was initially evacuated by the pumps Eco1 and Eco3. ^{3}He was injected from the reservoir bottle into the system via the V1 valve, about 0.5 l PST were needed to reach working conditions. The pressure of the central gas cell was chosen to be 2 mbar, measured with 2% accuracy by an absolute capacitance gauge meter (Pfeiffer CMR261). This value of the pressure granted a large enough total thickness but takes into account the issues related to angular straggling, see section 2.3. It was also observed that the amount of target gas lost in the beam line was increasing with the central cell pressure. The gas flow into the inner

target chamber was controlled by the aperture of the valve V2. The pressure of the gas in the central cell was continuously monitored by an automatic regulation system (Pfeiffer RVC300). This device provided the necessary feedback to the additional electromechanical valve V3 (Pfeiffer EVR116) to keep the pressure constant, within 1%, against gas loss in the beam line. The loss of gas was in the order of 10%/h of the initial gas volume. After few hours of operation fresh gas was injected through the valve V1 to restore initial conditions.

It was possible to operate the gas target also with ^{4}He, without removing all the ^{3}He gas from the system. In fact operating valves V4 and V5 the ^{3}He could be kept in the volume of the WS152 pump and the zeolite trap. The ^{4}He, not recirculated, was expelled from the system through the Eco2 pump. This feature of the gas target allowed to perform background measurements with the same conditions of beam focusing, see section 3.1. Before going back to recirculation mode, and use again ^{3}He, the gas target was operated with Ar gas for some minutes in order to minimise target contamination from ^{4}He residual gas. The effectiveness of this procedure is further discussed in section 2.5.3.

2.5.1 Target thickness

The determination of the total target thickness N_t is a crucial point. The uncertainty on this quantity fully dominates the total systematic uncertainty of the measurements.

The target areal density could be estimated via energy loss measurements using the separator's 60° dipole magnet. In fact ions of energy E traversing a thin target loose an amount of energy $\Delta E = S(E) \cdot N_t$, where $S(E)$ is the corresponding stopping power. The measurement procedure made use of an ion beam of energy E_0, that was focused on the target without gas, and then guided to FC4 at the end of the separator. In such condition the beam exits the dipole on the optical axis, and maximise the current in FC4, if the dipole measured B field satisfies the relation

$$B_0 = \kappa \frac{\sqrt{2mE_0}}{q} \quad , \tag{2.1}$$

where κ depends from the curvature radius of the magnet, the calibration of the probe, etc. When gas is inserted in the target cell, ions after passing the cell will have energy $E = E_0 - \Delta E$, and will be no longer properly transmitted through the dipole. The maximum of the current in FC4 is then achieved with a new field value $B = B_0 - \Delta B$. ΔB is connected to ΔE by the relation

$$\Delta E = E_0 \left[1 - \left(\frac{E - \Delta E}{E} \right)^2 \right] \simeq 2E_0 \frac{\Delta B}{B_0} \quad ,$$

and, therefore, it is possible to obtain the gas thickness as

$$N_t = \frac{2E_0}{S(E)}\frac{\Delta B}{B_0} \quad .$$

A disadvantage of this method is that often experimental data for the stopping power are not available for the ion/energy/target combination used for the measurements. Thus the stopping power has to be evaluated on the basis of standard compilations like SRIM [Bie03]. On such values a conservative $\sim$ 10% error is quoted. In order to achieve better precision on the total target thickness, the strategy has been to measure the ratio R of the ^{3}He target thickness $N_t(^3\mathrm{He})$ with respect to the thickness $N_t(^4\mathrm{He})$ of the ^{4}He target. Then

$$R = \frac{N_t(^3\mathrm{He})}{N_t(^4\mathrm{He})} = \frac{\Delta B(^3\mathrm{He})}{B_0(^3\mathrm{He})}\frac{B_0(^4\mathrm{He})}{\Delta B(^4\mathrm{He})} \quad .$$

The stopping power $S(E)$ can be assumed to be the same for ^{3}He and ^{4}He since in the energy regime exploited it is mainly determined by atomic ionisation and nuclear effects are negligible. An example of the determination of ΔB is shown in figure 2.17, where the current measured in FC4 is shown as function of the dipole magnet field B. Measurements have been performed with several ion beams, namely ^{7}Li, ^{12}C, ^{14}N, and ^{16}O. The results are summarised in table 2.1. The estimate for the ratio R is

$$R = 0.459 \pm 0.005 \quad .$$

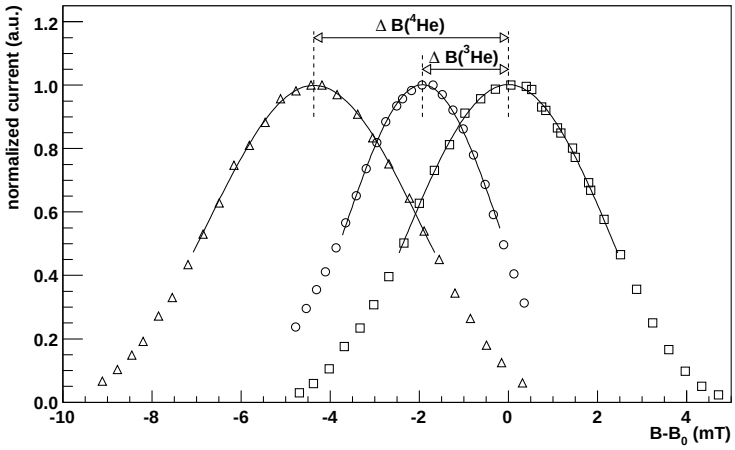

Figure 2.17: Typical behaviour of energy loss measurements. The FC4 current, normalised to the maximum, is shown as function of the dipole magnetic field B. □ indicate a measurement without gas, ○ with 2 mbar ^{3}He, △ with 4 mbar ^{4}He.

ion	E(MeV)	S (keV/(10^{17}/cm^2))	^{3}He target p = 2 mbar	^{4}He target p = 4 mbar			$R \times 10^{-2}$
			$\frac{\Delta B}{B} \times 10^3$	$\frac{\Delta B}{B} \times 10^3$	ΔE (keV)	N_t(10^{17} cm^{-2})	
$^7Li^+$	1.68	2.829	1.71 ± 0.02	3.97 ± 0.02	13.3 ± 0.4	4.7 ± 0.4	45.0 ± 1.0
$^{12}C^{2+}$	2.00	5.839	3.21 ± 0.03	7.17 ± 0.03	28.6 ± 0.8	4.9 ± 0.4	44.8 ± 1.2
$^{12}C^{2+}$	4.50	6.457	1.46 ± 0.02	3.17 ± 0.03	28.7 ± 0.9	4.5 ± 0.4	45.8 ± 1.9
$^{14}N^{2+}$	2.00	6.497	3.49 ± 0.02	7.50 ± 0.02	29.9 ± 0.9	4.4 ± 0.4	46.5 ± 0.6
$^{16}O^{3+}$	4.50	8.962	2.10 ± 0.02	4.54 ± 0.02	40.8 ± 1.2	4.6 ± 0.4	46 ± 2

Table 2.1: Results of the energy loss measurements for the determination of the ^{3}He total target thickness. The absolute ^{4}He thicknesses measured in this work are also reported.

The ^{4}He target thickness $N_t(^4\text{He}) = (4.37 \pm 0.12) \times 10^{17}$ atoms/cm^2 is obtained from the values reported in [Sch07] combined with the values measured in this work. The resulting thickness for the ^{3}He target is

$$N_t(^3\text{He}) = R \cdot N_t(^4\text{He}) = (2.00 \pm 0.08) \times 10^{17} \text{ atoms/cm}^2 \quad .$$

2.5.2 Density profile

I mentioned already in section 2.3 that the transmission of the recoils decreases as the distance from the target centre along the beam axis exceed ~ 40 mm. Therefore it was necessary to check that the target gas was confined mainly in the region where full acceptance was verified.
The density of the gas as a function of the distance from the target centre, the density profile, can be obtained by measuring the γ-ray yield of a nuclear reaction from small areas of the target. If the reaction yield is almost constant over the whole target thickness the yield from a small portion is proportional to the density at that point. This measurent was performed using a well shielded high purity germanium detector (HPGe) of 110% efficiency[1], as shown in figure 2.18. The γ-rays from the target were collimated through a slit of 2 mm width in the 10 cm thick lead shielding, limiting the effective target length seen by the detecotor to ~ 4 mm. The effective length was obtained by a GEANT4 [Ago03] simulation of

[1] Efficiency of HPGe is expressed with respect to the efficiency of a 3 × 3 inch NaI detector.

the setup, that gives the expected response of the detector to an isotropic source as function of the source position with respect to the slit centre. The results of the simulation are shown in right panel of figure 2.18.

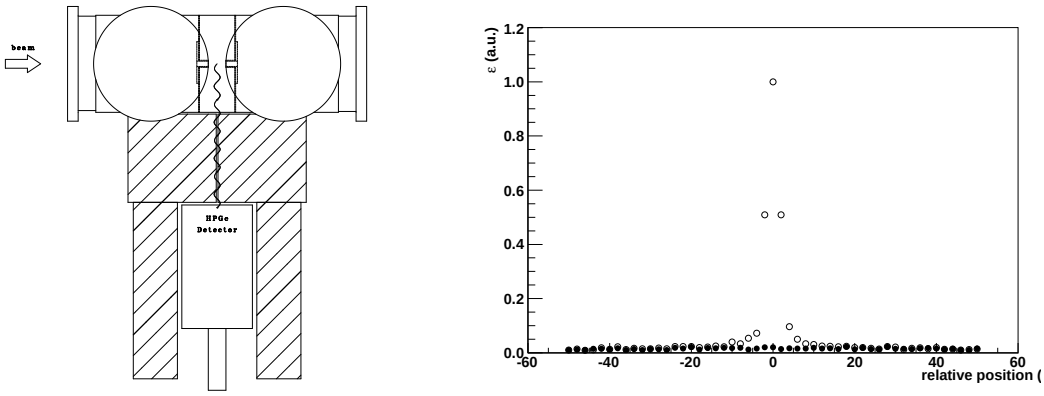

Figure 2.18: Left: scheme of the setup used for the ^{3}He gas target density profile measurement. Right: the simulated response of the detector, where the open circles indicates the case with the 2 mm wide slit, while the filled circles demonstrate the case with a closed slit.

Direct capture reactions or resonant reactions having width larger than the target thickness are best candidates to be used for the measurement. Unfortunately light elements (^{3}He, γ) reactions having high yield have also low threshold for neutron production, e.g. the ^{7}Li + ^{3}He reaction has both the γ-ray and neutron channels open. The expected neutron fluxes were larger than the maximum allowed for the laboratory. Therefore I chose to use the ^{3}He(^{16}O, $p\gamma$)^{18}F reaction that, using ^{16}O as projectile, has at $E_{\mathrm{lab}} = 15$ MeV a cross section of ~ 50 mb [Hah66]. The yield was high enough to have a reasonable measurement time, from 20 minutes to 2 hours for one data-point. The cross section does not show resonance structures, and could be assumed to be constant over the target thickness (3 keV in the centre of mass).

The reaction yield was measured at different positions along the target by moving together detector and shielding parallel to the beam axis. Due to the fact that not all of the γ-rays were absorbed by the lead shield, also γ-rays emitted in other parts of the target may contribute to the spectrum, *off-slit* yield. To evaluate this contribution also measurements with the detector completely shielded were performed, to be subtracted from the measurement runs. Indeed in this way also contributions from the observed area are subtracted, for this reason a correction of 2%, as estimated from the simulation, was applied.

Since the off-slit contributions become larger with increasing γ-ray energy, among the several transitions of the ^{18}F, only the one with the lowest energy, namely the

627 keV, was used to work out the density profile. Results of the measurements are shown in figure 2.19.

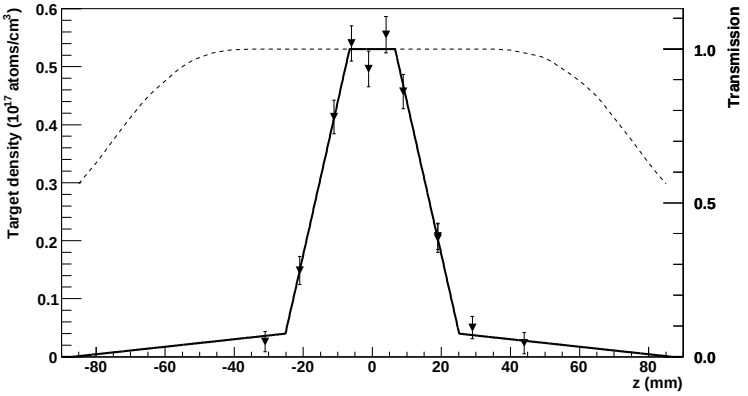

Figure 2.19: Density profile of the ^{3}He gas target as a function of the distance z from target centre. The dashed line represents the expected transmission of ^{7}Be recoils.

The curve through the experimental points $N_t(z)$ is a symmetric function given by a constant plus two linear parts. It is normalized to the density at $z = 0$ known by pressure measurement. Due to the few number of experimental points the uncertainty on the total thickness that may be derived would be much higher than what is obtained via energy loss measurements discussed before. Nevertheless the ratio of the amount of gas lying in the flanges with respect to the central region can be determined. The amount of gas outside ±40 mm is ∼ 4%. The measured pressure in the first pumping stages supports this estimate.

In figure 2.19 the acceptance for ^{7}Be recoils as a function of the reaction coordinate is depicted (dashed line) based on experimental values obtained during the separator tuning and optical calculations (section 2.3). Clearly, the transmission of the recoils produced at a distance larger than 40 mm from the gas target centre is less than 100%: its actual value is rather uncertain, depending on the details of the phase space volume occupied by the recoils and the corresponding acceptance of the separator. Thus the folding of $N_t(z)$ with the separator acceptance leads to an energy dependent transmission T to the end detector ranging from 98 ± 2% at $E_{\mathrm{cm}} \leq 1$ MeV to 99 ± 1% at $E_{\mathrm{cm}} > 1$ MeV.

2.5.3 Target and beam contaminations

The contaminations of other ion species in the projectile beam are usually negligible for standard accelerator physics experiments. Nevertheless in the case of

measurements with a recoil separator those contaminations may be a large problem. In fact since the analysing magnet is a rigidity filter all the ions leaving the filter on axis have the same p/q. Thus isobars of the recoils present as contaminants, here ^{7}Li, with the same charge state selected by the separator, would have the same velocity of the recoils. Such isobars would be transmitted trough the separator and could not be distinguished from reaction products. Therefore the beam purity required for measurements with a separator is extremely high, for this work the ^{7}Li contaminations had to be kept far below 1×10^{-15}, this level corresponds to a 1% background for $\sigma = 1\mu$b.
The presence of ^{6,7}Li as beam contaminants was expected since Li was used in the exchange channel of the duoplasmatron ion source. The reactions producing ^{7}Be, such as ^{6}Li(^{3}He, d) and ^{7}Li(^{3}He, t) have cross section 10^3 to 10^5 times larger than ^{3}He$(\alpha, \gamma)^7$Be. These reactions may have led to parasitic production of recoils even with small contaminations.
The high purity level of the impinging beam was granted by two Wien filters in the beam preparation stages, one before and one after the analysing magnet, as shown in figure 2.1. The two Wien filters were set to match the velocity of the ^{4}He ions. Thus the contaminations were kept to a negligible level at all energies. In figure 2.20 are shown two γ-ray spectra from an HPGe detector placed in close

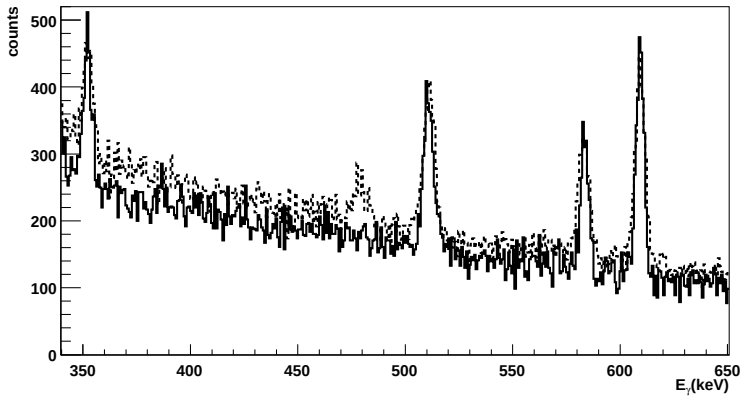

Figure 2.20: HPGe γ-ray spectra of measurement without beam purification (dashed) and with beam purification (solid).

geometry to the target chamber. In the spectrum of the measurement without beam purification by the Wien filters a peak at $E_\gamma = 479$ keV is present. This is due to the inelastic scattering of contaminant ^{7}Li on ^{3}He. The peak disappears when the purification Wien filters are used.
Moreover contaminations and parasitic production of ^{7}Be were directly checked by performing background runs at all energies (see section 3.1): no Li contaminations were observed. Furthermore during the measurement campaign the source

was upgraded with a rubidium exchange channel. Measurements at selected energies were repeated. The results were found to be consistent for all the charge states.

The purity of the target gas was checked as well to investigate on induced parasitic production on impurities, i.e. residual gases, pump oil vapours, etc. There was also the need to check that the partial pressures of contaminants, especially residual ^{4}He from the background runs, were negligible with respect to ^{3}He.
Cleaning of gas from impurities heavier than He was obtained with a *zeolite trap* cooled to liquid nitrogen temperature. The purity of the gas and the effectiveness of the cleaning were tested observing the scattering yield of protons in the silicon detectors that face the target cell. In figure 2.21.1 the spectrum of a measurement performed with protons of $E_{\mathrm{lab}} = 3.0\,\mathrm{MeV}$ is shown. Such a measurement has a higher sensitivity due to the lower Z of the projectiles. ^{4}He and ^{40}Ar gases

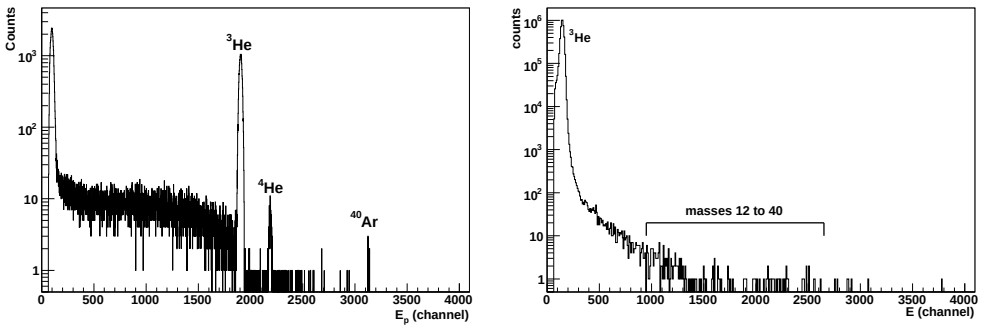

2.21.1: **2.21.2:**

Figure 2.21: Test of target gas purity. Left: elastic scattering of protons $E_{\mathrm{lab}} = 3.0\,\mathrm{MeV}$, the peaks relative to ^{3}He and residual ^{4}He and ^{40}Ar gases are indicated. Right: scattering of ^{4}He at $E_{\mathrm{lab}} = 3.27\,\mathrm{MeV}$, see text for details.

were used as target to identify the corresponding peaks. The spectrum shown was acquired after several cycles of measurement and background runs. The residual ^{4}He contamination present in the ^{3}He target accounts for less than 0.4% of the total thickness.
Another check of the target purity was obtained from the spectra of elastically scattered He at target position, that are used to monitor the incoming current (section 3.1). In figure 2.21.2 the sum of spectra of a measurement at $E_{\mathrm{cm}} = 1.4\,\mathrm{MeV}$, for a total running time of 15 hours, is shown. The main peak is due to ^{3}He, the tail is most likely due to multiple scattered particles. In the region at higher energies where ^{4}He scattered by atoms heavier than the target gas were expected very few counts were collected. In none of the scattering spectra a significant yield from heavy atoms was observed. This demonstrates that contaminants were orders of magnitude lower than the target density.

2.6 γ-rays detector array

A recoil separator offers the opportunity of γ-ray measurements using a coincidence condition, i.e. selecting in the γ-ray spectrum only events that appear within a limited time window with respect to a recoil detection. This allows to have almost background free γ-ray spectra, since the background is given only by random coincidences, a contribution that can be evaluated by coincidences with the leaky beam (section 3.2).

An array of three sodium iodide (NaI) 3×3 inch detectors (Ortec 905-4) was placed in close geometry to the target chamber to detect the γ-rays. The setup is schematically illustrated in figure 2.22. The detectors were facing the chamber

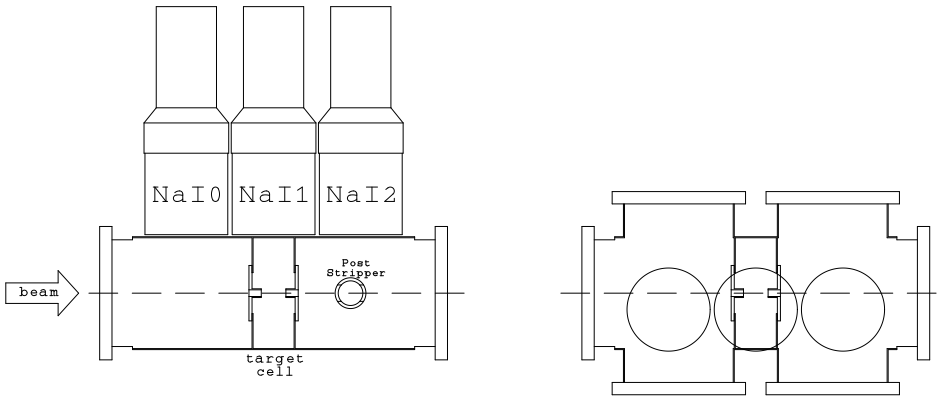

Figure 2.22: Schematic view of the NaI detector array used for γ-ray detection measurements. Left: top view. Right: side view.

wall at 1 mm distance, thus at 57 mm from the beam axis. Due to the presence of the target silicon detector pipe, not shown in the figure, the centre of the detector front face was 18 mm below the beam axis, in order to reach the closest distance to the chamber.

The geometry of the extended gas target and of the chamber determine a non trivial dependence of the efficiency with the energy; the maximum γ-ray energy was about 4.6 MeV. The efficiency[2] of the setup was determined on the basis of a GEANT4 simulation. An adequate validation was done by additional measurements with ^{56}Co sources, a nuclide with a half-life of 77.27 d, emitting several γ-rays with energies ranging from 0.85 to 3.6 MeV. Two sources were produced at the cyclotron of the ATOMKI in Debrecen, Hungary. They were obtained by proton bombardment of natural iron targets, via the reaction $^{56}\mathrm{Fe}(p,n)^{56}\mathrm{Co}$ at

[2]Unless otherwise specified for γ-ray detectors I will use *efficiency* to indicate the full energy peak efficiency.

$E_p = 15.5\,\text{MeV}$. During the activation a $\phi = 3\,\text{mm}$ tantalum mask was placed on top of the targets, thus defining the active spot to the same size, granting an almost point like source.

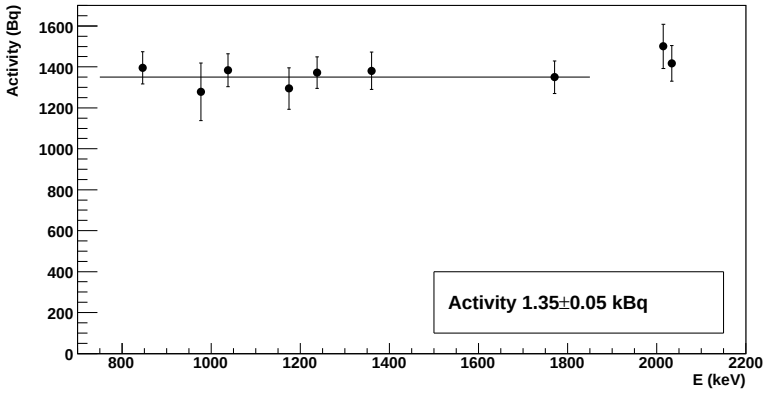

Figure 2.23: Measured activity of the ^{56}Co source A, as obtained from the yields of the different transitions. Solid line represents the average of the values in the energy range where the detector was calibrated.

I calibrated one of the sources, source A, using the HPGe detector of the Environmental Radioactivity Laboratory at CIRCE in Caserta, Italy. The efficiency of this HPGe detector I determined using a multi-isotope source certified to a precision of 3% (2σ confidence level). The activity of the ^{56}Co source A was determined with 4% accuracy, as average of the values obtained from the various γ-rays emitted by the source, figure 2.23. For the measurement the distance between source and detector was fixed at $\sim 120\,\text{mm}$, in order to minimise *summing* effects. Summing appears when a source generates γ-ray cascades. In close geometry the probability of detecting two or more γ-rays belonging to the same cascade can be relevant. In this case the signal produced by the detector is proportional to the sum of all of the γ-rays detected: a cascade appears as a single transition. This effect is called a true coincidence summing (TCS) and is strongly affected by the angular correlation between the cascade γ-rays and the source-to-detector distance. The effect is purely geometrical and does not depend on the source intensity. This aspect has to be carefully taken into account when the source is used for absolute efficiency determinations.

The second ^{56}Co source, source B, was calibrated with respect to source A, by measurements at several distances with a single NaI detector. The accuracy achieved for the activity was 5%. Source B was used to investigate the influence of the summing in the ^{56}Co γ-ray detection. In particular it was used to analyze the

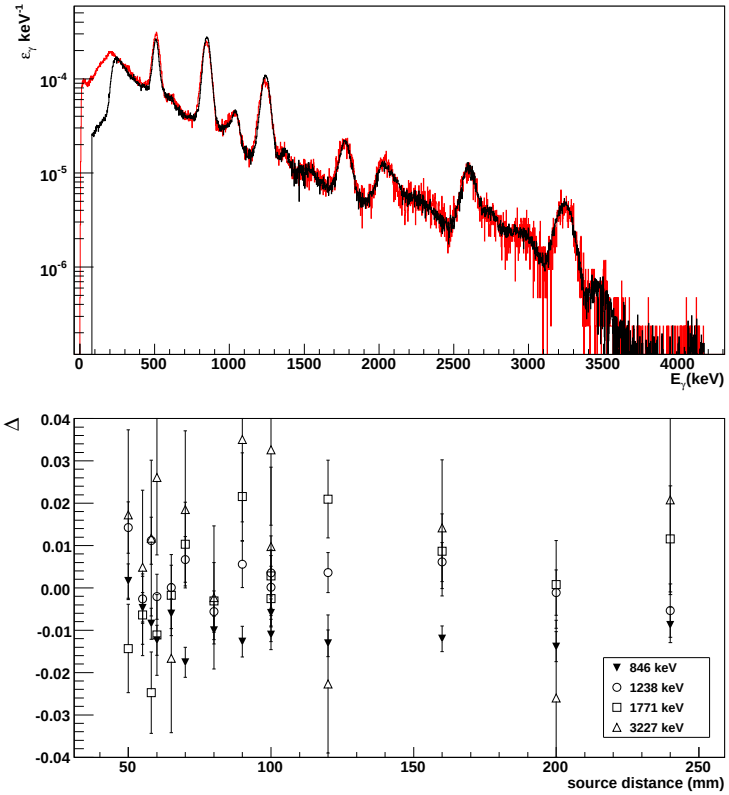

Figure 2.24: Top: Sample measured ^{56}Co γ-ray spectrum (black) and the corresponding GEANT4 simulation (red). Bottom: Comparison of simulated to measured detection efficiency ε_γ as function of the source distance, $\Delta = (\varepsilon_{\text{sim}} - \varepsilon_{\text{meas}})/\varepsilon_{\text{meas}}$.

reproducibility by the GEANT4 simulation[3] of the measured γ-ray spectrum. The yield from source B was measured with a single NaI detector at several distances, namely from 50 to 240 mm. At the closer distances the summing is significant and becomes less likely as the distance enlarges. A comparison of the measurements versus the simulations is shown in figure 2.24 along with a sample measured ^{56}Co γ-ray spectrum and the corresponding GEANT4 simulation. The results show that the simulation reproduces the measured behaviour within 4%.

The actual γ-ray detection efficiency of the detector array $k(E_\gamma)$, due to the extended nature of the gas target, is given by the folding of the detection efficiency $\varepsilon_\gamma(z, E_\gamma)$ along the beam axis and the target density profile $N_t(z)$

$$k(E_\gamma) = \frac{1}{N_t} \int N_t(z)\varepsilon_\gamma(z, E_\gamma)\mathrm{d}z \quad . \tag{2.2}$$

[3]GEANT4 uses branching ratio and angular correlation data from the Evaluated Nuclear Structure Data File [ENS].

$k(E_\gamma)$ was obtained from the GEANT4 simulation, whereas a comparison with source measurements were used to optimise the simulation. The ^{56}Co sources were small enough in size to be moved through the target chamber along the beam axis, and thus determine $\varepsilon_\gamma(z, E_\gamma)$, for E_γ corresponding to the source energies. Due to the resolution of the NaI detectors several peaks are given by the overlap of different γ-rays. Therefore only the 846, 1238 and 3253 keV transitions were analysed. The measurements were performed with source A.

The measured efficiency as a function of the distance from the target centre is shown for the 1238 keV transition in figure 2.25, the results of the GEANT4 simulation are also shown.

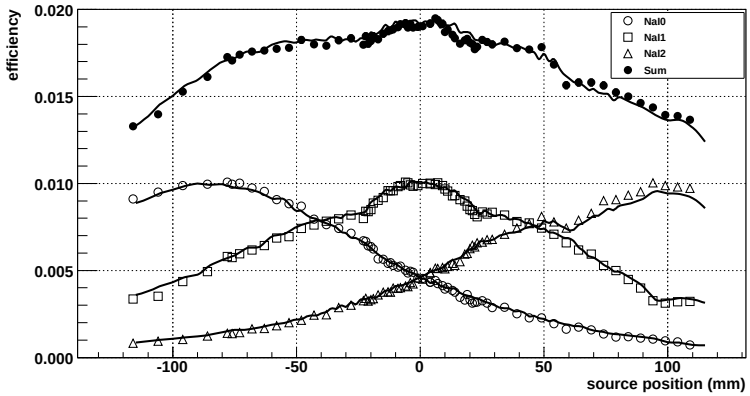

Figure 2.25: Efficiency of the NaI detector array as function of the source position along beam axis $\varepsilon_\gamma(z, E_\gamma = 1238\,\text{keV})$. The open symbols are the measured efficiencies, the full squares their sum, the solid line the result of the GEANT4 simulation.

Finally $k(E_\gamma)$ was obtained from the simulation and is displayed in figure 2.26. Each point is a simulation of monochromatic γ-rays distributed according to the target density profile. For comparison the values obtained from the source measurements are also shown, demonstrating the very good overall agreement achieved.

The dependence of $k(E_\gamma)$ on the density profile was investigated by performing several simulations of the setup with different probability distributions, i.e. by changing the event distribution as a function of the beam axis coordinate z. The efficiency of the setup was estimated for γ-rays of energy $E_\gamma = 2.8\,\text{MeV}$ with isotropic angular distribution and different density distributions, besides the one obtained from the density profile measurement that is used as a reference. To quantify the changes applied to the density profiles they are characterized with the parameters F and l_{eff}. The quantity F reperesents the relative amount of particles outside $\pm 40\,\text{mm}$ from the target centre with respect to the total thickness. The effective lenght $l_{\text{eff}} = N_t/N_t(z = 0)$ is an indication of the spatial extension of the

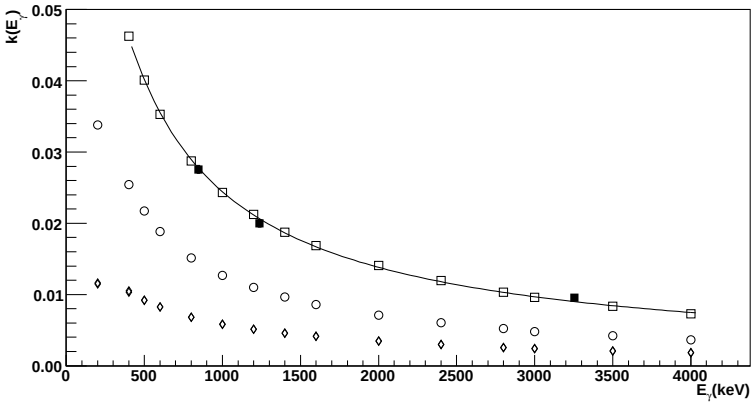

Figure 2.26: The NaI detector array efficiency $k(E_\gamma)$ as a function of the γ-ray energy. The open circles represent the efficiency of the central detector, diamonds of the side detectors, open squares their sum, the solid line is to guide the eye only. The full squares are the values obtained from measurements with the ^{56}Co source.

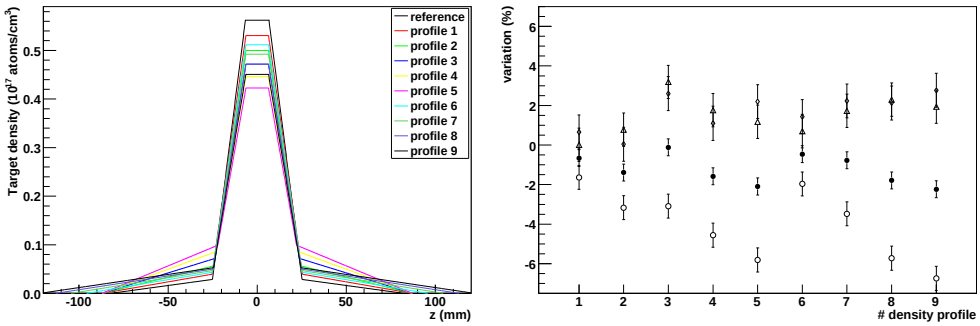

Figure 2.27: Dependence of $k(E_\gamma)$ on the target density profile. The different density profiles used for the simulation are shown in the left panel. In the right panel are plotted the variations with respect to the results obtained with the reference profile for the single detectors (open symbols) and the total (bullets).

gas.
The results obtained are shown in figure 2.27 and summarised in table 2.2. There is a sizable change in the efficiency of the single detectors, with respect to the results obtained with the reference profile. Nevertheless the variation of the total efficiency $k(E_\gamma)$ does not change significantly. Thus this feature of the detector array makes the analysis of the γ-ray measurements robust and almost independent from the actual gas density profile.

In the simulation an assumption about the angular distribution of the γ-rays was made. Since the reaction is supposed to be an external direct capture reaction

Profile #	F (%)	l_{eff}	$k(E_\gamma)$ variation (%)			
			upstream	centre	downstream	total
reference	0.04	35.6	-	-	-	-
1	0.07	37.7	0.0	-1.6	0.7	-0.7
2	0.10	40.0	0.8	-3.2	0.0	-1.4
3	0.13	42.4	3.2	-3.1	2.6	-0.1
4	0.15	44.8	1.8	-4.6	1.1	-1.6
5	0.17	47.3	1.2	-5.8	2.2	-2.1
6	0.10	39.1	0.7	-2.0	1.4	-0.5
7	0.12	40.6	1.7	-3.5	2.2	-0.8
8	0.15	42.4	2.3	-5.7	2.1	-1.8
9	0.18	44.4	1.9	-6.7	2.8	-2.2

Table 2.2: Dependence of $k(E_\gamma)$ on the target density profile.The results are compared with with the reference profile for the single detectors and their sum, see text for details.

in *s* wave it is reasonable to assume it to be isotropic at low energies. However the simulation has shown that the setup has a weak sensitivity to the angular distribution. The close distance of the detectors and the extended target do not allow to extract the angular distribution from the data. This issue is further discussed in next chapter.

In summary, the γ-ray detection efficiency has a 5% uncertainty: 4% due to the ability of the simulation in reproducing the ^{56}Co source and 1% related to the uncertainty on the density profile distribution.

Chapter 3

Experimental procedures and data analysis

In this chapter I will illustrate the experimental procedures followed to determine the total ^{3}He$(\alpha,\gamma)^7$Be cross section as well for the measurements of the γ-ray emission cross section. I will also discuss the additional measurement with the activation method that made use of the ERNA ^{3}He gas target.

3.1 Recoils measurements

The total capture cross section at the effective centre of mass energy E can be measured by counting the recoils in the end detector provided that the separator has a proper tuning, i.e. has been verified full acceptance for that energy. Since the beam energy loss in the target is small ($\Delta E < 6\,\mathrm{keV}$), the cross section can be assumed constant over the target thickness. Thus the effective energy E is

$$E = \frac{m_{^3\mathrm{He}}}{m_{^3\mathrm{He}} + m_{^4\mathrm{He}}}\left(E_{\mathrm{lab}} - \frac{1}{2}\Delta E\right) ,$$

where E_{lab} is the energy of the impinging $^4\mathrm{He}^{2+}$ ion beam.
In case the separator selects the charge state q, the number of recoils $N_{^7\mathrm{Be}^q}$ measured in the end detector is related to the cross section $\sigma(E)$ by the formula

$$\frac{N_{^7\mathrm{Be}^q}}{N_t N_{pq} T \varepsilon} = \phi_q(E)\sigma(E) \ , \tag{3.1}$$

where ε, N_t, T are the end detector efficiency, the total number of target atoms, and the recoil transmission through the separator, respectively. These quantities, and their uncertainties, have already been discussed in the previous chapter. N_{pq}

indicates the number of projectiles that hit the target and $\phi_q(E)$ is the probability for the recoils to emerge from the target in the charge state q.
The *a priori* knowledge of $\phi_q(E)$ is possible only if the ions reach charge state equilibrium. This was not achieved within the actual ^{3}He gas target. The charge state equilibrium could have been attained by adding after the target a *post-stripper*, an additional gas layer other than ^{3}He, in a similar way as in the measurement of $^{12}C(\alpha,\gamma)^{16}O$ [Sch04]. Besides the difficulties in producing a beryllium beam to measure equilibrium charge state probabilities, the post-stripper would have given an additional angular straggling to the recoils, and thus increasing the required angular acceptance. Therefore, to cover an energy range as wide as possible, the post-stripper was avoided and the reaction yield was measured for all the relevant charge states of ^{7}Be. Thus $\sigma(E)$ is obtained by summing all charge states q. From equation 3.1, using the condition $\sum_q \phi_q(E) = 1$, one gets

$$\sigma(E) = \frac{1}{TN_t\varepsilon}\sum_q \frac{N_{^7\mathrm{Be}^q}}{N_{pq}} \quad . \tag{3.2}$$

The number of projectiles N_{pq} was obtained by measuring the number of elastically scattered particles $N_{\mathrm{Si}q}$ in the silicon detector facing the target cell centre at 75° with respect to the beam axis, see figure 2.16. The two quantities are directly proportional, $N_{pq} = N_f N_{\mathrm{Si}q}$, with the *normalisation factor* $N_f \propto \frac{1}{\sigma_{scattering}}$.

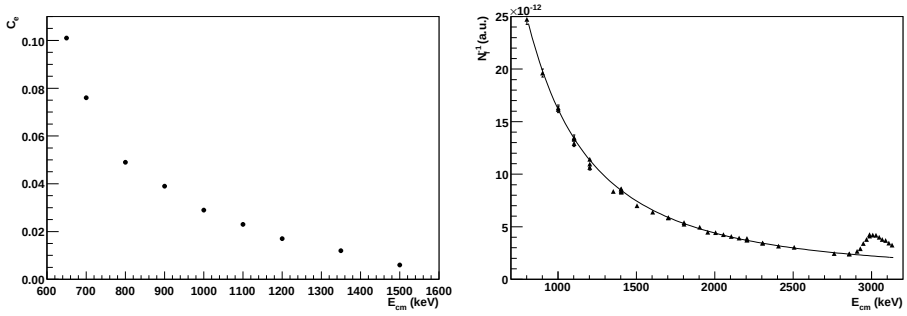

Figure 3.1: Left: correction C_e to FC2 beam charge integration. Right: the inverse of N_f as a function of the centre of mass energy. The deviation from Rutherford scattering (solid line) in the energy region of the ^{7}Be second excited state is visible.

For each measurement N_f was obtained by measuring the ratio of the yield N_{Si} in the target silicon detectors to the charge Q concurrently collected in the Faraday cup after the gas target (FC2). Thus

$$N_f = \frac{(1+C_e)Q}{q_{\mathrm{beam}}e}\frac{1}{N_{\mathrm{Si}}} \quad ,$$

where e is the electron charge, C_e is a correction for the charge exchange of the beam particles in the target gas. The evaluation of C_e was done by integrating

beam current in FC2 with and without gas in the target cell. The correction C_e turned out, as shown in left panel of figure 3.1, to be negligible for $E_{\mathrm{cm}} > 1.5\,\mathrm{MeV}$, and increases at lower energies due to the increasing probability for the projectiles to populate the 1+ charge state. In the right panel of figure 3.1 the inverse of N_f is shown as a function of the centre of mass energy. At energies below $E_{\mathrm{cm}} = 2.9\,\mathrm{MeV}$ the energy dependence follows the $1/E^2$ Rutherford law, while at higher energies the resonance structure corresponding to the ^{7}Be second excited state at $E_x = 4.57\,\mathrm{MeV}$ is observed.
In summary, the procedure described allowed to establish N_{pq} with ~1% precision above $E_{\mathrm{cm}} = 1.5\,\mathrm{MeV}$ and increasing, with decreasing energy, up to 4% for the minimum measurement energy. The systematic uncertainty due to current integration was estimated to be 1%, that is the typical difference found in reading the same current in the different Faraday cups.

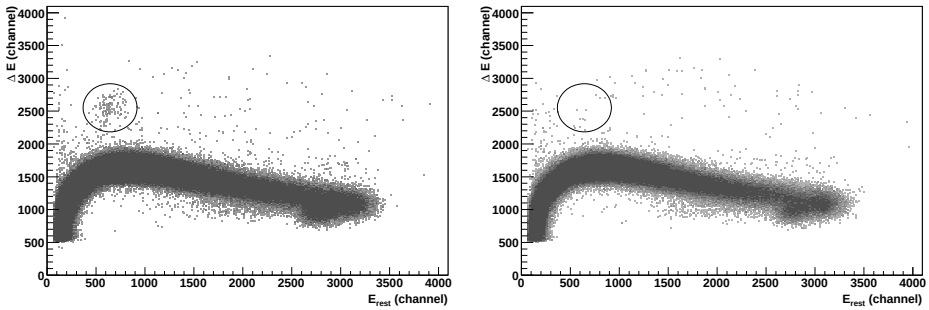

Figure 3.2: Examples of ICT ΔE-E spectra acquired at $E_{\mathrm{cm}} = 1.20\,\mathrm{MeV}$. Left is the measurement for 1+ and right is the relative background. The separator's suppression factor was $\sim 1 \times 10^{-10}$. The ^{7}Be ROI is also shown.

Finally the number observed recoils $N^{meas}_{^7\mathrm{Be}^q}$ was obtained by counting in the bi-dimensional spectrum, E_{rest}-ΔE or ToF–E, the events in the region of interest (ROI) where ^{7}Be ions were expected. An example of an ICT spectrum ($E_{\mathrm{cm}} = 1.20\,\mathrm{MeV}, q = 1+$) is shown in figure 3.2 left panel, the ^{7}Be ROI is also indicated. The ROI was kept the same for all charge states at the same measurement energy. As already discussed in section 2.5.3, possible contributions to the recoil yield other than the $^3\mathrm{He}(\alpha,\gamma)^7\mathrm{Be}$ reaction were expected to be negligible. Nevertheless background runs were performed at each measurement energy to check for beam contaminants, parasitic ^{7}Be production and to evaluate the amount of recoil-like pile-up events. The background runs were carried out by changing the target gas to ^{4}He. In none of the background run spectra events that could be addressed to parasitic production or beam contamination were observed. The main source of background-like events was pile-up, occurring in case the suppression of the separator was not sufficient to keep the rate in the end detector below about 1000

events per second. Since the leaky particle trajectories are most likely to be originated by elastic scattering on the target cell collimators and on the WF1 plates, the leaky rate, and thus the pile-up rate, was strongly influenced by beam focusing and alignment. The pile-up rate was also related to the impinging beam intensity, since it depends on the number of particles reaching the end detector per time unit. Therefore it was of utmost importance to keep, for the background measurements, the same conditions with respect to all of these factors. Thus for each energy the background runs were performed right after the measurement of the recoil yields were accomplished, granting conditions as close as possible to the measurement. $N_{^7\mathrm{Be}^q}$ was obtained as

$$N_{^7\mathrm{Be}^q} = N^{meas}_{^7\mathrm{Be}^q} - \frac{N^{meas}_{pq}}{N^{bkg}_{pq}} N^{bkg}_{pile-up} \quad ,$$

where superscript *meas* and *bkg* refer to measurement and background runs, respectively. For the ^{4}He-^{4}He elastic scattering the probability for the particles to be emitted at $\theta_{\mathrm{lab}} = 75^\circ$ is about 10^{-3} lower than for the ^{4}He-^{3}He case. This made the use of the rate in the target Si detector impractical to evaluate N^{bkg}_{pq}. This difficulty was overcome by normalizing the number of projectiles to the number of leaky particles, i.e. $N^{meas}_{pq}/N^{bkg}_{pq} \simeq N^{meas}_{leaky}/N^{bkg}_{leaky}$. Because of this assuption great care was taken in keeping the same leaky rate in the end detector for the measurement and the corresponding background run. Changing from measurement to background the structure of the leaky beam does not change. At all energies the background run leaky particle distribution on the strips of the Si detector is almost identical to the respective measurement run distribution. An example is shown in figure 3.3, for the measurement $E_{\mathrm{cm}} = 800\,\mathrm{keV}, q = 1+$. Thus the normalization of the

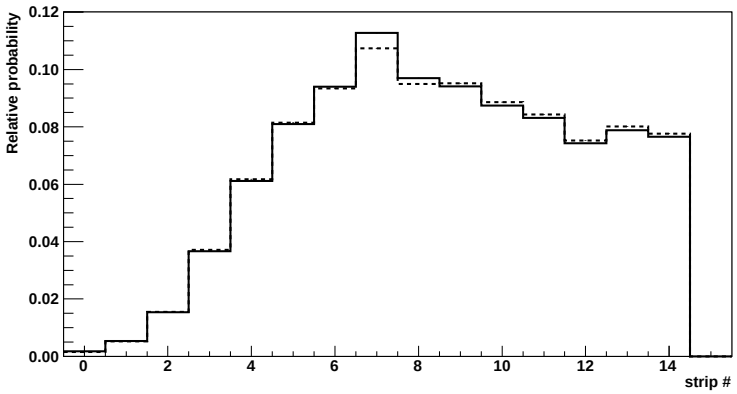

Figure 3.3: Leaky particles distribution in the horizontal plane at end detector position for the $E_{\mathrm{cm}} = 800\,\mathrm{keV}, q = 1+$ measurement. Solid and dashed line represent measurement and background runs, respectively.

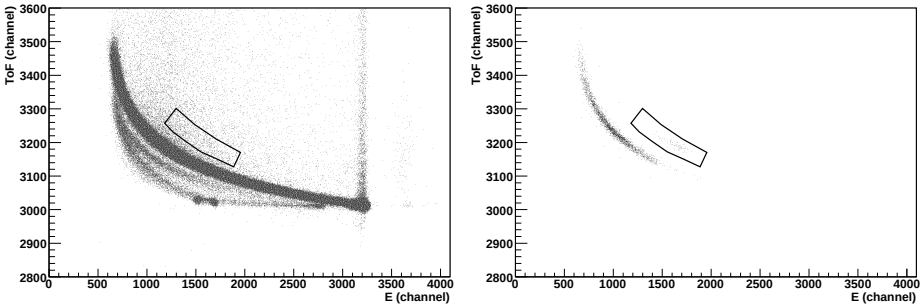

Figure 3.4: Time of flight vs energy spectra for $E_{\mathrm{cm}} = 0.80\,\mathrm{MeV}$. Left: $q = 1+$ measurement, suppression factor of the separator 3×10^{-9}. The replica of the main structure due to the contact ragion (section 2.4.1) are clearly visible. Right: $q = 2+$ measurement, suppression factor 5×10^{-11}. The ^{7}Be ROI is indicated.

beam intensity to the leaky rate is reliable and the uncertainty associated with it is negliglible.

The background due to pile-up events was usually a minor fraction of the total counting rate, $\lesssim 5\%$. This was not the case for measurements of $q = 1+$ recoils charge state at $E_{\mathrm{cm}} \leq 1.0\,\mathrm{MeV}$. This is an effect of the increase in the necessary acceptance with decreasing energy combined with the lower analyzing power of the velocity filters with decreasing charge state, essentially due to the limitation in the maximum achievable magnetic field. In these cases another analysis procedure was adopted. In this energy range only the ToF-E end detector was used. The analysis procedure is illustrated for the measurement at $E_{\mathrm{cm}} = 0.80\,\mathrm{MeV}$, whose $q = 1+$ ToF-E spectra is shown figure 3.4 left panel. The ^{7}Be ROI, also shown in figure, was identified on the basis of the 2+ measurement that had negligible amount of pile-up events due to a better suppression of the primary beam, figure 3.4 right panel. Essentially, to get a clearer signal signature, the energy spectra of the 16 strips of the silicon detector were summed up for the events selected in the ROI, both for the measurement run and the background run, as shown in figure 3.5. The number of recoils $N_{^{7}\mathrm{Be}^{1+}}$ is given by the difference of the sum spectra. The ROI in the sum spectrum is obtained from the $q = 2+$ measurement sum spectrum.

The measurements performed with the 16 strips Si detector provided some information on the spatial distribution of the recoils at the detector position in the horizontal plane, that is the most critical, because of the separator optics. In all measurements it was verified that the largest counting rate was observed in the central strips, with few or no counts on the outer strips, see figure 3.6. This indicates that the recoils were well focused toward the centre of the detector. It can be noted that the 1+ charge state is not as well focused as the other charge states.

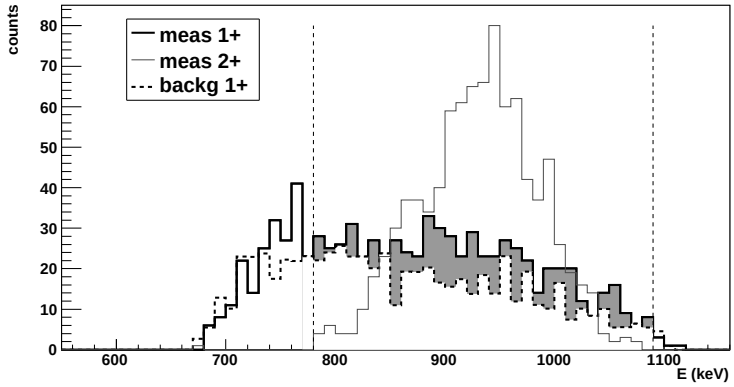

Figure 3.5: ^{7}Be yield for $E_{\mathrm{cm}} = 0.8\,\mathrm{MeV}, q = 1+$. Thick solid line is the sum of the 16 Si spectra of measurement run, the dashed line is the corresponding for background run, their difference is highlighted by the shadowed area. The thin solid line is the $q = 2+$ recoil spectrum used to identify the ROI (vertical bars).

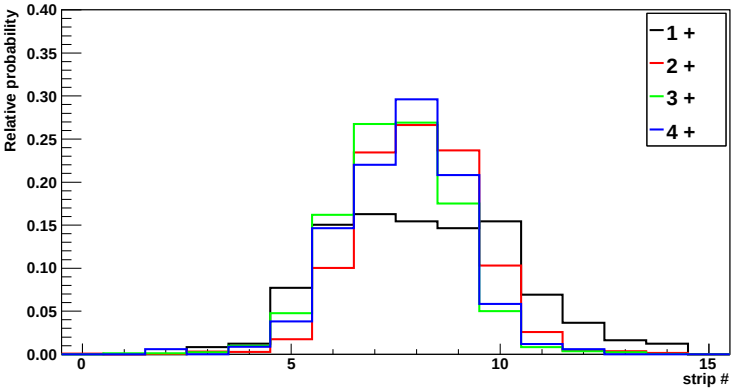

Figure 3.6: Recoil distribution in the horizontal plane at the end detector position for a measurement at $E_{\mathrm{cm}} = 1.2\,\mathrm{MeV}$.

This is most likely due to the limitation in the maximum achievable magnetic field of sepWF1, that in turn reflects in a smaller focusing effect on the recoils having an energy most different from the central one.

Recoil measurements where carried out in the energy region 0.70 to 3.15 MeV. The measured yields are reported, as a function of the centre of mass energy, in left panel of figure 3.7. The high efficiency in recoil detection allowed to reach good precision in a relatively short measuring time. Measurements lasted from less than one hour to a maximum of ten to get a single experimental point. The precision achieved is in the order of 2% or better for the measurements above $E_{\mathrm{cm}} = 1.10\,\mathrm{MeV}$, see table B.1. At lower energies the uncertainty is larger, domi-

nated by the uncertainty on the 1+ charge state yield.

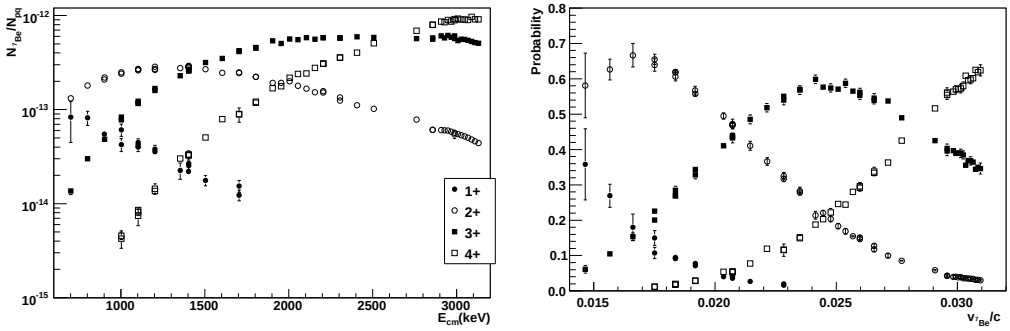

Figure 3.7: Left: measured yields for the relevant recoils charge states. Right: probabilities for the recoils to emerge from the target in the charge state q with a $^4He^+$ beam.

In right panel of figure 3.7 are shown, as a function of the recoil velocity, the relative probabilities for the recoils to emerge from the target in the charge state q. They are obtained as $\phi_q = Y_q / \sum_q Y_q$. The probabilities follow approximately a gaussian distribution. It has to be stressed that these are non equilibrium probabilities, characteristic for the actual gas target and the impinging beam charge state. Thus the results do not provide atomic physics information.
As regards the neutral charge state, it is considered to be negligible at all energies. For the higher energies this appears clear from the right panel of figure 3.7, since the 3+ and 4+ dominate and the lower charge states are disfavoured. For the lower energies several observations support the assumption. Since the target atoms are neutral, it is reasonable that the recoils are created in the same charge state of the incoming beam particles, in the case of this work 2+, although there are some evidences for the recoils to be created in an even higher charge state [Sch04]. The small target thickness does not favour the electron exchange of the recoils with the target atoms to populate the neutral charge state. Even if charge state equilibrium would be reached within the target, at the lowest measurement energy the neutral charge state would amount to not more than 4% [Mar68].

3.2 Prompt γ-rays measurements

The long lasting issue of the discrepancy between the results of the prompt γ-ray and the activation measurement methods was a trigger to investigate the cross section for radiative transition in the $^3He(\alpha,\gamma)^7Be$ reaction. Under this respect the separator approach is an ideal tool, since the total cross section and the radiative

cross section refer to the same physical events. Therefore at selected energies the cross section for radiative transition σ_γ was measured concurrently to the total cross section. Any ratio $\sigma_\gamma/\sigma < 1$ would mean the presence of a *monopole* transition, i.e. a decay channel in which the energy excess is not radiated by a γ-ray but used in a different process, e.g. pair emission or internal conversion. The γ-ray detector array used for this purpose has been presented in section 2.6.

As already mentioned in the first chapter the ^{3}He$(\alpha,\gamma)^7$Be may proceed through two different channels: transition directly to the ground state or through the cascade via the first excited state of ^{7}Be at $E_x = 429$ keV.

Since the setup was not optimised for γ-ray detection, the *free* γ-ray energy spectrum was dominated by the beam induced background. The γ-ray background was mainly produced on the central target cell collimators by the ^{27}Al$(\alpha, p)^{30}$Si reaction. A sample free γ-ray spectrum collected at $E_{\rm cm} = 2.15$ MeV, obtained by triggering the Data Acquisition system (DAQ) by any event in the NaI detector array, is shown as dashed line in figure 3.8. From this spectrum only little information could be obtained, since only the full energy peak of the ground state transition (gsfep) can be identified. The γ-rays due to the cascade transition are not identifiable at all.

Because of the concurrent recoil detection it is possible, by requiring the *coincidence condition*, to select in the γ-ray spectra only the events produced in the

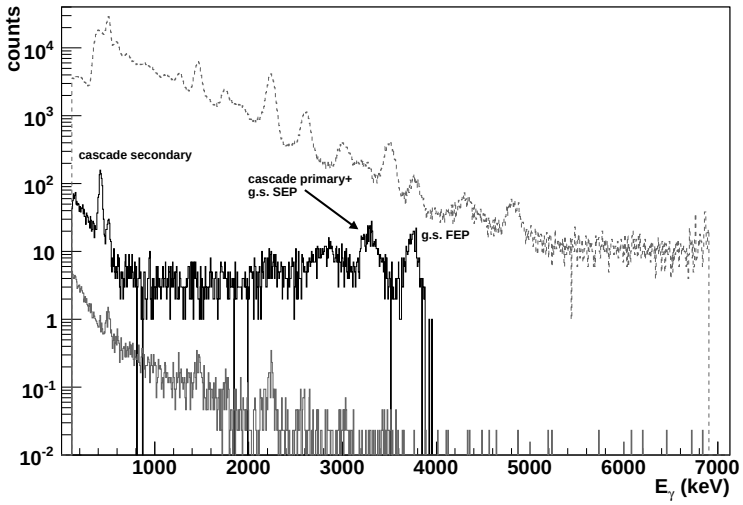

Figure 3.8: γ-ray spectrum collected at $E_{\rm cm} = 2.15$ MeV (dashed line). The coincidence condition with the ^{7}Be recoils allows to obtain a background suppression of about 4 orders of magnitude and to identify the reaction γ-rays (solid black line). The background due to random coincidences with the recoils is also reported (solid grey line), see text for details.

reaction. The coincidence condition means that a γ-ray event is taken only if it happened in a given time window with respect to a recoil detection. The width of the time window was essentially set by the *rise time protection* (rtp) of the DAQ, i.e. the time the DAQ waits for signals to be converted after it is triggered, usually the rtp was set to $9\,\mu$s. The coincidence spectrum is shown with a solid black line in figure 3.8.
It was still possible that in the rtp window a background γ-ray was detected as a random coincidence. Nevertheless the amount of random coincidences with room or beam induced background could be precisely estimated, making use of the fact that the detection of leaky particles is randomly distributed with respect to reaction γ-ray detection. Thus the background spectrum due to random coincidences is obtained by selecting the γ-rays in coincidence with the leaky particles detected in the end detector. The random background spectrum has to be normalised by the ratio $N_{^7\mathrm{Be}^q}/N_{\mathrm{leaky}^q}$ of the number of events used to build the coincidence spectra. The random background spectrum is also shown, grey line, in figure 3.8.

The number $N_{\gamma q}$ of γ-rays detected while selecting recoils in the charge state q is

$$N_{\gamma q} = \sigma_\gamma N_t N_{pq} \int \varepsilon_\gamma(\mathrm{z}, E_\gamma)\phi_q(\mathrm{z}, E)\varepsilon \mathrm{dz} \ , \tag{3.3}$$

the term $\phi_q(z, E)\varepsilon$ is due to the coincidence condition with the recoils. The functions $\phi_q(z, E)$ are the (unknown) probabilities for a recoil to be created in the position z along the gas target and enter the separator having charge state q. Not necessarily the recoil is created in the charge state q. Thus the functions $\phi_q(z, E)$ satisfy the condition

$$\int \phi_q(\mathrm{z}, E)\mathrm{dz} = \phi_q(E) \ .$$

Since the recoils do not reach charge state equilibrium in the target $\phi_q(z, E)$ are not necessarily uniform on the whole target thickness. Nevertheless, since the cross section is assumed constant over the target thickness, that is the reaction probability is the same over the same amount of target atoms, the sum over q of $\phi_q(z, E)$ has to follow the target density profile:

$$\sum_q \phi_q(\mathrm{z}, E) = \frac{N_t(z)}{N_t} \ .$$

Dividing both sides of equation 3.3 by N_{pq} and summing over q one obtains

$$\sum_q \frac{N_{\gamma q}}{N_{pq}} = \sigma_\gamma N_t \varepsilon \int \varepsilon_\gamma(\mathrm{z}, E) \sum_q \phi_q(\mathrm{z}, E)\mathrm{dz} = \sigma_\gamma N_t k(E_\gamma) \ .$$

The detector array efficiency $k(E_\gamma)$ has been defined in the previous chapter (equation 2.2). Dividing the last expression by equation 3.1 one gets

$$\frac{\sigma_\gamma}{\sigma} = \frac{\sum_q N_{\gamma q}/N_{pq}}{\sum_q N_{^7\mathrm{Be}^q}/N_{pq}} k(E_\gamma) \ .$$

If different channels are available to the γ-ray emission this last equation has to be evaluated for any transition γ_i and then summed up

$$\frac{\sigma_\gamma}{\sigma} = \frac{\sum_i \sigma_{\gamma i}}{\sigma} = \frac{1}{\sum_q N_{^7\mathrm{Be}^q}/N_{pq}} \sum_q \frac{1}{N_{pq}} \sum_i N_{\gamma i\, q} k(E_{\gamma i}) \ . \tag{3.4}$$

The efficiencies $k(E_{\gamma i})$ are obtained from the GEANT4 simulation as the ratio of the number of events given by the simulation in the E_γ ROI, the same set in the experimental spectra, with respect to the total number of events generated in the simulation. $k(E_{\gamma i})$ depends on the details of the transition to be considered. In particular, if more γ-rays are present in the same event, summing effects have to be evaluated. Angular distributions also must be considered.
It has been shown in the previous chapter that the GEANT4 simulation fairly well describes the summing of cascade transitions. Thus in the estimation of $k(E_\gamma = 429\,\mathrm{keV})$ both γ-rays of the cascade transition were considered in a single event. The results show that the yield of the cascade secondary is changed by about 3% by summing-out. The summing of full energy of both γ-rays, mimicking full energy peak events, is very small ($< 0.2\%$).
Two γ-ray angular distributions are found in literature for the reaction, isotropic and the direct capture model of [Tom63] (TP), originally used to describe the data of [Par63]. The model is used to calculate the angular distribution up to $E_{\mathrm{cm}} = 3.4\,\mathrm{MeV}$. While at very low energies the reaction occurs in s wave ($l = 0$) isotropy can be assumed. With increasing energy the higher partial waves $l = 2, 3$ may become more relevant, especially in correspondence of the second excited state of ^{7}Be, and lead to a non isotropic, eventually asymmetric, angular distribution. As mentioned in chapter 1 angular distribution were measured by [Krä82] for E_{cm} between 0.15 and 1.29 MeV, thus at higher energies no experimental informations are available. The influence of the two angular distributions on $k(E_{\gamma i})$ was estimated with the GEANT4 simulation.

As an example the central detector coincidence spectrum at $E_{\mathrm{cm}} = 2.15\,\mathrm{MeV}$, subtracted of the random coincidence background, is shown in figure 3.9, together with the results of the GEANT4 simulation of the different transitions.

For the ground state transition the number of events N_{gsfep} was readily obtained by integrating the spectrum in the gsfep ROI.
As regards the cascade, the primary γ-ray could not be used in the analysis since, because of the resolution of the detectors, it could not be clearly separated from

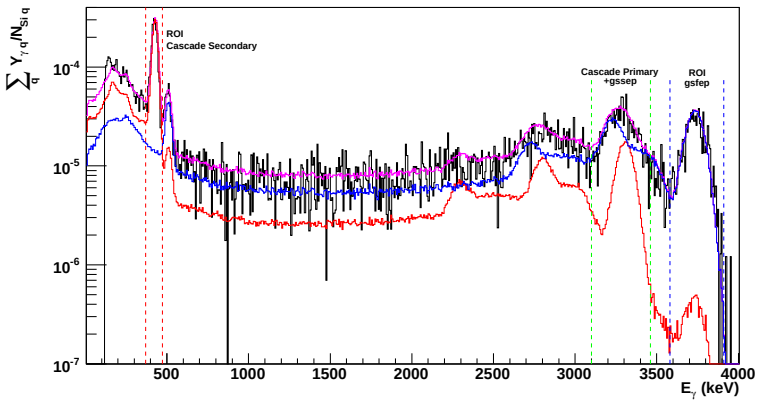

Figure 3.9: Experimental γ-ray energy spectrum (black) of the central NaI detector at $E_{\mathrm{cm}} = 2.15\,\mathrm{MeV}$. For comparison the results of the GEANT4 simulation are shown: ground state transition (blue), cascade transition (red) and their sum (magenta).

the single escape peak (gssep) and the compton edge of the ground state transition.
The number of events in the cascade secondary ROI N_{429}^{meas} contains also the contribution of events due to the *compton tail* of the ground state transition. From the experimental spectrum was difficult to estimate this background. Then it has been obtained from the intensity of the primary times $\varepsilon_{\mathrm{compton}}$: the detection efficiency for the compton events, generated by the ground state transition, in the 429 keV ROI. $\varepsilon_{\mathrm{compton}}$ was evaluated from the simulation. Thus the number of events due to the cascade secondary N_{429} is

$$N_\gamma(429) = N_{429}^{\mathrm{meas}} - N_{\mathrm{gsfep}} \frac{\varepsilon_{\mathrm{compton}}}{k(E_{\mathrm{gsfep}})} \quad ,$$

The obtained results for σ_γ/σ are shown in figure 3.10, for both the isotropic or the TP angular distribution assumption. As is evident no significant differences were found whether one or the other was used in the analysis of the experimental data. This is a result of the little sensitivity of the detection setup to the angular distribution.
A consistency check about the angular distributions is given by the yields of the three individual detectors. For this purpose the measured yield Y_{meas}^i in detector $i (i = 1, 2, 3)$ is compared with the expected yield Y_{sim}^i calculated from the simulation assuming σ_γ as derived from the sum of the three detectors. The values $\Delta_{ij} = (Y_{\mathrm{meas}}^i - Y_{\mathrm{sim}}^i)/Y_{\mathrm{meas}}^i$ are plotted in figure 3.11, assuming either isotropic or TP angular distribution, the index $j = 1, 2$ is used to indicate ground state and cascade transition, respectively.

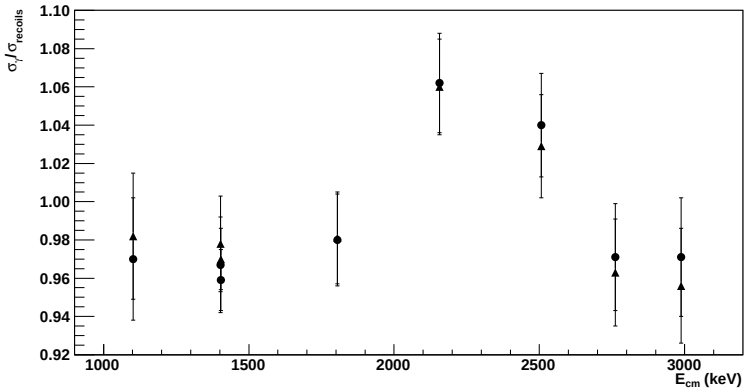

Figure 3.10: Ratio of σ_γ with respect to σ for the performed measurements as obtained assuming the isotropic angular distribution (bullets) and the prediction of [Tom63] (triangles).

Both angular distributions describe fairly well the observed relative yields in the different detectors at E_{cm} below 2.5 MeV, while at higher energies significantly larger deviations are observed. This appears to be more evident if the sum over the detectors and the transitions $\sum_{ij}(\Delta_{ij}/\sigma_{\Delta_{ij}})^2$ is calculated for each energy, and is shown in figure 3.12. While the values at $E_{\mathrm{cm}} \leq 2500$ keV do not differ significantly from their average, the values for $E_{\mathrm{cm}} = 2.75$ and 2.98 MeV do show a remarkable difference. Since the angular information provided by our γ-ray detector setup is insufficient to fix the parameters of the angular distributions, these latter data points were excluded from the results.

3.3 Activation measurements

As a further consistency check on the transmission and detection of the recoils off-beam measurements were performed to obtain cross section values independent of the recoil separator.
For this purpose the nuclei produced by the ^{3}He$(\alpha,\gamma)^7$Be reaction need to be collected and subsequently the activity of the ^{7}Be was to be determined. Thus a circular copper catcher ($\phi = 70$ mm) was installed at the exit of the gas target, i.e. at a distance of 31 cm from the gas target centre, in order to have recoils implanted into it. The measurements were performed at $E_{\mathrm{cm}} = 650, 1103$ and 2504 keV. The ^{4}He beam current was of the order of 2 μA. According to SRIM MC calculations, the probability of backscattering and sputtering is negligible for all of the three measurements. The mean implantation depths are 1.0, 1.4, and 2.5 μm, respectively. The beam power dissipated in the catcher was small enough to prevent any

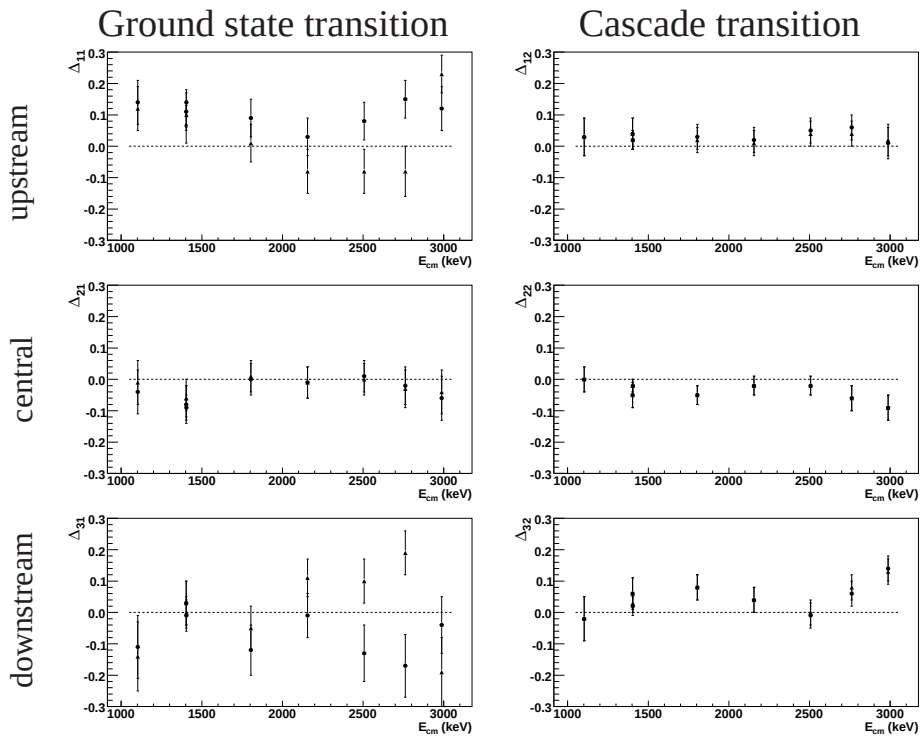

Figure 3.11: Comparison of detectors measured yields with predictions of the GEANT4 simulation, $\Delta_{ij} = (Y^i_{\text{meas}} - Y^i_{\text{sim}})/Y^i_{\text{meas}}$, see text for details. Filled circles and triangles indicate results assuming the isotropic or TP angular distribution, respectively.

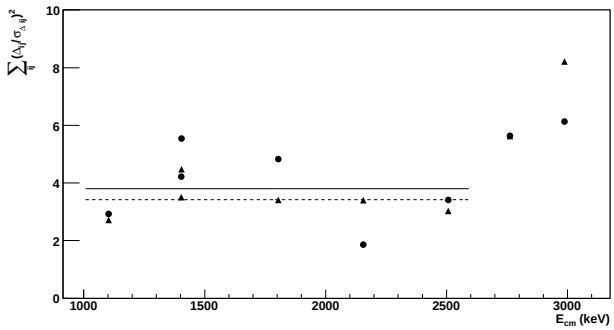

Figure 3.12: $\sum_{ij}(\Delta_{ij}/\sigma_{\Delta_{ij}})^2$ of the previous figure. The solid and dashed lines indicate the average of the values for $E_{\text{cm}} \leq 2.5\,\text{MeV}$ assuming isotropy (filled circles) or TP (triangles) angular distribution, respectively.

blistering of the surface. This was verified by optical inspection of the catchers with a microscope at the end of the implantation runs.
The catcher was electrically insulated from the beam-line. Current reading on the catcher was used for the initial beam focusing. Since no electron suppression was present such reading was not suitable to estimate the number of impinging projectiles. Therefore the beam current estimate was obtained from the elastic scattering in the target Si detectors. The normalisation factors were obtained from previous measurements, since the beam could not reach FC2 due to the presence of the catcher.

Bombarding the target with a beam intensity I_α the number of $N_{^7\mathrm{Be}}$ of implanted recoils follows the law

$$\frac{\mathrm{d}N_{^7\mathrm{Be}}}{\mathrm{d}t} = \sigma N_t I_\alpha - \lambda N_{^7\mathrm{Be}} \ ,$$

where the term $\sigma N_t I_\alpha$ is the production rate and the term $-\lambda N_{^7\mathrm{Be}}$ takes into account the decay of the nuclei. If the current is constant after a time period of duration T the total number of implanted nuclei is

$$N_{^7\mathrm{Be}} = \frac{\sigma N_t I_\alpha}{\lambda}\left(1 - e^{-\lambda T}\right) \ .$$

In order to take into account that the beam current was not constant during the irradiation, each production run was divided into sub-periods of 20 minutes: $\Delta t_i = t_i - t_{i-1}, t_0 = 0, i = 1, \ldots N$. The production of ^{7}Be was calculated for each sub-period from the average current I_i, determined from the scattering rate in the target Si detectors, see figure 3.13. The sharp drops of current in figure are due to stops needed for beam intensity checks and refocusing. The number of implanted re-

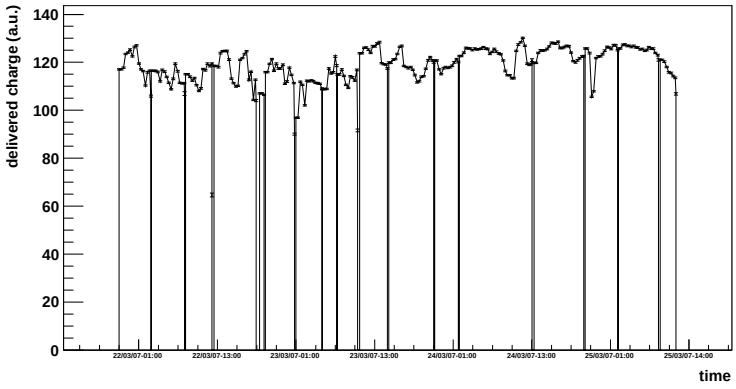

Figure 3.13: Delivered charge on target during the activation at $E_{\mathrm{cm}} = 1100\,\mathrm{keV}$.

coils at the end of the nth sub-period is

$$N_{^7\mathrm{Be}\,n} = N_{^7\mathrm{Be}\,n-1}\,[1 - \lambda\Delta t_i] + \sigma N_t I_n \Delta t_n = \sigma N_t \sum_0^n I_i \Delta t_i e^{-\lambda(t_n - t_i)} \quad .$$

This last equation assumes that none of the recoils produced in the nth sub-period decays during that particular period. Since $\Delta t_i \ll 1/\lambda$ this approximation has no effect on the results.
Thus the activity $A_0 = \lambda N_{^7\mathrm{Be}\,N}$ of the implanted recoils at the end of the irradiation, $t = t_N$, is related to σ by the relation

$$\sigma = \frac{A_0}{\lambda N_t \sum_0^N I_i \Delta t_i e^{-\lambda(t_N - t_i)}} \quad . \tag{3.5}$$

The activity of the collected nuclei was determined by measuring the 477.6 keV γ-ray emitted in the de-excitation of the first energy level of ^{7}Li populated in the electron capture decay of the ^{7}Be. The setup used for the counting measurement is the same of [Gyü07] at the underground Low-Level Laboratory of the Laboratori Nazionali del Gran Sasso, Italy. The reduction of the cosmic ray induced background due to the natural shielding of 1400 meters of rock allows the measurement of counting rates as low as $3 \times 10^{-4}\,\mathrm{s}^{-1}$. The counting setup consisted

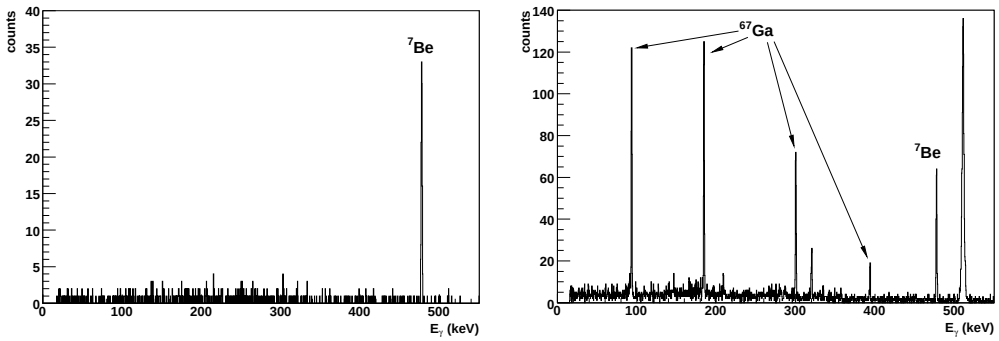

Figure 3.14: HPGe spectra from the low background laboratory at LNGS. Left: irradiation at $E_{\mathrm{cm}} = 1.1\,\mathrm{MeV}$. Right: irradiation at $E_{\mathrm{cm}} = 2.5\,\mathrm{MeV}$

of a HPGe detector additionally shielded with low contamination lead and copper. The irradiated samples were placed in close geometry to the detector, the distance sample to detector was $\sim 5\,\mathrm{mm}$. Sample spectra are shown in figure 3.14: in the left panel is shown the spectrum obtained from the catcher irradiated at $E_{\mathrm{cm}} = 1.10\,\mathrm{MeV}$, while in the right panel is reported the spectrum for the activation at $E_{\mathrm{cm}} = 2.5\,\mathrm{MeV}$. In the first spectrum only the ^{7}Be decay γ-ray is present.

In the second spectrum are present also background lines due to the decay of ^{67}Ga, produced by the interaction of beam particles with the catcher material through the ^{63}Cu$(\alpha,\gamma)^{67}$Ga reaction.
In order to ensure that no parasitic production of ^{7}Be was induced in the catcher a background measurement run was performed using ^{4}He, at the same pressure of ^{3}He as target gas at $E_{\mathrm{cm}} = 2.5\,\mathrm{MeV}$. In this case the total number of projectiles was estimated from the average current measured every few hours. The background has shown that the upper limit for parasitic production of ^{7}Be is 0.5%. The counting rates of the semples were obtained by integrating the γ-ray spectra with typical intervals of few days. The number of events was determined by counting events in the 478 keV peak assuming a linear background. The background was estimated averaging the number of counts detected in two regions adjacent to the peak ROI, as shown in figure 3.15.

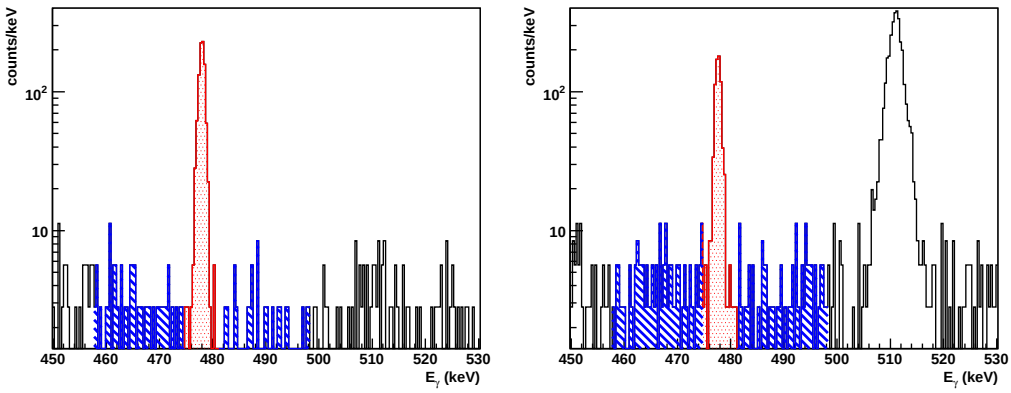

Figure 3.15: Determination of the counting rate from the measurement spectrum. The regions for background average estimation are highlighted. Left: irradiation at $E_{\mathrm{cm}} = 650\,\mathrm{keV}$. Right: irradiation at $E_{\mathrm{cm}} = 2.5\,\mathrm{MeV}$.

The rate as a function of the measurement time for the $E_{\mathrm{cm}} = 650\,\mathrm{keV}$ catcher is shown in figure 3.16. The initial activity is obtained from a fit to the data with the exponential decay function

$$A(t) = A_0 \varepsilon_{\mathrm{Act}} b \exp(-\lambda(t - t_N)) \ , \tag{3.6}$$

where b is the probability for the first excited state of ^{7}Li to be populated in the decay. The quantity $\varepsilon_{\mathrm{Act}}$ is the efficiency of the delayed γ-ray counting setup. The value of $\varepsilon_{\mathrm{Act}}$ was obtained from source measurements. Nevertheless since the samples were in very close geometry, a correction due to the ^{7}Be distribution on the catcher must be evaluated. This was done with a GEANT4 simulation of

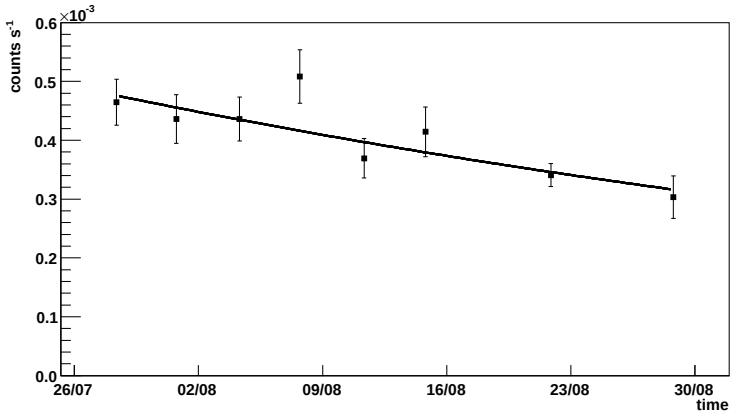

Figure 3.16: Measured counting rate for the sample activated at $E_{\mathrm{cm}} = 650\,\mathrm{keV}$. The curve through the points is the fit to estimate the initial activity.

the setup [Bem06, Gyü07]. The simulation needs as input an accurate evaluation of the areal distribution of the implanted recoils on the catcher, for a proper estimation of $\varepsilon_{\mathrm{Act}}$. This distribution was given by the results of the realistic simulation of straggling in the target gas, as explained in section 2.3. The efficiency of the counting setup for these samples was estimated to be $\varepsilon_{\mathrm{Act}} = (11.3 \pm 0.2)\%$ [Bem07].

The values extracted for the initial activity, as well the cross section values obtained by means of equation 3.5, are reported in table B.3. The results are fully consistent with the recoil measurements, thus confirming the robustness of the experimental procedures and of the analysis followed for this work.

Chapter 4

Results

In this chapter the results of the total cross section, the γ-ray coincidence measurements, and the activation measurements will be presented. The comparison with results of other experiments, and the extrapolation to stellar energies, implies the choice of a theoretical model among the several proposed. This choice will be done according to the experimental data available. Finally the implications of the results for astrophysics will be briefly outlined.

4.1 Experimental results

In figure 4.1 the experimental results of the measurements, in the form of the astrophysical S-factor are plotted for all of the three methods used: recoils, prompt γ-rays, and activation. Their numerical values are given in tables B.1, B.2, and B.3 in appendix B. The results of the prompt γ-ray measurement are given according to the isotropic angular distribution hypothesis, see section 3.2. In figure 4.1 the results of previous works in the overlapping energy range are also shown for comparison.
Table B.2 reports also the results of the experimental determination of the cascade-to-ground state transition intensity ratio $R = \sigma_{429}/\sigma_{gs}$. The ratio R is plotted, and compared with results of previous works, in figure 4.2.

The uncertainty on the energy determination, essentially set by the beam energy loss in the target (< 3 keV), gives a negligible contribution to the uncertainty on the S-factor, less than 0.5% at the lowest measurement energy.

All three methods agree within their uncertainties. The consistency of recoil with prompt γ-ray results confirm that there is no evidence for a non-radiative transition. In fact the average value of the ratio of radiative transition with respect to the total cross section, for $E_{\mathrm{cm}} \leq 2.5$ MeV, is $\sigma_\gamma/\sigma = 0.99 \pm 0.05$, see fig-

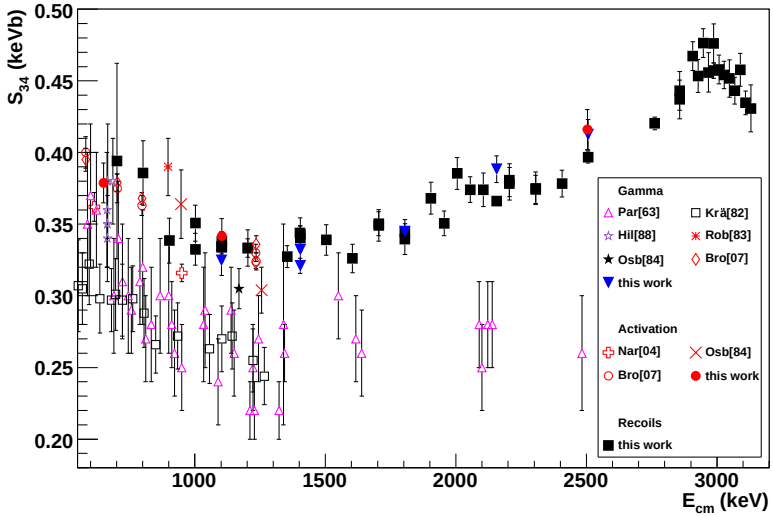

Figure 4.1: Results of the cross section measurements of the present work. The data are plotted in the form of the astrophysical S-factor as a function of E_{cm}. The results of previous works in the same energy range are also shown.

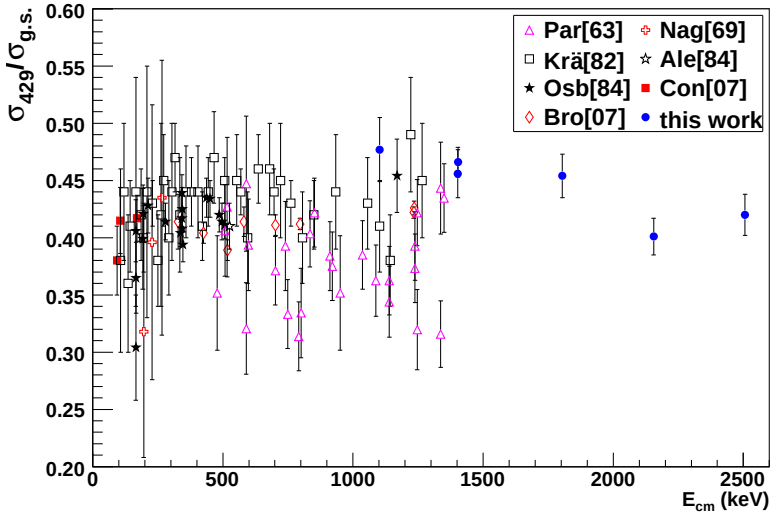

Figure 4.2: Ratio of the cascade-to-ground state transition intensity measured in this work as a function of E_{cm}. The results of previous works are also shown.

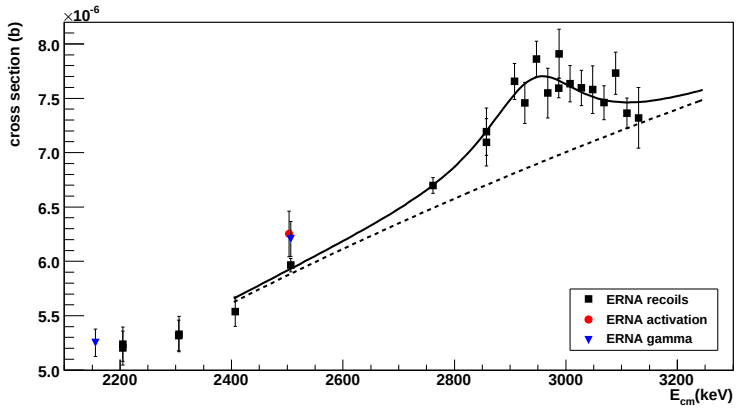

Figure 4.3: Fit to the cross section experimental data to determine the resonance parameters. The full line is the fitting function, while the dashed line represents the non resonant part σ_{NR}, see text for details.

ure 3.10. The consistency between recoil and activation results confirms that the transmission and detection of the recoils are correctly evaluated.

It is worth noting that the resonance corresponding to the $J^{\pi} = 7/2^{-}, E_x = 4.57 \pm 0.05$ MeV state in ^{7}Be [Til02] was observed for the first time in this channel. To obtain the parameters E_R and Γ, resonance energy and width, respectively, a fit to the data was performed. The cross section was parametrised in the region of the resonance as a non resonant part, given by a decreasing exponential function, $\sigma_{\mathrm{NR}} = A \exp\left(-B/\sqrt{E}\right)$, plus a Breit-Wigner function σ_{BW}:

$$\sigma = \sigma_{\mathrm{NR}} + \sigma_{\mathrm{BW}} = \sigma_{\mathrm{NR}} + \frac{C}{(\Gamma/2)^2 + (E - E_R)^2} \quad .$$

From the measured values $\sigma_i \pm \delta\sigma_i$ at energy E_i the least square function $L = \sum_i \left(\frac{\sigma(E_i)-\sigma_i}{\delta\sigma_i}\right)^2$ in the energy range $2400 \leq E_{\mathrm{cm}} \leq 3130$ keV was calculated[1]. The minimum of L corresponds to the best estimate of the parameters and their errors. The minimisation was done using the routine MINUIT [Jam75]. The obtained

[1]The quantity L is a χ^2 variable only under the conditions: that the model is adequate to describe the data; that the fitted measurements are independent; that the measured quantities have a gaussian distribution, whose standard deviations must be correctly evaluated. For some of the fits to be presented in the following the probability that L follows a χ^2 probability distribution is very low.

parameter values for σ are

$$\begin{aligned} A &= 0.9 \pm 0.3\,\mathrm{b}\ , \\ B &= 206 \pm 16\,\mathrm{keV}^{\frac{1}{2}}\ , \\ C &= (2.7 \pm 1.7) \times 10^{-4}\,\mathrm{b\,keV}^{-2}\ , \\ \Gamma &= (2.1 \pm 1.0) \times 10^{2}\,\mathrm{keV}\ , \\ E_R &= 2942 \pm 15\,\mathrm{keV}\ . \end{aligned}$$

These results compare to literature values of $\Gamma = 175 \pm 7\,\mathrm{keV}$ and $E_R = E_x - Q = 2.98 \pm 0.05\,\mathrm{MeV}$ [Til02], respectively.
The strength of the resonance can be obtained from $\sigma(E)$ by the following equation [Rol88]:

$$\omega\gamma = \frac{1}{2\pi^2 \lambda\!\!\!^{-2}_R} \int_0^\infty \sigma_{\mathrm{BW}} \mathrm{d}E = \frac{1}{2\pi} \frac{\mu E_R}{656.6} \int_0^\infty \sigma_{\mathrm{BW}} \mathrm{d}E = 0.33 \pm 0.21\,\mathrm{eV}\ ,$$

where the reduced wavelength value is $\lambda\!\!\!^{-}_R = \frac{656.6}{\mu E_R}\,\mathrm{b}$ if the reduced mass μ is expressed in amu and the centre of mass resonance energy E_R in keV. The value of the decay width in the γ-ray channel Γ_γ is obtained from the relation

$$\omega\gamma = \left[\frac{2J_R + 1}{(2J_{^3\mathrm{He}} + 1)(2J_{^4\mathrm{He}} + 1)}\right] \frac{\Gamma_p \Gamma_\gamma}{\Gamma_p + \Gamma_\gamma}\ ,$$

were J_R is the spin of the resonance level, $J_{^3\mathrm{He}} = 1/2$ and $J_{^4\mathrm{He}} = 0$ are the nuclear spins of ^{3}He and ^{4}He, and Γ_p is the decay width in the particle channel. Since $\Gamma_p \gg \Gamma_\gamma$ the last term reduces to Γ_γ, and thus for the observed resonance $\Gamma_\gamma = \omega\gamma/4$. For the resonance it can be assumed a decay only to the ground state, that is a $7/2^- \rightarrow 3/2^-$ $E2$ transition. This assumption is well grounded since the transition to the first excited state $7/2^- \rightarrow 1/2^-$ should occur via an $M3$ transition that is highly disfavoured with respect to $E2$ transitions [Bla52]. The value of $\omega\gamma$ corresponds to the single-particle estimate for the $E2$ multipole reduced electric transition probability

$$B(E2) = \frac{\Gamma_\gamma}{\hbar} \frac{1}{1.223 \times 10^9 E_x^5} = 52 \pm 31\,e^2\mathrm{fm}^4\ .$$

$B(E2)$ essentially represents the probability of γ-ray emission if it would be caused by a transition of one single proton, moving independently within the nucleus, from one nuclear state to another.
The model of [Moh93] obtains a value of $B(E2) = 23\,e^2\mathrm{fm}^4$. A more sophisticated calculation based on the nuclear shell-model [Cor05], that includes also core polarisation effects, gives a value of $B(E2) = 12\,e^2\mathrm{fm}^4$ [Cor08]. Thus it appears that models are not able to account for the strength of the resonance, although one should be aware of the large error affecting the estimate of $\omega\gamma$.

4.2 S_{34}(0) extrapolation

To obtain the S-factor at any energy a theoretical model is usually fit to the data. It is common to specify the normalisation of the model with its value at $E_{\rm cm} = 0$: $S_{34}(0)$.
The model that better describes the ^{3}He$(\alpha,\gamma)^7$Be S-factor has to be chosen on the basis of all the experimental data sets available. Nevertheless it appears clearly in figure 4.1 that some of the data sets do not agree. In fact the S-factor values obtained in the present work show a significant discrepancy, on both the absolute scale and the energy dependence, from the results of [Par63], that is the data set with the largest energy range overlap. As already pointed out in section 1.2, the intensity ratio in [Par63], as shown in figure 4.2, deviates significantly from all other determinations, including the present data. The influence of this discrepancy on the cross section is difficult, or even impossible, to evaluate. Even larger is the discrepancy with the results of [Krä82]. However, as mentioned in the first chapter, those data need a renormalisation by a factor 1.4, as suggested by [Hil88]. On the normalisation factor an error of 28% applies, and thus these data provide a weak constrain on the absolute scale of the S-factor. In regard to [Nar04], the agreement is only within 2σ. An excellent agreement is found with the determination of [Osb84] and the recent measurement of [Bro07]. The comparison with the remaining data sets is more complex, since it must be done necessarily through the model calculation. The quantitative estimation on the agreement of the various experiments with each other needs a proper statistical analysis, considering the statistical and systematic uncertainty for each measurement (subsection 4.2.2).

4.2.1 Choice of the model

As mentioned in the first chapter several models are available in literature. Since the ^{3}He$(\alpha,\gamma)^7$Be is considered an external capture, the cross section is calculated from the electromagnetic operator expanded as electric and magnetic multipole operators, connecting the initial and final state wave functions. According to the way the wave functions are determined the models can be classified in two different groups: potential models and microscopic models.
In the potential models the initial wave function is expressed as a function of the experimentally determined elastic scattering phase shifts. The final wave function depends on the reduced widths of the bound state, that can be derived from the measurement of $\sigma_{\gamma 429}/\sigma_{\gamma \rm gs}$. Thus the only free parameter in the model is an absolute intensity parameter that is obtained from a fit to the cross section data.
The microscopic models, instead, try to describe the 7 nucleon system, in a more or less detailed way, as clusters of nucleons interacting through a nucleon-nucleon (NN) potential. The parameters of the NN potential are adjusted to match the

properties of target, projectile, and compound system, like scattering phase shifts and energy levels. The cross section calculated in this approach do not contain an absolute intensity parameter.

In the following I consider the models given in [Liu81, Mer86, Kaj87, Moh93, Csó00, Nol01, Des04]. Although the calculation of [Des04] is *R*-matrix based, since no resonances are present in the energy range considered, it reduces to a potential model calculation, indeed very similar to the predictions of [Tom63]. The models are claimed to be valid for $E_{\mathrm{cm}} \lesssim 2\,\mathrm{MeV}$, therefore comparison with data of the present work will be limited to this energy range.

Unfortunately, to choose which model better describes the $^3\mathrm{He}(\alpha,\gamma)^7\mathrm{Be}$ S-factor, a global analysis of all the experimental data available is not possible. In fact in several works the quoted uncertainties include systematic errors, namely [Par63, Nag69, Krä82, Hil88]. A deconvolution of the errors is not possible on the basis of the published information. Thus the results obtained by least square fits to these data sets would be not statistically correct. The works of [Rob83, Ale84, Vol83] measured each a single data point, so they provide no test of the model energy dependence.

Hence to establish which calculation better describes the experimental data a least square fit of each model is performed separately to: [Osb84] prompt γ-ray, [Osb84] activation, [Nar04], LUNA prompt (prompt γ-ray measurements of [Con07]), LUNA activation (delayed activity measurements of [Bem06, Gyü07, Con07]), [Bro07] prompt, [Bro07] activation, and results of this work for recoil and activation measurements. The least square fits of the model to the data were obtained by scaling each calculation by a constant factor c. This procedure is somewhat questionable for microscopic models, but the possible inaccuracy resulting from the scaling stays small when $c \approx 1$.

The values of the minima of the least square function L are given in table 4.1. If L follows a χ^2 probability distribution its expected value is the number of degrees of freedom ν and the variance is $\sqrt{2\nu}$. The fits are assumed consistent with the data considering a conservative confidence level of 95%, i.e. the probability that the model is discarded altough it is correct is 5% or less.

The prompt γ-ray data of [Osb84] are not fitted by any model, this is due to the fact that the external error is larger than the quoted internal error, therefore little information on the model can be obtained from this data set. The LUNA data sets are fitted equally well by all models. This is due to the fact that the energy range covered by the experiments is too narrow to give any information on energy behaviour of the S-factor. Although the data of [Nar04] cover a relatively wide energy interval they also do not constrain the model since they are well fitted by all calculations, because of the relatively low precision. Thus the only data sets that can be used to discriminate models are [Bro07] and the present work data. The only models that are compatible with both data sets are [Kaj87] and [Nol01],

	[Osb84] prompt	[Osb84] activation	[Nar04]	LUNA prompt	LUNA activation	[Bro07] prompt	[Bro07] activation	this work recoils	this work activation
ν	18	1	3	2	6	7	7	21	1
[Des04]	86	1.6	1.1	0.8	6.6	20.2	5.3	72	1.8
[Kaj87]	83	2.3	1.4	0.7	6.6	9.6	12.3	28	0.4
[Csó00]	95	2.5	0.9	1.4	6.7	18.8	3.4	17	1.1
[Mer86]	79	2.4	1.7	0.4	9.2	15.4	10.9	46	0.8
[Liu81]	79	2.4	2.8	0.1	7.3	16.5	21.5	32	0.3
[Nol01]	83	2.5	0.9	0.7	6.6	10.7	10.0	18	0.7
[Moh93]	91	1.5	2.0	1.2	6.6	31.1	6.6	75	2.7

Table 4.1: Least square function minima of the different models to the data sets in the energy range $E_{\mathrm{cm}} \leq 2.0\,\mathrm{MeV}$. The number of degree of freedom ν is indicated for each data set. The colours indicate different confidence level: $<$ 85%, 85% $\leq$ $<$ 95%, 95% $\leq$.

although one should be aware that the normalisation factor c is significantly different from 1 in both cases, $\sim$ 1.15 and $\sim$ 1.4, respectively. In general, it is not possible to quantify the uncertainty introduced by this normalisation.
As regards the discarded models it is readily seen from table 4.1 that the model of [Des04] provides a poor fit to the results of present work. The calculation is shown in figure 4.4. The disagreement is due to the fact that the slope of the S-factor is not reproduced for $E_{\mathrm{cm}} \gtrsim 1.2\,\mathrm{MeV}$. Since the energy dependence of the S-factor in potential model calculation is essentially fixed by the spectroscopic factors there is no room for improvements within this model.
The model of [Csó00] provides a very good fit to the present work results, but does not fit the prompt γ-ray data of [Bro07]. The model of [Liu81] (and very similarly of [Mer86]) has a change in the slope around $E_{\mathrm{cm}} \sim 200\,\mathrm{keV}$, see figure 4.4, that has no physical explanation and most likely is due to numerical problems in the calculation [Hof08].

4.2.2 $S_{34}(0)$

To put on a quantitative basis the agreement of the different data sets the calculation of [Kaj87], or [Nol01], is assumed to be valid. The $S_{34i}(0)$ value is calculated according to the model for each data set compatible with the model, figure 4.5

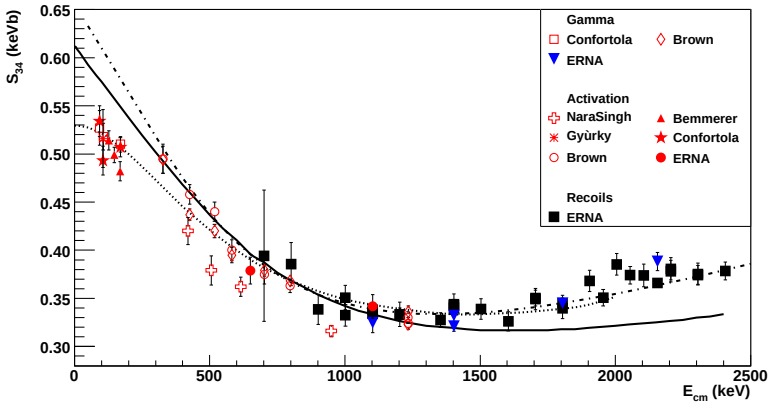

Figure 4.4: Comparison of the models to experimental data. Solid curve calculation of [Des04], dotted [Liu81], dash-dotted [Csó00]. The curves are scaled to best fit present work results, for [Des04] the fit is performed only to data points at $E_{\mathrm{cm}} \leq 1.2\,\mathrm{MeV}$.

bottom panel. The error σ_i affecting the extrapolation is obtained adding quadratically the systematic error affecting the measurement to the statistical error obtained by the fitting procedure. In case in the same experiment more than one measurement technique was used, namely LUNA, [Bro07], and present work, the results are combined, taking into account the common systematic uncertainty according to the prescription of [D'A94]. The obtained $S_{34i}(0)$ values, and relative uncertainty, are very similar for both calculations since their energy dependence differ significantly only for $E_{\mathrm{cm}} \gtrsim 1.5\,\mathrm{MeV}$, figure 4.5 top panel.

The compatibility of the different $S_{34i}(0)$ values was tested by evaluating the quantity

$$w_{ij} = \frac{\left|S_{34i}(0) - S_{34j}(0)\right|}{\sqrt{\sigma_i^2 + \sigma_j^2}}$$

for each possible pair of extrapolations $i - j$. w_{ij} follows a standard normal probability distribution $G(w)$. In table 4.2 the probability $P(w > w_{ij})$ that w exceeds the calculated value w_{ij} is reported. The compatibility of the extrapolations is assumed with a confidence limit of 95%, i.e. the experiments are considered not compatible if $P(w > w_{ij}) < 5\%$. This test shows that the $S_{34}(0)$ extrapolated from the data of [Rob83] and [Ale84] are not statistically compatible with the determinations of some other experiments, and therefore will not be used in the following analysis.

The best estimate for $S_{34}(0)$ is the weighted average of the results of the com-

patible experiments. The mean values for $S_{34}(0)$ are 0.570 ± 0.022 keV b and 0.566 ± 0.020 keV b for the [Kaj87] and [Nol01] model, respectively. Since the internal error is smaller than the external error, the latter is quoted as the error on the mean value. The external error is calculated as $\sqrt{\sum_i^N [S_{34i}(0) - \langle S_{34}(0)\rangle]^2/(N-1)}$. Thus the best estimate is

$$S_{34}(0) = 0.569 \pm 0.023 \text{ keV b} \quad .$$

This procedure is more robust than recently proposed analyses, since physical models have been used for the extrapolation (e.g. [Cyb08] uses a polynomial expansion of the S-factor) and the statistical treatment of the data does not need arbitrary adjustment of the errors (as done in [Cos08]). The quoted error repre-

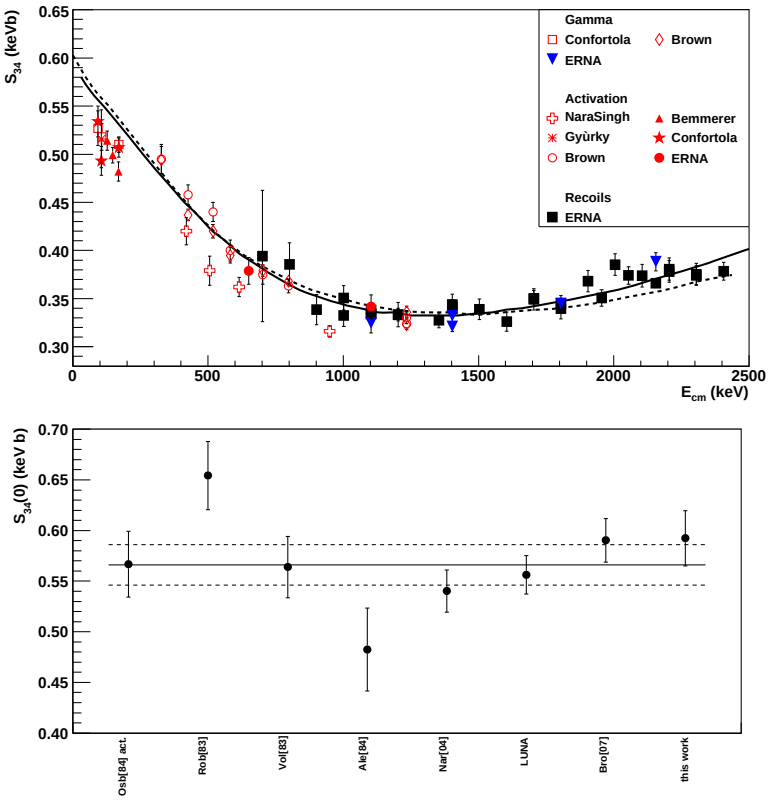

Figure 4.5: Comparison of the models to experimental data. Top panel: solid curve calculation of [Nol01], dashed [Kaj87]. The curves are scaled to best fit present work results. Bottom panel: extrapolated $S_{34}(0)$ values according to the model of [Nol01], the continuous line represents the weighted average while the dashed lines 1σ deviation. Very similar results are obtained with the model of [Kaj87].

	[Rob83]	[Vol83]	[Ale84]	[Nar04]	LUNA	[Bro07]	this work
[Osb84] activation	0.06	0.91	0.13	0.51	0.80	0.50	0.46
[Rob83]		0.04	0.00	0.00	0.01	0.13	0.18
[Vol83]			0.15	0.58	0.90	0.40	0.37
[Ale84]				0.24	0.12	0.02	0.02
[Nar04]					0.58	0.09	0.09
LUNA						0.21	0.21
[Bro07]							0.90

	[Rob83]	[Vol83]	[Ale84]	[Nar04]	LUNA	[Bro07]	this work
[Osb84] activation	0.06	0.95	0.11	0.49	0.78	0.55	0.56
[Rob83]		0.04	0.00	0.00	0.01	0.11	0.14
[Vol83]			0.11	0.52	0.83	0.48	0.49
[Ale84]				0.21	0.10	0.02	0.02
[Nar04]					0.57	0.09	0.13
LUNA						0.23	0.28
[Bro07]							0.98

Table 4.2: Probability to obtain a value of w larger than the calculated, see text for details. The colours indicate different confidence level: $< 68\%$, $68\% \leq < 95\%$, $95\% \leq$. Top: extrapolation according to the [Kaj87] model. Bottom: extrapolation according to the [Nol01] model.

sents the uncertainty to the determination of $S_{34}(0)$ due to statistical fluctuations of the experimental information used. The contribution to the error that may come from the rather large normalisation of the models is assumed to be negligible, i.e. I assume that the energy dependence of the S-factor at energies below 1 MeV is predicted correctly by the [Kaj87] and [Nol01] calculations. To establish the validity this assumption is beyond the scope of this work, since it needs an improved theoretical calculation, compatible with all experimental data, able to predict the absolute scale of the S-factor within few percent.

The *popular* recommendations for $S_{34}(0)$ are are from [Ade98] (0.53 ± 0.04 keV b) and the more recent of [Ang99] (0.54 ± 0.09 keV b). Thus the proposed result is 6-8% larger than previously assumed. This fact has some consequences in astrophysics that will be discussed in next section.

4.3 Impact on astrophysics

The improved $S_{34}(0)$ determination from the previous section has an influence on the predictions of the Big Bang Nucleosynthesis and of the Standard Solar Model.

As mentioned $S_{34}(0)$ gives the normalisation of the theoretical prediction. Thus the value of $S_{34}(0)$ given in the previous section implies that in the energy range relevant for BBN the reaction rate is larger by about 8% compared to what is obtained by using the widely accepted $S_{34}(0)$ estimation of [Ade98].
The impact of such an increase on the prediction of primordial ^{7}Li abundance has been evaluated using the BBN code of [Pis08] with the WMAP determination for the baryon fraction $\Omega_b h^2 = 0.02273 \pm 0.00062$ [Hin09]. A value $^7\mathrm{Li/H} = (5.4 \pm 0.2) \cdot 10^{-10}$ is found [Man08]. The quoted uncertainty on ^{7}Li/H takes into account all relevant nuclear processes involved in ^{7}Li and ^{7}Be production/destruction. The better precision $S_{34}(0)$ reflects in a better precision on the prediction: 4% compared to the 8% of [Ser04], obtained with an earlier version of the same BBN code. This theoretical determination of ^{7}Li/H is larger than the observational value by a factor 3 or more, see e.g. [Cyb08], thus worsening the primordial ^{7}Li problem.

The progress in the solar neutrino experiments and the more precise determination of neutrino mass parameters by means of reactor neutrino experiment [Abe08] allow for the possibility of exploiting neutrinos to study the solar interior [Hax08]. Therefore, it will be possible to test the SSM and, more in general, to better understand the evolution of low mass stars. Independent checks of the solar core composition are of great interest also in consideration of the *new solar problem* due to the recent determination of the metal content of convective zone. The new metal abundances significantly alter the agreement between SSM and helioseismology in the temperature region below the solar convective zone.
The $S_{34}(0)$ result obtained in this work implies an increase in the calculated Standard Solar Model neutrino fluxes from decay of ^{7}Be and ^{8}B by approximately 7% [Bah04]. This in turn has an influence on the estimated counting rates in the neutrino detectors (BOREXINO, SNO, etc), that rely on the SSM to interpret their experimental results. More remarkable is the reduction of the uncertainty to a *precision* level, a crucial point to exploit CN neutrinos from the solar core [Hax08]. Although a similar value and uncertainty for $S_{34}(0)$ were already suggested by [Cos08] the analysis was based on a questionable statistical treament of the data. The results of this work, with strong constrain given to the model that has to be used for the extrapolation and with a proper statistical treatment of the experimental information, give to the $^3\mathrm{He}(\alpha,\gamma)^7\mathrm{Be}$ nuclear input to the SSM a solid ground.

Summary and Outlook

In this work I presented the preparation and the results of the ^{3}He$(\alpha,\gamma)^7$Be reaction cross section measurement with the recoil separator ERNA. This is a novel approach that has given a substantial contribution to the improvement of the knowledge about ^{3}He$(\alpha,\gamma)^7$Be. The cross section was measured, with an unprecedented accuracy, in a wide energy range, $E_{\rm cm} = 0.70$ to $3.13\,$MeV. In particular for the first time has been observed in this channel the ^{7}Be resonance at $E_x = 4.57\,$MeV, leading to the estimation of the strength of the resonance $\omega\gamma = 0.33 \pm 0.21\,$eV.
The complementary measurements of the prompt and delayed γ-rays have been also carried out. The in-beam γ-ray measurements confirmed, as also [Con07] and [Bro07], that no non-radiative contribution is present in this reaction. The activation measurements have given a direct comparison of the *standard* measurement techniques with the measurement carried out with the separator.

One of the outcome of this work is that the experimental results cannot be described by the simple direct capture model, although for several calculation it is supposed to be accurate in the investigated energy range, e.g. [Tom63, Des04]. A better description is obtained by calculations based on microscopic models. The extrapolation of the S-factor to zero energy $S_{34}(0)$ needs the choice of one of such calculations. This choice has been done on the basis of the results of this work and of a selection of the available experimental information. This selection is needed since in some cases the quoted uncertainties include the systematic errors. It was found that the only two data sets giving substantial information to discriminate among models are the present work data and the data of [Bro07].
The models that are able to describe all of the selected experimental data are the calculations of [Kaj87] and [Nol01]. No substantial difference was found whether the [Kaj87] or the [Nol01] calculation was used for the extrapolation of $S_{34}(0)$. The best estimate is $S_{34}(0) = 0.569 \pm 0.023\,$keV b, where the systematic uncertainty associated to the different data sets were properly taken into account.
The error quoted on $S_{34}(0)$ reflects only the statistical fluctuations of the experimental information. The scaling of the models to fit the experimental data is sizable, the additional uncertainty carried by this scaling, in particular on the slope of the S-factor at low energy, was neglected. An evaluation of this error is beyond

the scope of this work.

The statistical approach followed in this work in the treatment of the experimental information gives to the $S_{34}(0)$ result, and the corresponding uncertainty, a firm ground. The solidity of the result is reflected in the consequences sketched for the two astrophysical scenarios where the role of ^{3}He$(\alpha,\gamma)^7$Be is relevant, the BBN and the solar neutrino spectrum.

It has been shown that the major unsettled aspect of ^{3}He$(\alpha,\gamma)^7$Be S-factor at low energy is the theoretical description. A calculation, within the framework of microscopic models, able to predict the absolute value of the S-factor not further off than few percent is needed. Since the models make use of the experimentally determined elastic scattering phase shifts, an experiment devoted to check such phase shifts in the energy region above 3 MeV could be useful. In fact in this energy region the available data were determined essentially by the same group. An experiment that could determine the S-factor in the energy interval $E_{\rm cm} \sim 0.2$ to ~ 1.5 MeV with an accuracy comparable with the present work results is in any case desirable.

This work has confirmed that the recoil separator approach for the measurement of the cross section of astrophysical relevant radiative capture reactions is very advantageous. The possibility to reach good statistical precision, without any corrections, the ability to easily extend the energy range toward higher energies is very valuable. The high energy data, as in this work, can give substantial information on the models used for the extrapolation toward stellar energies and/or evidence aspects previously neglected, as in the case of the ^{12}C$(\alpha,\gamma)^{16}$O reaction [Sch05, Sch07].

Appendix A

Basic concepts of nuclear astrophysics

Energy production in stars occurs through fusion of two atomic nuclei. The generic reaction is indicated as $A(x,y)B$, with A the target, usually the heavier nucleus, x the projectile, y the ejectile and B the recoil nucleus. The Q-value of the reaction is defined as

$$Q = (m_A + m_x - m_B - m_y)c^2 \ ,$$

if $Q > 0$ the reaction is said to be exothermic, and it can occur with any energy in the centre of mass, although the probability of the reaction to happen, the cross section σ, is influenced by the coulomb and centrifugal barriers.
Charged particle reactions, occurring in s wave ($l = 0$), can be depicted as in figure A.1. Classically with projectile energy $E < E_C$, the nuclear reaction cannot occur since the incoming particle does not enter the nuclear potential well ($r < R_n$), because the coulomb repulsion will allow the impinging particle to approach only up to $r = R_C$. Nevertheless quantum mechanics predicts a non vanishing probability for the incoming particle to penetrate the barrier by *tunnel effect*. In case $E \ll E_C$, or equivalently $R_C \gg R_n$, the tunnelling probability is

$$P \simeq \exp(-2\pi\eta) \ , \tag{A.1}$$

where η is the Sommerfeld parameter

$$\eta = \frac{Z_A Z_x e^2}{\hbar}\left(\frac{2\mu}{E}\right)^{\frac{1}{2}} = \frac{Z_A Z_x e^2}{\hbar v} \ ,$$

with e the electron charge, Z_A and Z_x the nuclear charges of target and projectile nuclei, respectively, v the relative velocity and μ the reduced mass.

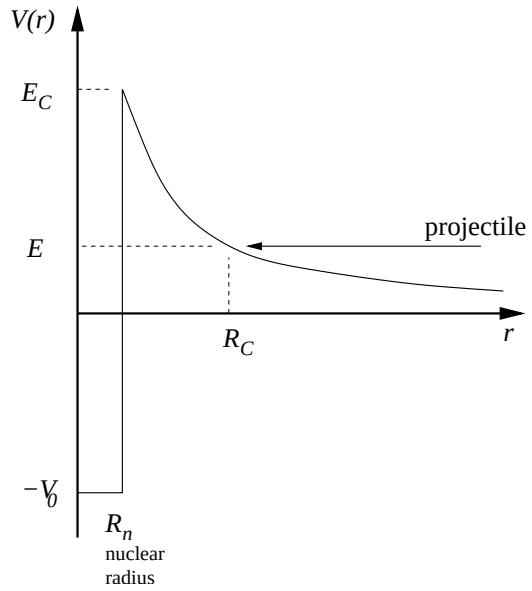

Figure A.1: Schematic representation of the potential seen by the projectile in a nuclear reaction in *s* wave. It is given by the nuclear potential well for $r < R_n$ and by the Coulomb potential $V(r) = \frac{Z_A Z_x e^2}{r}$ for $r > R_n$.

It is useful to express $\sigma(E)$ as

$$\sigma(E) = \frac{1}{E} \exp(-2\pi\eta) S(E) \ . \tag{A.2}$$

In this way one can factorise the cross section dependence as a geometrical factor $1/E$, a penetrability factor $\exp(-2\pi\eta)$ strongly decreasing with E, and nuclear factor $S(E)$, defined by this equation. $S(E)$ is called the *astrophysical* or *nuclear S factor*.

In a stellar environment, the relevant quantity, instead of σ, is the number of reaction per unit time and unit volume: the reaction rate r.
Then let N_A and N_x be respectively the number of target and projectile particles per unit volume, and let $\phi(v)$ be their relative velocity distribution. The reaction rate per particle pair is

$$r = N_A N_x \langle v\sigma(v) \rangle = \int_0^\infty \phi(v) v\sigma(v) \mathrm{d}v \ , \tag{A.3}$$

In quiescent burning phases the stellar core is a non degenerate particle gas in thermal equilibrium at the temperature T. In such cases $\phi(v)$ is the Maxwell-

Boltzmann distribution and thus

$$\phi(v) = 4\pi v^2 \left(\frac{m}{2\pi k_B T}\right)^{\frac{3}{2}} \exp\left(-\frac{mv^2}{2k_B T}\right) \ ,$$

then A.3, becomes

$$\langle\sigma(v)v\rangle = \left[\frac{8}{\pi\mu(k_B T)^3}\right]^{\frac{1}{2}} \int_0^\infty \sigma(E) e^{-\frac{E}{k_B T}} E \mathrm{d}E \ , \tag{A.4}$$

with $E = \frac{1}{2}\mu v^2$ relative kinetic energy. Inserting A.2 in A.4 one obtains

$$\langle\sigma(v)v\rangle = \left[\frac{8}{\pi\mu}\right]^{1/2} \frac{1}{(k_B T)^{\frac{3}{2}}} \int_0^\infty S(E) \exp\left(-\frac{E}{k_B T} - \frac{b}{E^{1/2}}\right) \mathrm{d}E \ , \tag{A.5}$$

where

$$b = (2\mu)^{\frac{1}{2}} \frac{\pi e^2 Z_A Z_x}{\hbar} \simeq 0.989 Z_A Z_x \sqrt{\mu(\mathrm{amu})}\,\mathrm{MeV}^{\frac{1}{2}} \ ,$$

b^2 is called Gamow energy. The product of the two exponential terms in the integrand of equation A.5 leads to a peak having its maximum at the energy E_0, usually larger than $k_B T$. The peak is referred to as the Gamow peak, whose qualitative behaviour is shown in figure A.2. Since $S(E)$ usually has a smooth energy

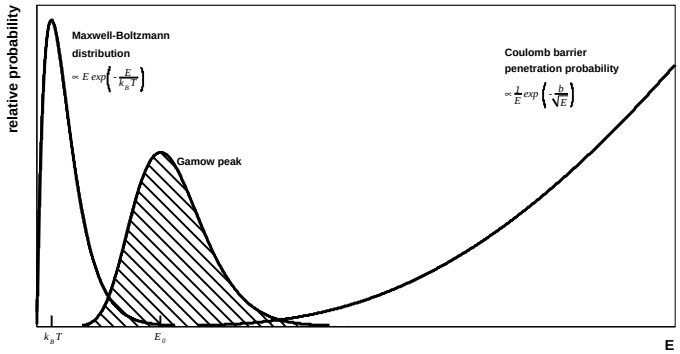

Figure A.2: Qualitative behaviour of the Gamow peak, note that the function is expanded by several order of magnitudes with respect to the other two functions.

dependence, equation A.5 implies that the nuclear reactions relevant in quiescent stellar burning are effective in a tight interval around E_0. If the reaction to be considered has no resonances in the Gamow peak region it is possible to assume

$S(E) \simeq$ constant $= S(E_0)$. Using this condition and imposing the first derivative of the integrand function of A.5 to be zero, one obtains

$$E_0 = \left(\frac{bk_BT}{2}\right)^{\frac{2}{3}} \simeq 1.22\left(Z_A^2 Z_x^2 \mu(\text{amu}) T_6^2\right)^{\frac{1}{3}} \text{ keV} \ , \tag{A.6}$$

where T_n is the temperature in units of 10^n K.

Appendix B

Data tables

Data tables of the present work. The S-factor values are calculated from the measured cross section as

$$S(E) = E \cdot \sigma(E) \cdot \exp\left(31.29 \cdot 4\sqrt{1.720/E}\right)$$

with E in keV.
The uncertainty reported in the tables are statistical only. Systematic uncertainties are 5% for recoils, 7% for γ-ray, and 5% for activation measurements. These uncertainties include the 4% contribution of target thickness and 1% of current integration, that are common to all measurements.

Table B.1: Results of recoil measurements. The end detector used for the measurement is indicated, Ionisation Chamber Telescope (ICT), Gas Silicon Telescope (GST), Time-of-Flight detection system, see section 2.4.

E_{cm} (keV)	σ (μb)	$\delta\sigma$ (μb)	S (keV b)	δS (keV b)	End detector
701	1.1	0.2	0.39	0.07	ToF–*E*
802	1.46	0.08	0.39	0.02	ToF–*E*
902	1.59	0.07	0.339	0.016	ToF–*E*
1002	1.96	0.07	0.351	0.013	ToF–*E*
1002	1.86	0.06	0.332	0.011	ToF–*E*
[1] 1102	2.16	0.02	0.334	0.004	ICT
1102	2.19	0.04	0.338	0.007	ToF–*E*
1103	2.16	0.06	0.334	0.010	ICT
1203	2.44	0.05	0.333	0.007	ToF–*E*
1203	2.44	0.09	0.333	0.013	ICT
1353	2.79	0.07	0.327	0.008	ICT
1403	3.06	0.04	0.344	0.005	GST
[1] 1403	3.03	0.08	0.340	0.009	ICT

Table B.1: Recoils (Continued)

E_{cm} (keV)	σ (μb)	$\delta\sigma$ (μb)	S (keV b)	δS (keV b)	End detector
[1] 1403	3.06	0.10	0.343	0.012	ICT
1504	3.27	0.10	0.339	0.011	ICT
1604	3.37	0.10	0.326	0.010	GST
1704	3.84	0.12	0.350	0.008	GST
1704	3.86	0.09	0.349	0.011	GST
[1]1804	4.01	0.04	0.345	0.003	ICT
1804	3.95	0.12	0.340	0.011	GST
1904	4.49	0.14	0.368	0.011	GST
1955	4.38	0.11	0.351	0.009	GST
2005	4.92	0.14	0.385	0.011	GST
2055	4.87	0.12	0.374	0.009	GST
2105	4.96	0.16	0.374	0.012	GST
[1]2156	4.95	0.05	0.366	0.003	ICT
2205	5.24	0.16	0.381	0.011	GST
2205	5.20	0.16	0.378	0.011	ICT
2305	5.32	0.14	0.374	0.010	GST
2306	5.33	0.16	0.375	0.011	GST
2406	5.54	0.14	0.378	0.009	GST
[1]2507	5.97	0.06	0.397	0.004	ICT
2762	6.70	0.07	0.420	0.005	ICT
2857	7.2	0.2	0.437	0.013	GST
2857	7.1	0.2	0.443	0.013	GST
2908	7.66	0.17	0.467	0.010	GST
2928	7.46	0.19	0.453	0.012	GST
2947	7.86	0.17	0.476	0.010	GST
2968	7.6	0.2	0.456	0.014	GST
2987	7.59	0.09	0.457	0.005	ICT
2988	7.9	0.2	0.476	0.014	GST
3008	7.63	0.17	0.458	0.010	GST
3028	7.60	0.16	0.454	0.010	GST
3048	7.6	0.2	0.452	0.013	GST
3068	7.46	0.16	0.443	0.009	GST
3089	7.73	0.19	0.458	0.012	GST
3110	7.36	0.14	0.435	0.008	GST
3130	7.3	0.3	0.431	0.016	GST

[1]Measurements where coincidence γ-rays were detected.

Table B.2: Results of the prompt γ-ray measurements. The intensity ratio $R = \sigma_{429}/\sigma_{gs}$ is also reported, see section 3.2.

E_{eff} (keV)	σ_γ (μb)	$\delta\sigma_\gamma$ (μb)	S (keV b)	δS (keV b)	R	δR
1102	2.10	0.07	0.325	0.011	0.48	0.03
1403	2.96	0.08	0.332	0.009	0.46	0.02
1403	2.86	0.05	0.321	0.005	0.47	0.01
1804	4.01	0.10	0.345	0.008	0.45	0.02
2156	5.25	0.13	0.388	0.009	0.40	0.02
2507	6.20	0.16	0.412	0.011	0.42	0.02

Table B.3: Results of the activation measurement, see section 3.3

E_{eff} (keV)	A_0 (mBq)	δA_0 (mBq)	σ (μb)	$\delta\sigma$ (μb)	S (keV b)	δS (keV b)
650	47.7	1.4	0.93	0.03	0.379	0.014
1103	172	6	2.21	0.08	0.342	0.012
2504	385	12	6.25	0.21	0.416	0.014

Deutschsprachige Zusammenfassung

Die Reaktion ^{3}He$(\alpha,\gamma)^7$Be spielt eine fundamentale Rolle in der nuklearen Astrophysik. Der Wirkungsquerschnitt dieser Reaktion stellt die grösste Unsicherheit bei der Bestimmung des solaren Neutrino Flusses dar. Auch die Synthese der leichtesten Elemente im Urknall wird von dieser Reaktion beeinflusst. Während die Häufigkeiten meisten im Urknall erzeugten Elemente in guter Übereinstimmung mit kosmologischen Modellen sind, ist die vorhergesagte Häufigkeit von ^{7}Li um einen Faktor 2 bis 3 höher als die astronomisch beobachtete Isotopenhäufigkeiten.
Bisherige Messungen dieser Reaktion basieren auf 2 verschiedenen Methoden. Zum einen kann die in der Reaktion enstehende γ-Strahlung direkt nachgewiesen werden. Zum anderen kann *offline* die Aktivität der erzeugten radioaktiven ^{7}Be Kerne gemessen werden. Die Ergebnisse dieser Messungen müssen dann mit Hilfe geeigneter Modelle zu stellaren Energiebereichen extrapoliert werden. Dazu wird der Wirkungsquerschnitt bei der Energie Null in der Form des astrophysikalischen S-Faktors $S_{34}(0)$ angegeben.

Zu Beginn dieser Arbeit wurde eine mögliche Diskrepanz der Ergebnisse der zwei experimentellen Methoden diskutiert [Ade98]. Ein Ziel der vorliegenden Arbeit war es, durch Verwendung einer unabhängigen Methode die Ursache dieser Diskrepanz zu untersuchen. Darüber hinaus sagen die verschiedenen in der Extrapolation des astrophysikalischen S-Faktors benutzten Theorien verschiedene Werte von $S_{34}(0)$ voraus. Mit den zuvor existierenden Datensätzen im Bereich von $E_{\mathrm{cm}} = 0.2 - 1.2\,\mathrm{MeV}$ kann jedoch nicht zwischen diesen Theorien unterschieden werden. Die neuen in Rahmen dieser Arbeit gewonnenen Daten im Energiebereich von $0.7 - 3.1\,\mathrm{MeV}$ können bei der Bewertung der verschiedenen theoretischen Modelle helfen.

In der vorliegenden Dissertation wurde der Wirkungsquerschnitt der Reaktion ^{3}He$(\alpha,\gamma)^7$Be mit Hilfe des Rückstoß-Massen-Separators ERNA (European Recoil separator for Nuclear Astrophysics) [Rog03b] gemessen. Dazu werden die erzeugten ^{7}Be Kerne direkt nachgewiesen. Diese Methode ist somit verschieden und unabhängig von bisherigen Experimenten. In weiteren Messungen wurde dann zusätzlich die direkte γ-Strahlung gemessen, sowie in einem weiteren Abschnitt des Experiments eine Aktivierungsmessung vorgenommen. Diese Messungen komplementieren den reinen Nachweis der ^{7}Be Kerne und halfen bei der Untersuchung der zuvor beschriebenen Diskrepanz.

Zur Messung der ^{7}Be Reaktionsprodukte mit einem Rückstoß-Massen-Separator wird

die Kernreaktion in inverser Kinematik initiiert. Dazu wird ein α-Strahl einer Intensität von mehreren μA, in ein fensterloses, doppelseitig differentiell gepumptes, rezirkulierendes ^{3}He-Gastarget [Gia04] geleitet. Aufgrund der Kinematik verlassen Projektile und Reaktionsprodukte gemeinsam die Targetzone in Vorwärtsrichtung, wobei die Trajektorien der Reaktionsprodukte aufgeweitet werden durch den Impuls der emittierten γ-Strahlung zur Strahlrichtung und das Straggling im Gas. Der Rückstoß-Massen-Separator trennt Projektile und Reaktionsprodukte und erlaubt einen anschließenden Nachweis der ^{7}Be-Kerne entweder in einem ΔE-E Ionisationsteleskop oder einer lokalen Time-of-Flight-Detektion. Letzteres mit einer Kombination aus elektrostatischem Spiegel und Micro Channel Plate Detektor als Startdetektor und Siliziumstreifen-Detektor als Stoppsignal. Dies führt zu einer sauberen Identifikation der ^{7}Be Kerne. Dabei können über den gesamten Energiebereich alle relevanten Ladungszustände der ^{7}Be Ionen gemessen werden, so dass aus der Summe der Anteile der verschiedenen Ladungszustände direkt der absolute Wirkungsquerschnitt bzw. S-Faktor berechnet werden kann.

Die im Rahmen dieser Arbeit gemessene Anregungskurve der Reaktion ^{3}He$(\alpha,\gamma)^7$Be mit dem Rückstoß-Massen-Separator wurde durch eine zusätzliche, vom Separator unabhängige Messung gestützt. Dazu wurde der Strahl am Ende des ^{3}He-Gastargets in einer Kupfeplatte gestoppt. Das Gasprofil des Targets wurde dabei nicht gestört bzw. verzerrt. Die in der Gaszelle erzeugten ^{7}Be Kerne wurden so in das Kupfer implantiert und nach dem Ausbau in das Low-Level Laboratorium des Gran Sasso Labors (Italien) geschickt. Die Ergebnisse der dort durchgeführten Aktivierungsmessung sind in hervorragender Übereinstimmung mit der Messung der ^{7}Be Ejektile am Rückstoß-Massen-Separator.

Im letzten Abschnitt der vorliegenden Arbeit werden die Übereinstimmungen der zur Extrapolation verwendeten Theorien mit den experimentellen Wirkungsquerschnitts-Daten untersucht. Von den in der Literatur verwendeten Direct Capture [Des04] bzw. Mikroskopischen Modellen [Kaj84, Nol01] zeigen nur letztere eine gute Übereinstimmung mit den neuen Daten. Hier ist insbesondere die Energieabhängigkeit bei höheren Energien hervorzuheben, die zur Selektion eines der Modelle führen kann. Zur Extrapolation werden die Modelle jedoch nicht nur an die neuen Daten, sondern auch an alte Datensätze gefittet. Hier ist zu beachten, das ein Teil der in der Literatur verfügbaren Datensätze Fehlerangaben enthält, die nicht nur die statistischen, sondern auch die systematischen Unsicherheiten mit einschliessen. Da in diesen Fällen nur die gesamte Unsicherheit angegeben ist, können sie nicht als Basis eines Fits dienen.

Die so getroffene Auswahl der theoretischen Modelle und Datensätze führt zu einem Wert von $S_{34}(0) = 0.569 \pm 0.023\,\mathrm{keV\,b}$. Dabei berücksichtigt die Unsicherheit lediglich statistische Fehler in den experimentellen Daten, der mögliche Einfluss der Skalierung von existierenden theoretischen Modellen konnte im Rahmen dieser Arbeit jedoch nicht untersucht werden. Bestätigt sich dieses hohe Ergebniss des astrophysikalischen S-Faktors $S_{34}(0)$, so würde die bisherige sehr gute Übereinstimmung des solaren Standardmodelle mit den Neutrinomessungen an SNO und SuperKamiokande nicht mehr aufrecht erhalten werden können. Dieser beobachtete Fluss der solaren Neutrinos skaliert nahezu linear mit dem Wirkungsquerschnitt der Reaktion ^{3}He$(\alpha,\gamma)^7$Be im solaren Gamow-Peak.

Auch das angesprochene Problem der Überproduktion von ^{7}Li im Urknall würde durch einen höheren Wirkungsquerschnitt sogar noch grösser werden. Eine Kernphysikaliche Lösung des ^{7}Li Probleme ist somit nahezu ausgeschlossen.

Bibliography

[Abe08] S. Abe, *et al.* Phys. Rev. Lett. **100**(2008) 221803

[Ade98] E. Adelberger, *et al.* Rev. Mod. Phys. **70**(1998) 1265

[Ago03] S. Agostinelli, *et al.* Nucl. Instrum. Methods A **506**(2003) 250

[Ahm02] Q. R. Ahmad, *et al.* Phys. Rev. Lett. **89**(2002) 011301

[Ale84] T. Alexander, *et al.* Nucl. Phys. **A427**(1984) 526

[Ang99] C. Angulo, *et al.* Nucl. Phys. A **656**(1999) 3

[Ang05] C. Angulo, *et al.* Astroph. J, Lett. **630**(2005) L105

[Ans92] P. Anselmann, *et al.* Phys. Lett. B. **B285**(1992) 376

[Arp08] C. Arpesella, *et al.* Phys. Rev. Lett. **101**(2008) 091302

[Bah82] J. N. Bahcall, R. Davis, Jr. in C. A. Barnes (Hrsg.), Essays in Nuclear Astrophysics 1982 243–+ see also URL `http://www.sns.ias.edu/jnb/Papers/Popular/snhistory.html`

[Bah00] J. N. Bahcall, R. J. Davis *Publications of the ASP* **112**(2000) 429

[Bah04] J. N. Bahcall, M. H. Pinsonneault Phys. Rev. Lett. **92**(2004) 121301

[Bah05] J. N. Bahcall, *et al.* Astroph. J, Lett. **621**(2005) L85

[Bec95] H. W. Becker, *et al.* Z. Phys. A **351**(1995) 453

[Bem06] D. Bemmerer, *et al.* Phys. Rev. Lett. **97**(2006) 122502

[Bem07] D. Bemmerer Private communication 2007

[Ber90] M. Berz Nucl. Instrum. Methods A **298**(1990) 473

[Bie03] J. Biersack, J. Ziegler Transport of ions in matter: TRIM program version 2003.26 IBM Research, New York and Hahn Meitner Institute, Berlin 2003

[Bla52] J. M. Blatt, V. F. Weisskopf Theoretical Nuclear Physics John Wiley & Sons 1952

[Bon99] R. Bonetti, *et al.* Phys. Rev. Lett. **82**(1999) 5205

[Bro07] T. A. D. Brown, *et al.* Phys. Rev. C **76**(2007) 055801

[Bus80] F. Busch, *et al.* Nucl. Instrum. Methods **171**(1980) 71

[Chr61] R. F. Christy, I. Duck Nucl. Phys. (1961) 89

[Coc04] A. Coc, *et al.* Astroph. J. **600**(2004) 544

[Col02] P. Coles, F. Lucchin Cosmology: The Origin and Evolution of Cosmic Structure, Second Edition Wiley-VCH 2002

[Con07] F. Confortola, *et al.* Phys. Rev. C **75**(2007) 065803

[Cor05] L. Coraggio, N. Itaco Phys. Lett. B. **616**(2005) 43

[Cor08] L. Coraggio, N. Itaco Private communication 2008

[Cos08] H. Costantini, *et al.* Nucl. Phys. A **814**(2008) 144

[Csó00] A. Csótó, K. Langanke *Few-Body Systems* **29**(2000) 121

[Cuo04] A. Cuoco, *et al.* Int. J. Mod. Phys. **19**(2004) 4431

[Cyb04] R. Cyburt Phys. Rev. D **70**(2004)

[Cyb08] R. H. Cyburt, B. Davids Phys. Rev. C **78**(2008) 064614

[D'A94] G. D'Agostini *Nuclear Instruments and Methods in Physics Research A* **346**(1994) 306

[DC06] M. De Cesare Un rivelatore TOF-E per lo studio della ^{3}He(^{4}He, γ)^{7}Be alle ernergie d'interesse astrofisico utilizzando il separatore di massa ERNA Thesis Università degli Studi di Napoli Federico II 2006

[Des04] P. Descouvemont, *et al.* At. Data Nucl. Data Tables **88**(2004) 203

[DL03] A. Di Leva Studio della reazione nucleare ^{12}C(α, γ)^{16}O alle energie di interesse astrofisico Thesis Università degli Studi di Napoli Federico II 2003

[ENS] Evaluated and Compiled Nuclear Structure Data
URL `http://www.nndc.bnl.gov/ensdf/`

[Fie06] B. D. Fields, K. A. Olive Nucl. Phys. A **777**(2006) 208

[Fra83] G. W. Frazer Nucl. Instrum. Methods **206**(1983) 445

[Fri86] H. Frischkorn, K. Groeneveld *Physica Scripta* **T6**(1986) 89

[Gia04] L. Gialanella, *et al.* Nucl. Instrum. Methods A **522**(2004) 432

[Gör80] J. Görres, *et al.* Nucl. Instrum. Methods **177**(1980) 295

[Gyü07] G. Gyürky, *et al.* Phys. Rev. C **75**(2007) 035805

[Hah66] R. L. Hahn, E. Ricci Phys. Rev. **146**(1966) 650

[Hax08] W. C. Haxton, A. M. Serenelli Astroph. J. **687**(2008) 678

[Hil88] M. Hilgemeier, *et al.* Z. Phys. **A329**(1988) 243

[Hin09] G. Hinshaw, *et al.* Astroph. J, Suppl. Ser. **180**(2009) 225

[Hof08] H. Hofmann Private communication 2008

[Hol59] H. D. Holmgren, R. L. Johnston Phys. Rev. **113**(1959) 1556

[Ioc07] F. Iocco, *et al.* Phys. Rev. D **75**(2007) 087304

[Ioc08] F. Iocco, *et al. ArXiv e-prints* (2008)

[Jam75] F. James, M. Roos *Comput. Phys. Commun.* **10**(1975) 343

[Kaj84] T. Kajino, A. Arima Phys. Rev. Lett. **52**(1984) 739

[Kaj87] T. Kajino, *et al.* Astroph. J. **319**(1987) 531

[Kne04] J. P. Kneller, G. Steigman *New Journal of Physics* **6**(2004) 117

[Kor06] A. J. Korn, *et al.* Nature **442**(2006) 657

[Krä82] H. Kräwinkel, *et al.* Z. Phys. A **304**(1982) 307

[Lan86] K. Langanke Nucl. Phys. A **457**(1986) 351

[Liu81] Q. Liu, *et al.* Phys. Rev. C **23**(1981) 645

[Mal93] R. A. Malaney, G. J. Mathews Phys. Rep. **229**(1993) 145

[Man08] G. Mangano Private communication 2008

[Mar68] J. Marion, F. Young Nuclear Reaction Analysis. Graphs And Tables. North-Holland, Amsterdam 1968

[Mer86] T. Mertelmeier, H. M. Hofmann Nucl. Phys. A **459**(1986) 387

[MK99] P. Maier-Komor, *et al.* Nucl. Instrum. Methods A **438**(1999) 73

[Moh93] P. Mohr, *et al.* Phys. Rev. C **48**(1993) 1420

[Nag69] K. Nagatani, *et al.* Nucl. Phys. A **128**(1969) 325

[Nar04] B. NaraSingh, *et al.* Phys. Rev. Lett. **93**(2004) 262503

[Nol01] K. M. Nollett Phys. Rev. C **63**(2001) 054002

[Oli00] K. A. Olive, *et al.* Phys. Rep. **333**(2000) 389

[Osb84] J. Osborne, *et al.* Nucl. Phys. **A419**(1984) 115

[Par63] P. Parker, R. Kavanagh Phys. Rev. **131**(1963) 2578

[PC06] Private Communication 2006

[Pis08] O. Pisanti, *et al. Computer Physics Communications* **178**(2008) 956

[Rob83] R. Robertson, *et al.* Phys. Rev. **C27**(1983) 11

[Rog99a] D. Rogalla, *et al.* Nucl. Instrum. Methods A **437**(1999) 266

[Rog99b] D. Rogalla, *et al.* Eur. Phys. J. A **6**(1999) 471

[Rog03a] D. Rogalla Aufbau eines Recoil-Massenseparators für die nukleare Astrophysik Dissertation Ruhr Universität Bochum 2003
URL `http://www-brs.ub.rub.de/netahtml/HSS/Diss/RogallaDetlef/diss.pdf`

[Rog03b] D. Rogalla, *et al.* Nucl. Instrum. Methods A **513**(2003) 573

[Rol88] C. Rolfs, W. Rodney Cauldrons in the Cosmos The University of Chicago Press 1988

[Sch04] D. Schürmann, *et al.* Nucl. Instrum. Methods A **531**(2004) 428

[Sch05] D. Schürmann, *et al.* Eur. Phys. J. A **26**(2005) 301

[Sch07] D. Schürmann Messung des totalen Wirkungsquerschnitts der Reaktion $^{12}C(\alpha,\gamma)^{16}O$ mit dem Rückstoß-Massenseparator ERNA Dissertation Ruhr Universität Bochum 2007
URL `http://www-brs.ub.rub.de/netahtml/HSS/Diss/SchuermannDaniel/diss.pdf`

[Ser04] P. D. Serpico, *et al. Journal of Cosmology and Astro-Particle Physics* **12**(2004) 10

[Til02] D. R. Tilley, *et al.* Nucl. Phys. A **708**(2002) 3
URL `http://www.tunl.duke.edu/NuclData/`

[Tom63] T. Tombrello, P. Parker Phys. Rev. **131**(1963) 2582

[Vol83] H. Volk, *et al.* Z. Phys. **A310**(1983) 91

Acknowledgments

Ich bedanke mich bei Herrn Prof. Claus Rolfs dafür, die Möglichkeit der Fertigstellung dieser Arbeit mir geboten zu haben, und insbesondere weil er ein Beispiel für mich dargestellt hat.
Ringrazio il Dott. Lucio Gialanella senza il cui contributo questo lavoro forse non sarebbe stato mai completato. Grazie per la costante presenza e la sollecitudine con la quale mi ha seguito durante tutto il lavoro di tesi.
Ich möchte mich bei allen EP3 Mitarbeitern bedanken, Dr. Detlef Rogalla, Dr. Ralf Kuntz, Dr. Frank Schümann, ohne die den Erfolg dieser Arbeit nicht möglich gewesen wäre. Insbesondere möchte ich mich bei Herr Dr. Frank Strieder bedanken für das *I agree* mit meinen Ideen, das mir ermöglichen hat, zu fehler und zu lernen. Ich danke auch Dr. Daniel Schürmann für seinen wertvollen Beitrag über diese Arbeit und für seinen Reiz zur meinen Verbesserung.
Ringrazio sentitamente tutti i collaboratori di Napoli e Caserta che si sono avvicendati nei turni di misura a Bochum: il Prof. Nicola De Cesare, il Prof. Antonio D'Onofrio, il Dott. Gianluca Imbriani, il Dott. Vincenzo Roca. Grazie a Mario De Cesare per il lavoro svolto e per avermi aiutato a capire molte cose. Un ringraziamento particolare va al Prof. Mario Romano per le illuminanti chiacchierate negli interminabili turni di notte. Al Prof. Filippo Terrasi sono anche grato per le innumerevoli chiarificazioni sugli aspetti più sottili dell'analisi statistica dei dati.
Szeretném megköszönni Dr. Somorjai Endrének a kísérletben való közreműködését valamint folyamatos lelkesítését. Továbbá köszönet jár Dr. Fülöp Zsoltnak és Dr. Gyürky Gyorgynek az aktivitásmérés és a ^{56}Co forrás előkészítésében való részvételéért.
Thanks to Dr. Daniel Bemmerer for his work on the activity measurements at the Low Level Laboratory of the Laboratori Nazionali del Gran Sasso. For such measurements I need to thank the LUNA Collaboration that allowed the use of their experimental setup.
Thanks to Dr. Peter Mohr for the discussions on the theoretical models.
Ringrazio la Dott.ssa Alba Formicola, oltre che per il lavoro svolto nelle misure di attività, per le discussioni e i consigli, di fisica e non, che mi sono sempre stati di grande aiuto nel lavoro e nella vita.
Ich bedanke mich bei Frau Iris Bergholz und Herr Jürgen Wöhlert für ihre Hilfe bei der Bürokratie. Ebenfalls bedanke ich mich bei Dr. Hans Werner Becker für die freundliche

Leihgabe an benötigten Teilen, und bei allen Mitarbeiter des DTLs für ihre Arbeit.

Debbo esprimere la mia immensa riconoscenza al Dr. Francesco Raiola per essere stato, ed essere ancora, un ottimo amico e un valente collega.
Last but not least, ho un debito inestinguibile con le persone che ho avuto l'opportunità di conoscere negli anni che ho trascorso a Bochum. Grazie (ma non sarà mai abbastanza) ad Alice. Grazie a Gianpiero e Vincenza. Grazie agli innumerevoli altri che, purtroppo, non so elencare.

Lebenslauf

Antonino Di Leva

Geburtsdatum	07/12/1973
Geburtsort	Caserta, Italien
Staatsangehörigkeit	Italienisch
Wohnort	Neapel, Italien

1979 - 1987	Grundschule in Positano, Italien
1987 - 1992	Staatliche höhere Schule für Handel-und Verwaltungswesen P. Comite in Amalfi, Italien
1992	Abitur
1993 - 2003	Studium Physik, Neapel Universität Federico II, Italien
2003 - 2007	Wissenschaftlicher Mitarbeiter im Institut für Physik mit Ionenstrahlen, Ruhr-Universität Bochum
2007 - 2008	Wissenschaftlicher Mitarbeiter im INFN, Italien
Seit August 2008	Fellowship im Bereich der Umweltwissenschaften, Dipartimento di Scienze Ambientali, Seconda Università degli Studi di Napoli, Caserta, Italien